SILICON BASED DIELECTRICS: GROWTH, CHARACTERIZATION, AND APPLICATIONS IN INTEGRATED OPTICS

A DISSERTATION SUBMITTED TO

THE DEPARTMENT OF PHYSICS

AND THE INSTITUTE OF ENGINEERING AND SCIENCE

OF BILKENT UNIVERSITY

IN PARTIAL FULFILLMENT OF THE REQUIREMENTS

FOR THE DEGREE OF

DOCTOR OF PHILOSOPHY

By

Feridun Ay

August, 2005

I certify that I have read this thesis and that in my opinion it is fully adequate, in scope and in quality, as a dissertation for the degree of doctor of philosophy.

Prof. Dr. Atilla Aydınlı (Supervisor)

I certify that I have read this thesis and that in my opinion it is fully adequate, in scope and in quality, as a dissertation for the degree of doctor of philosophy.

Prof. Dr. Raşit Turan

I certify that I have read this thesis and that in my opinion it is fully adequate, in scope and in quality, as a dissertation for the degree of doctor of philosophy.

Assoc. Prof. Dr. Recai Ellialtıoğlu

I certify that I have read this thesis and that in my opinion it is fully adequate, in scope and in quality, as a dissertation for the degree of doctor of philosophy.

Assist. Prof. Dr. Hilmi Volkan Demir

I certify that I have read this thesis and that in my opinion it is fully adequate, in scope and in quality, as a dissertation for the degree of doctor of philosophy.

Assist. Prof. Dr. Dönüş Tuncel

Approved for the Institute of Engineering and Science:

Prof. Dr. Mehmet B. Baray
Director of the Institute

ABSTRACT

SILICON BASED DIELECTRICS: GROWTH, CHARACTERIZATION, AND APPLICATIONS IN INTEGRATED OPTICS

Feridun Ay
PhD in Physics
Supervisor: Prof. Dr. Atilla Aydınlı
August, 2005

In recent years, growing attention has been paid to silicon based dielectrics, such as silicon oxynitrides, silicon nitrides, and semiconductor doped silicon oxides, all combined under the name silica on silicon technology. This attention has been motivated mainly due to their excellent optical properties such as well controlled refractive index and high transparency over a wide range of wavelength.

In accordance with the main goal of this study that relied on the utilization of silicon based dielectrics and their optimization for applications in integrated optics, an emphasis was given to optimize the compositional and optical properties of these materials. A detailed quantitative compositional analysis using Fourier transform infrared spectroscopy resulted in identification of the germanosilicate dielectrics as the most promising candidates for use in integrated optics. The first reported systematic study of propagation losses for different-index planar waveguides by using prism coupling method was correlated with the compositional analysis. This study had an important outcome for planar waveguides fabricated with germanosilicate core layers resulting in the lowest propagation loss values reported so far for as deposited CVD-grown films at λ=1.55 μm, eliminating the need for costly and cumbersome annealing process.

An improvement of the prism coupling technique led to a new approach for elasto-optic characterization of thin polymer films. This completely new method allows one to determine the optical anisotropy and out-of-plane mechanical properties and to correlate both in order to obtain the elasto-optical properties of thin polymer films, for the first time.

Of interest as potential electro-optic material, we have concentrated on thermally poled germanosilicate films deposited on fused-silica substrates by PECVD.

As a result of an optimization study, we demonstrated a record peak nonlinear coefficient of ∼1.6 pm/V, approximately twice as strong as the highest reliable value reported in a thermally poled fused silica glass.

Finally, we have demonstrated several applications of this technology in the field of integrated optics. Since optical waveguides constitute the building blocks of many integrated optical devices, we had first concentrated on design and optimization of waveguides employing germanosilicates as the core layers. The final step of our work concentrated on design and implementation of microring resonator devices based on germanosilicate layers.

Keywords: Integrated optics, Silicon dielectrics, Silicon oxide, Silicon oxynitride, Germanium, Germanosilicate, PECVD, FTIR, Waveguide, Optical absorption, Prism coupling, Elastic modulus, Elasto-optic coefficient, Birefringence, Nonlinearity, Electro-optic coefficient, Thermal poling, Ring resonator.

ÖZET

SİLİSYUM TABANLI DİELEKTRİKLER: TÜMLEŞİK OPTİKTE KULLANIMA YÖNELİK BÜYÜTME VE İNCELEME

Feridun Ay
Fizik, Doktora
Tez Yöneticisi: Prof. Dr. Atilla Aydınlı
Ağustos, 2005

Silisyum tabanlı dielektriklerin üstün optik özellikleri ve kırılma indislerinin geniş aralıkta ayarlanabilirliği bu malzemelerin tümleşik optikte kullanılmasına yönelik çalışmalarda büyük ilgi çekmesine neden olmaktadır.

Bu çalışmada silisyum tabanlı dielektriklerin tumleşik optik aygıtlarda kullanımları amaçlanarak optik özellikleri ve kompozisyonları incelenip optimize edildi. Fourier dönüşümlü spektroskopi kullanılarak yapılan ayrıntılı kompozisyon analazi sonucunda germanosilikat dielektrikleri tümleşik optik uygulamaları için en uygun malzemeler olarak tespit edildi. Prizma çiftlemesi yöntemi ile germanosilikat düzlemsel dalga kılavuzlarında ilk defa farklı kırılma indisli malzemeler için karşılaştırmalı optik kayıp ölçümleri yapıldı. Bu çalışma neticesinde literatürde ısıl olarak tavlanmamış $\lambda = 1.55$ μm dalga boyunda en düşük kayıplı duzlemsel dalga kılavuzları elde edildi.

Prizma çiftlemesi tekniğinin geliştirilmesi ile polimerler gibi yumuşak malzemelerin elesto-optik özelliklerinin ölçülebilmesi sağlanmıştır. Bu yeni yöntem ile eşzamanlı olarak yapılan farklı yönlü optik indis ölçümleri ve dikey yönlü mekanik sabit ölçümleri kullanılarak, ince polimer tabakaların elasto-optik katsayıları bulunabilmiştir.

Germanosilikat dielektriklerinin electro-optik özelliklerini arttırmak hedefi ile PECVD yöntemi ile yapılan büyütme koşulları ile ısıl kutuplama şartları optimize edildi. Bunun sonucunda şu ana kadar silika cam tabanlı malzemelerde edilmiş doğrusal olmayan en büyük katsayının iki katı elde edildi.

Son olarak, germanosilikatlara dayalı tümleşik optik aygıtlar üretildi. Bunlar

arasında ilk olarak tek kipli dalga kılavuzları üretilip incelendi. Çalışmanın sonunda germanosilikatlara dayalı halka çınnaç aygıtları tasarlandı, optimizasyon çalışmasını müteakip özellikleri ölçüldü.

Anahtar sözcükler: Tümleşik optik, Silisyum dielektrikler, Silisyum oksit, Silisyum oksinitrat, Germanium, Germanosilikat, PECVD, FTIR, Dalga Kılavuzu, Optik soğurma, Prizma çiftlemesi, Elastik katsayı, Elasto-optik katsayı, Doğrusal olmayan katsayı, Electro-optik katsayı, Isıl tavlama, Halka çınlaç.

Acknowledgement

It is my pleasure to express my deepest gratitude to Prof. Dr. Atilla Aydınlı for his guidance, moral support, friendship and assistance during this research. I am indebted for his efforts and enthusiasm.

I would like to thank the members of my thesis committee: Prof. Dr. Raşit Turan, Assoc. Prof. Dr. Recai Ellialtıoğlu, Assist. Prof. Dr. Hilmi Volkan Demir, and Assist. Prof. Dr. Dönüş Tuncel, for reading the manuscript and commenting on the thesis.

I would like to thank our current and former group members Dr. Aykutlu Dâna, Aşkın Kocabaş (miralay), Coşkun Kocabaş, İsa Kiyat, Orçun Ergün and Selcen Aytekin for creating a fruitful, enjoyable, and unique working environment.

I would like to acknowledge Aydoğan Özcan, M.J.F. Digonnet, and G.S. Kino of Edward L. Ginzton Laboratory, Stanford University, for the close and fruitful collaboration on poled germanosilicates project. Especially the enthusiasm of Aydoğan has been a source of motivation for me.

I would like to thank Assoc. Prof. Sedat Ağan for providing the TEM results along with being so highly motivated and hard working. Our close work with him has been a stimulating experience. I also would like to acknowledge Dr. Temel H. Büyüklimanlı for providing us with SIMS results. I appreciate the help of the physicist Murat Güre and the technician Ergün Karaman.

M. Ali Can, Özgür Çakır, Kerim Savran, Süleyman U. Eker, Sefa Dağ, and many other friends helped to keep my spirits high all the time which I appreciate very much.

I am indebted to my family for their continuous support, care, and encouragement.

And finally, I thank my dearest Suzan, as she means so much for me. I would like to devote this work to her and my family.

Contents

1 Introduction **1**

1.1 Milestones in the Field of Photonics 1

1.2 Why Silicon Based Dielectrics? 2

1.3 Contribution of This Work and Organization of the Dissertation . 5

2 Silicon Based Dielectrics – General Overview **8**

2.1 Plasma Enhanced Chemical Vapor Deposition 8

2.2 Silicon Oxide and Oxynitride Layers 10

2.3 Germanium Doped Layers 13

3 Germanosilicate Dielectrics I: Compositional Analysis Using FTIR **18**

3.1 General Remarks on FTIR Spectroscopy 19

3.2 Experimental Setup 21

3.3 IR Analysis of Germanosilicate Layers 23

4 Germanosilicate Dielectrics II: Index of Refraction and Propagation Loss Measurements Using PCM 29

4.1 Basic Principles of the Prism Coupling Method 30

4.2 Propagation Loss Measurements and PCM 34

4.3 Experimental Setup 37

4.4 Propagation Loss and Refractive Index Analysis of Germanosilicate Layers 39

4.5 Effects of Thermal Annealing on Germanosilicate Layers 44

4.6 Improvement of the Prism Coupling Method 48

4.6.1 Stress Effects in Prism Coupling Measurements of Thin Polymer Films 48

4.6.2 Measurement Results and Discussion 50

4.7 A New Approach: Elasto–Optical Properties of Small Young–Moduli Films By Prism Coupling Method 56

4.7.1 Current State of the Problem - Literature Review 56

4.7.2 Index of Refraction and Birefringence 58

4.7.3 Out–of–Plane Mechanical Properties by Prism Coupling Method 62

4.7.4 Elasto–Optical Properties 66

5 Germanosilicate Dielectrics III: Nonlinear Properties 72

5.1 Nonlinear Optics in Brief 72

5.1.1 Second Order Nonlinearities 73

5.1.2 Third Order Nonlinearity: Kerr Effect 78

5.2 Nonlinearity in Thermally Poled Germanosilicate Thin Films . . . 79

5.2.1 Second Order Nonlinearity in Poled Glasses 80

5.2.2 Germanosilicate Growth Process 82

5.2.3 Thermal Poling and Characterization of the Poled Germanosilicate Films 83

6 Application of Germanosilicate Layers to Ring Resonator Devices 94

6.1 Single Mode Germanosilicate Waveguides 95

6.1.1 Waveguide Structure 95

6.1.2 Fabrication Process 98

6.1.3 Propagation Loss Measurement and Optimization of the Germanosilicate Waveguides 106

6.2 Germanosilicate Ring Resonator Devices 111

6.2.1 Ring Resonator Devices Basics 112

6.2.2 Bending Loss and Coupling Coefficient Calculations 115

6.2.3 Lithographic Mask Design Issues 121

6.2.4 Fabrication of Germanosilicate Microring Resonator Devices 123

6.2.5 Measurement Results for Germanosilicate Ring Resonators 125

7 Conclusions 136

A List of Publications 151

List of Figures

1.1 Attenuation characteristics of a typical silica fiber guide. (Adapted from [12]). 4

2.1 PECVD reactor structure. 9

2.2 Variation of index of refraction of SiO_x and $SiON$ films with N_2O and NH_3 precursor gases flow rates and growth temperature. . . . 12

2.3 Comparison of the O−H and N−H stretching bands as obtained with FTIR absorbance spectroscopy for germanosilicate and germanate films as a function of GeH_4 flow rate at fixed SiH_4 and N_2O flows. 15

2.4 Variation of index of refraction for germanosilicate layers with GeH_4 flow rate. 16

3.1 Illustration of (a) bending, (b) symmetric stretching, and (c) antisymmetric stretching vibrations for a polyatomic molecule. . . . 19

3.2 The FTIR experimental setup used for infrared absorbance measurements. 22

3.3 Infrared absorption spectra of germanosilicate samples at 250–1550 cm^{-1} range with the the following GeH_4 flow rates; s0: 0, s1: 5, s2: 10, s3: 20, s4: 30, s5: 50, s6: 60 and s7: 70 *sccm*. 24

3.4 Variation of normalized absorption band area for Si−O and Ge−O related bonds with increasing GeH_4 flow rate. 25

3.5 FTIR absorption coefficient, α vs incident wavenumber for the germanosilicate samples in the N−H and O−H absorption band region. 26

3.6 Variation of calculated N−H (a) and O−H (b) bond concentrations for germanosilicate samples with increasing GeH_4 flow rate. . . . 28

4.1 Schematic representation of a prism coupler. 31

4.2 Schematic representation of the commonly used propagation loss measurement techniques based on prism coupling. 34

4.3 Experimental setup for measuring the coupling angles. The laser beam is incident on the coupling prism. The prism coupler setup is mounted onto a high precision rotary stage with stepper motor having a precision of better than ± 0.01°. 37

4.4 Variation of the index of refraction for germanosilicate layers with GeH_4 flow rate at λ = 632.8 and 1550 nm for both TE and TM polarizations. 40

4.5 Photographs of the experimental configuration for prism coupling technique used for index of refraction and propagation loss measurements at (a) λ= 632.8 nm and (b) 1.55 μm. 41

4.6 A schematic picture of the mode profile of (a) the slab waveguides used for propagation loss measurements using prism coupling method along with (b) a simulated mode profile. 42

4.7 SIMS profiles for the (a) as deposited GeH_4= 90 sccm , (b) GeH_4= 90 sccm and annealed at 1000 ℃, and (c) GeH_4= 120 sccm and annealed at 1000 ℃ samples. 45

4.8 (a) Scanning electron and (b) transmission electron microscopy images of the *Ge* precipitate formed at the silicon/dielectric interface for the sample *sims3*. 46

4.9 Coupled light spectrum for both (a) triangle and (b) trapezoid shaped prisms for PS films. 50

4.10 Light coupling efficiency vs. loaded force for both TE and TM polarizations as observed for PS films. 52

4.11 Typical spectrum of guided modes with TM (or TE) polarized light for PMMA. 53

4.12 Calculated refractive index values vs. thickness change of PMMA films. A small but steady increase of the refractive index is clearly observed for both polarizations. 54

4.13 Birefringence vs. thickness change of PMMA polymer films. . . . 55

4.14 Change of the TE and TM refractive index for PS films with change in the film thickness. 59

4.15 Change of the TE and TM refractive index for BCB films with change in the film thickness. 60

4.16 Change of birefringence for PS films with change in the film thickness. 61

4.17 Detailed representation of the system used for pressure application and readout in the modified prism coupler setup. 62

4.18 Experimental data for variation of $\Delta y/y_0$ with the applied force F for PMMA films with thicknesses of 3.10, 3.22, 4.30, 4.75, and 6.10 μm. Note that the coupling is completed for $F > 15$ N. . . . 64

4.19 Variation of the out–of–plane elastic modulus with films thickness for PMMA films. 65

5.1 Thermal poling apparatus consisting of a hot plate and a pyrex beaker oven. The contact between the substrate and electrodes is maintained by a ceramic clamp. 83

5.2 Calibrated MF curves measured for (a) sample #2, (b) sample #3, and (c) sample #4. 85

5.3 The recovered optical nonlinearity depth profiles of sample #2 (blue), #3 (red) and #4 (black). 86

5.4 Left axis (blue curve): the ratio of the $\chi^{(3)}$ of the PECVD grown germanosilicate layer to the $\chi^{(3)}$ of fused silica; right axis (green curve): maximum built-in E-field measured in poled germanosilicate films. 87

5.5 Charge density of poled sample #4, inferred by differentiating the recovered $d_{33}(z)$ profile. 89

5.6 The recovered nonlinearity profiles of sample #1 (blue), #3 (red), #6 (black) and #7 (green). 90

5.7 The recovered optical nonlinearity depth profile of samples #3 (red) and #5 (blue). 92

6.1 Fundamental mode profiles for (a) TE and (b) TM polarization of germanosilicate ridge waveguide as calculated by BPM. 96

6.2 Index of refraction for the germanosilicate sample grown with GeH_4 flow rate of 50 sccm as a function of wavelength as measured by ellipsometry. 97

6.3 Schematic representation of the growth process of the layered structure for germanosilicate optical waveguides. 99

6.4 Schematic representation of the process of waveguide strip definition on the layered structure for germanosilicate optical waveguides. 101

6.5 Formation of irregularities at the edges of the metal stripes after the liftoff process, as viewed with optical microscope. These wriggles are potential scattering sources increasing the propagation losses in optical waveguides. 102

6.6 SEM images of the formed edge defects of Cr stripes in the overdeveloped samples after liftoff process. The over developed PR structure (a) and the formed edge defects (b) are clearly identified. . . 103

6.7 Index of refraction for the PECVD as-grown SiO_x film as a function of wavelength. 104

6.8 The final structure of the waveguide as viewed through an optical microscope. The Si, SiO_2, SiO_x, and ITO layers are clearly identified, while it is difficult to distinguish the SiO_x:Ge layer sue to the similar material nature. 105

6.9 Optical waveguide devices measurement setup. 107

6.10 Insertion loss results for the TE and TM input polarized light for identical waveguides of different length. The waveguide geometry is depicted in the inset. 108

6.11 Insertion loss results for the TE and TM input polarized light for identical waveguides of different length and lower and upper cladding thicknesses increased to ∼4 μm. The waveguide geometry is depicted in the inset of the figure. 109

6.12 A schematic picture of a single bus microring resonator channel dropping filter. 111

6.13 Calculated transmission characteristics of a sample single bus microring resonator. 113

6.14 Schematic representation of the effective index model used to reduce the 3D structure to 2D. 116

6.15 Waveguide layout model used for BPM simulation of bending losses in curved structures. 117

6.16 Bending loss results as extrapolated to 90° as a function of arc radius as calculated both analytically and by 3D-BPM. 118

6.17 (a) Waveguide layout model used for 3D-BPM calculation of coupling coefficients, κ. (b) A sample simulation output for a device with a gap of 1 μm and R=1000 μm. 119

6.18 Coupling factors as calculated by 3D-BPM simulations as a function of gap length for various radii. 120

6.19 A two-step and two-chip photolithographic mask layout as designed with MEMS L-Edit and used for fabrication of germanosilicate ring resonator devices. 122

6.20 An optical microscope image of a 750 μm radius ring resonator. The inset shows in detail the coupling region and the 0.8 μm gap between the bus and ring waveguides, the widths of the waveguides are 3.0 μm. 124

6.21 A schematic picture of the ring resonator device with the top ITO electrode structure. The insets show the optical micrographs of the top ITO electrode layers placed onto the waveguide ridge structures.125

6.22 Transmission spectra results for some of the ring resonator devices with different radii as a function of wavelength at TE polarization. 126

6.23 Transmission spectra results and analytical function fit to a single bus microring resonator with R=1000 μm and gap=1.3 μm at TE polarization. 128

6.24 Optical microscope image of the coupling region between the bus waveguide and the ring structure in a resonator device with R=1000 μm and gap=1.3 μm. The left inset of the figure shows the magnified portion of the coupling region. The discontinuity region (trench) formed during the PECVD growth of the upper silicon oxide cladding layer is highlighted in the insets and is marked with ①. 131

6.25 Transmission spectra result for a microring resonator with R=1000 μm and gap=1.3 μm at both TE and TM polarizations fabricated without the upper and lower ITO layers. 132

6.26 The measured (a) Q-factors, (b) Finesse values, and (c) the calculated propagation loss values determined from the function fitting for the ring resonator devices fabricated with and without ITO layers. The lines are drawn to guide the eye. 133

List of Tables

2.1 Growth parameters for silicon oxide, nitride, and oxynitride layers. 11

2.2 Refractive index values for some of the silicon based dielectrics. . 14

3.1 Growth parameters for germanosilicate films used in FTIR measurements. 23

3.2 N−H bond str. concentration calculation details for germanosilicate films by using FTIR transmittance spectroscopy. 28

4.1 Summary of the measurements of index of refraction for germanosilicate layers for TE & TM polarization at $\lambda = 633$ and 1550 nm, with varying GeH_4 flow rate. 40

4.2 Propagation loss variation with GeH_4 flow rate for three representative germanosilicate planar waveguides at $\lambda = 1.55$ μm. 43

4.3 List of the germanosilicate samples investigated by secondary ion mass spectroscopy. 44

4.4 Summary of all refractive index and thickness measurements for polymer films in this study. 55

4.5 Results of FEM analysis and elasto-optic coefficient calculations. The tabulated data includes the initial thickness of the guiding polymer films (y_0), maximum film thickness change with the applied pressure (Δy_{max}), calculated elastic moduli of the layers (E), constants (K_1, K_2, and K_3) as determined by FEM simulations, the slope values (m_x and m_y), and the calculated elasto-optic constants C_1, C_2 and C. 69

5.1 Characteristics and poling time of germanosilicate films poled in air at ~5 kV and ~280 ℃. 82

6.1 Optimized process parameters used in reactive ion etching of germanosilicate layers. 104

6.2 Summary of the propagation loss values for germanosilicate waveguides with different thicknesses of the cladding layers. 110

6.3 The geometrical structures of the devices included in the photolithographic mask. Five different radii with several gap lengths for each were included, resulting in a total of 16 devices to be placed on two separate chips. 121

6.4 Summary of the measured characteristics of some of the germanosilicate microring resonators. 127

6.5 List of some of the critical parameters for germanosilicate ring resonators. The simulated values correspond to the expected parameters based on calculations and the experimental values are extracted from the fit of the analytical function of Eq. (6.20) to the measured transmission spectrum of each device. 129

Chapter 1

Introduction

Since the discovery of fire, light and optics have0 been employed in communicating information. It has been used to exchange information both on the sea and on the ground. Today, information affects every aspect of our lives because of the enormous improvements in the computer and communication technologies [1]. Everyone would agree that our lives would be totally different without computers, cell-phones, internet, satellites, and many other information processing tools. Today, the increasing importance of information access and manipulation, forces us to process it faster, with fewer inaccuracies, at a lower cost, and with a system which consumes less space.

1.1 Milestones in the Field of Photonics

Close connection between physics and communications started after 1876 with the invention of telephone by A.G. Bell. The field of electromagnetism became an important topic at those times. It is an interesting fact that only five years after the invention of the phone, it underwent a rapid commercialization [1]. A similar breakthrough had become possible only after 1960's when T. Maiman demonstrated the first pulsed ruby laser. Providing the coherent light source was one of the major impacts of physics. It stimulated the research in fiber optics resulting

in first low loss (20 dB/km) optical fibers developed in 1970's by F. P. Kapron *et al.* These fibers were designed to operate at 850 nm, the GaAs/$Al_xGa_{1-x}As$ laser wavelength. The development of lasers on InP/InGaAsP materials system operating at wavelengths of 1300 and 1550 nm made it possible to shift the communications wavelengths to this low-loss region. Silica fibers, as a result, were developed to reach losses as low as 0.15 dB/km by 1985, making it possible to establish the first long haul transatlantic optical fiber system that was installed in 1988 [1]. Since then, the capacity of the commercial fibers has increased in accordance with the Moore's law [2] for integrated circuits, i.e. doubling each year.

The next stage in the field of communications and photonics can be identified as the trend of evolving towards planar waveguides instead of relying completely on optical fibers. Although optical fiber components can perform many of the passive optical functions, the notion of planar integration is becoming more and more important. It offers potential technological and economic advantages. The compactness it provides makes reduction of many critical devices down to single chip dimensions possible. Moreover, integrating complex functions into chips, that are made processing a single wafer, reduces the cost abruptly [3]. Above all, the available integrated circuit processing technologies facilitate the use of silicon based materials in the area of integrated optics.

1.2 Why Silicon Based Dielectrics?

Silicon technology was and remains as the most dominant force in electronic integrated circuits and it seems that this will continue in the near future [2, 4]. Si-based technologies offer crucial advantages in terms of both performance and cost, which makes it more attractive over all other competing technologies. The major drawback of this technology has been lack of a light source (Si being an indirect bandgap material), however, recently researchers have demonstrated a continuous-wave Raman silicon laser [5], which has made the technology even more promising.

The work towards implementation of silicon technology in the integrated optics area started ever since the notion of integrated optics was introduced. There are several key factors for this application to be successful. First of all, any candidate technology must provide waveguide structures with low propagation losses. Moreover, it should be compatible with microelectronics device processing and provide high reproducibility with reasonably low cost. The coupling between the optical integrated circuit devices and other elements such as optical fibers, light sources, and photodetectors is another important issue of consideration. Most of the materials used in integrated optics so far are classified as either low index contrast (e.g. silica, $LiNbO_3$, polymers) or high index contrast (e.g. InP, SOI) [6]. The satisfaction of all of the above mentioned requirements simultaneously for both of these systems is a challenging issue. In the low contrast systems the fiber-to-chip coupling efficiency is excellent due to the large size of the single mode waveguides, but they have low integration density since large bend radii (10-30 mm) are required for low loss operation. On the other hand, high contrast systems allow very small bending radii (below 0.5 mm) with low losses, however efficient fiber-to-chip coupling is difficult to obtain due to small waveguide dimensions [7, 8].

In recent years, growing attention has been paid to silicon based dielectrics, such as silicon oxynitrides, silicon nitrides, and semiconductor doped silicon oxides, all combined with the name silica on silicon technology (SOS) [9–11]. This attention has been motivated mainly by their excellent optical properties such as well controlled refractive index and high transparency over a wide range (see Fig. 1.1) [3]. Silicon based dielectrics combine the properties of SiO_2 together with good chemical inertness and low permeability of high-refractive-index materials, e.g. Si_3N_4, germania, etc. Furthermore, the index of refraction of these layers can be easily adjusted continuously over a wide range between 1.45 (SiO_2) – $\sim$2.0. This is a very attractive property as it allows for fabrication of waveguides with desired characteristics of fiber match and compactness [10, 11]. Moreover, the growth of silicon based layers is done by well established standard silicon integrated circuit processing technology, which is also a key point towards low cost mass production.

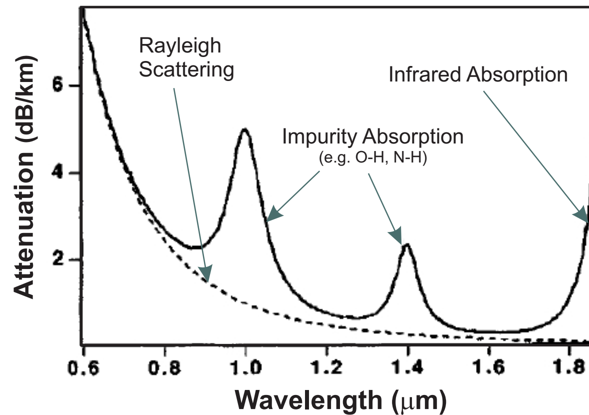

Figure 1.1: Attenuation characteristics of a typical silica fiber guide. (Adapted from [12]).

The major drawback of this technology originates from the relatively high propagation losses introduced by the impurities during the growth of the material [13]. In particular, loss at λ=1.55 μm is known to be caused mainly by N−H and O−H bonds incorporated into the film matrix (see Fig 1.1). The reported values for propagation losses are larger than 2 dB/cm at λ=1.55 μm, although this has not been analyzed systematically [14]. To reduce these loss values, it is common practice to anneal the as-grown layers at temperatures as high as 1100 ℃ for prolonged times [13, 15, 16]. It would be of great interest to obtain silicon based dielectric layers with reasonably low propagation losses in as-deposited form, avoiding the need for the annealing process.

The silicon based dielectrics are deposited using various techniques. The most commonly used growth technologies are plasma enhanced chemical vapor deposition (PECVD) and low pressure chemical vapor deposition (LPCVD). The PECVD process is found to be more efficient in controlled deposition of films with refractive indices below 1.7 [6]. The deposited layers have good uniformity of the refractive index and layer thickness with run-to-run reproducibility. The waveguides fabricated by this technology have the following structure: silicon is used as a substrate and SiO_2 buffer layer is thermally grown on it to act as a lower cladding layer for the silicon based dielectric core film on top of which SiO_x is

deposited to provide symmetric structure [17]. The reported propagation losses of the waveguides vary between 1.5-10 dB/cm ($\lambda = 1.55$ μm) for as deposited films and are reduced to 0.2-0.36 dB/cm for thermally annealed films [6,7,18–20].

The application area of any material system includes variety of integrated optical devices. Among these, microring resonators attract special interest. Recently a lot of research has been carried out for use of microring resonators in integrated optics as all-optical switches, add-drop filters, electro-optic modulators, etc [21–23]. Optical Ring Resonators (RRs) offer useful components for wavelength filtering, multiplexing, switching, and modulation. The key performance characteristics of the RRs includes Free-Spectral Range (FSR), finesse, quality factor, resonance transmission, and extinction ratio. These quantities depend not only on the device design but also on the fabrication tolerance. Current challenges in the field are to produce dielectric microring resonators with low-loss, large free-spectral range and of desired characteristics of resonant wavelength adjustment and filter linewidth [24]. Application of silicon based dielectrics on such devices has recently been studied in detail [25,26] motivated by the fact that these materials are relatively inexpensive and their index contrast is easily adjustable. Moreover, their dimensions are two or three times larger than their semiconductor counterparts, which allows efficient usage of optical lithography without the need for e-beam lithography. Silicon based dielectrics, therefore, offer a promising platform for applications of ring resonator devices [27].

1.3 Contribution of This Work and Organization of the Dissertation

In accordance with the main goal of this work, that relies on the utilization of silicon based dielectrics and their optimization for applications in integrated optics, an emphasis was given to the compositional and optical properties of these materials.

As discussed in Chapter 2, in the first stage of our work we have mutually

investigated the compositional properties of silicon oxide, silicon nitride, silicon oxynitride, germania, and germanosilicate glasses and identified the germanosilicate dielectrics as the most promising candidates for use in integrated optics.

In Chapter 3 we focused on detailed quantitative compositional analysis of the germanosilicate films using Fourier transform infrared spectroscopy. Compositional analysis using FTIR spectroscopy showed that the amount of N−H and O−H related bonds exhibited a drastic decrease with increasing GeH_4 flow rate.

In Chapter 4 we report on a first systematic study of propagation losses for different-index planar waveguides. This study had striking results in which planar waveguides fabricated with germanosilicate core layers showed the lowest propagation loss values reported so far both for as deposited and annealed germanosilicate films at λ=1.55 μm, eliminating the need for costly and cumbersome annealing process. With a further step of improvement of the prism coupling technique, a new approach is proposed for elasto-optic characterization of thin polymer films. This completely new method allows us to determine and to correlate the optical anisotropy and out-of-plane mechanical properties in order to obtain the elasto-optical properties of thin polymer films, for the first time.

The investigations of optical properties of germanosilicate films continued with a focus on their nonlinear properties as described in Chapter 5. Of interest as potential electro-optic devices, we have concentrated on thermally poled low-loss germanosilicate films deposited on fused-silica substrates by PECVD. After optimizing the germane flow rate during deposition, the film thickness, and the poling time for maximum peak nonlinearity, we demonstrated a record peak nonlinear coefficient of ~1.6 pm/V, approximately twice as large as the highest reliable value reported in a thermally poled fused silica glass.

Having optimized the compositional and nonlinear properties of germanosilicate dielectrics, in Chapter 6 we have demonstrated several applications of this technology in the field of integrated optics. Since optical waveguides constitute the building blocks of many integrated optical devices, we had first concentrated on design and optimization of waveguides employing germanosilicates as the core

layers. The final step of our work was to design and implement microring resonator devices based on germanosilicate layers with optimized finesse and quality factors.

Finally, in Chapter 7 we conclude with a summary and discussion of the key results of this PhD work.

Chapter 2

Silicon Based Dielectrics – General Overview

In this chapter, the results on compositional and refractive index characterization obtained on silicon based dielectrics grown by Plasma Enhanced Chemical Vapor Deposition (PECVD) technique are summarized. After a brief description of the PECVD method, results for silicon oxide and silicon oxynitride films are presented, and then an analysis of the effects of adding germanium to these layers are reported.

2.1 Plasma Enhanced Chemical Vapor Deposition

The field of microelectronics has been using chemical vapor deposition (CVD) techniques for several decades for deposition of various dielectrics primarily aiming applications such as insulation, masking, optical guiding, etc. This technique can be defined as a process where thin solid films are grown as a result of chemical reactions of the precursor gases. The PECVD technique in particular, has

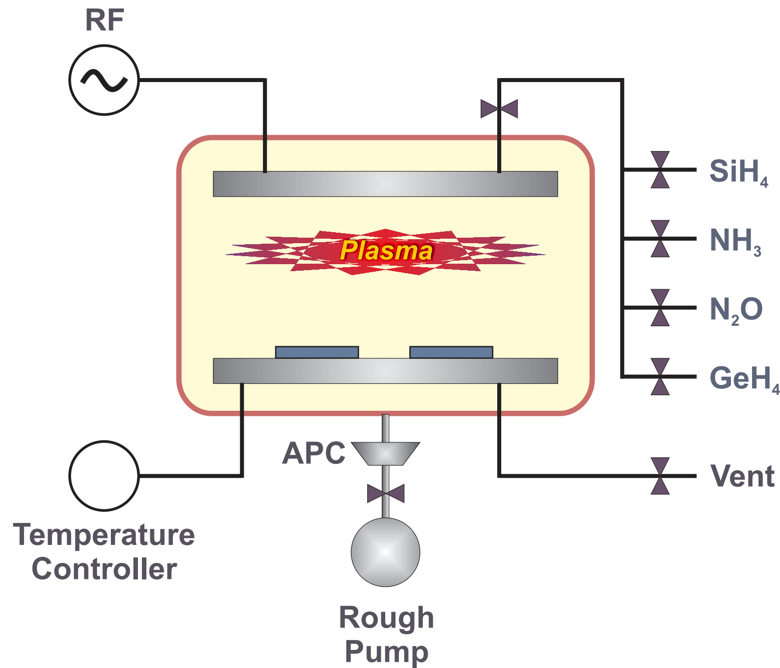

Figure 2.1: PECVD reactor structure.

received wide application in the area of integrated optics. The major advantage of plasma enhanced (or plasma–assisted) CVD comes from its capability of growing films at relatively low temperatures (150–350 ℃) [28]. In conventional CVD processes, the standard temperature of operation is in the range of 700–900 ℃, which limits its applicability to device fabrication in which metallization and other temperature sensitive preocesses are involved. The operation at such low temperatures for PECVD technique is possible due to the addition of electrical energy to the environment in the form of RF power, resulting in glow discharges.

The system used in our studies is a parallel-plate type *Plasmalab 8510C* reactor (see Figure 2.1). The radio frequency (RF) generated glow discharge (plasma) takes place between two electrodes which are separated by 2 cm. The plates are 24 cm in diameter and the RF power that establishes the plasma is applied to the upper electrode while the samples are placed on the bottom grounded electrode that can be heated up to 400 ℃. The system can be operated at a pressure range of 0.1–10 Torr. Applied RF frequency is 13.56 MHz with a maximum power of

300 Watts. The available gases that can be used as precursors for film growth are silane (2% SiH_4/N_2), ammonia (NH_3), and nitrous oxide (N_2O). A germane (2% GeH_4/He) gas line has later been introduced in order to be able to dope the grown films with Ge. The structure of the films grown by this technique is amorphous in nature and their compositional characteristics are to be discussed extensively in the following chapters.

2.2 Silicon Oxide and Oxynitride Layers

The major problem for integrated optics applications in the PECVD grown silicon based layers has been reported to be the incorporation of hydrogen and nitrogen in the form of N–H bonds into the film matrix [7, 29]. Although there have been a considerable number of both compositional and device related studies on these films separately, there has been a lack of systematic analysis comprising all three silicon based layers [30, 31], i.e. silicon oxides, nitrides, and oxynitrides. Namely, the dependence of the optical properties on film composition and growth parameters needs to be established for the whole range of compositions starting from silicon oxide and ending with silicon nitride films. During our M.Sc. study, an attempt was made to establish such a relation, to identify possible drawbacks of the films in the above mentioned range and to possibly eliminate them in a systematic way, for the first time [13]. Their deposition, material characterization, and treatment towards loss minimization, and finally the fabrication and characterization of single-mode waveguides were analyzed. A brief summary of the results of our M.Sc. study is included in this section for the sake of completeness.

The stoichiometry of the PECVD grown layers typically deviates from their "ideal" counterparts. Namely, instead of SiO_2 one obtains SiO_x due to small amounts of hydrogen and nitrogen incorporated into the film, resulting in a refractive index larger than 1.46. For convenience, they will be denoted as SiN_x and SiON, respectively.

In the growth process of the samples, the flow rate of silane was kept constant

Table 2.1: Growth parameters for silicon oxide, nitride, and oxynitride layers.

Silane (2% SiH_4/N_2) Flow Rate	180 $sccm$
N_2O Flow Rate	25–450 $sccm$
NH_3 Flow Rate	0, 15, 30 $sccm$
Process Pressure	1000 $mTorr$
RF Power	10 W
Temperature	250 ℃, 350 ℃

at 180 sccm, while that of ammonia was either 0, 15 or 30 sccm, and the flow rate of nitrous oxide was varied between 0 and 300 sccm (see Table 2.1 for details). The index of refraction and thickness of the grown films were measured by an automated Rudolph Research/AutoEl III ellipsometer at a wavelength of 632.8 nm. Typical accuracy values of the measurements were ± 0.01 and ± 20 Å for the index of refraction and thickness of the films, respectively. In addition, the thickness values of some of the layers were measured by Sloan Dektak 3030ST stylus profilometer.

As seen from Fig. 2.2, the values of the refractive index of both silicon oxide films grown at 250 and 350 ℃, decrease from a value of about 1.56 down to 1.47 with increasing N_2O flow rate. At N_2O flow rates higher than 150 sccm the decrease in the refractive index saturates. The high index region in Fig. 2.2 is due to silicon rich films. As the N_2O flow increases, a large amount of oxygen and some nitrogen is incorporated into the films, resulting in refractive index closer to that of stoichiometric SiO_2. The silicon oxide characterizations were performed at two different growth temperatures of 250 and 350 ℃ in order to compare the qualities of the films grown. It was observed that the growth rate decreases slowly as the substrate temperature is increased. For N_2O flow of 25 sccm, the growth rate at 250 ℃ is 340 Å/min, whereas at 350 ℃ it decreases down to 290 Å/min. This can be regarded as an indication that the films grown at higher temperatures are denser and contain less microvoids, which was also verified by monitoring the wet chemical etch rates of these layers. It is well known that etch rates obtained with wet chemical etch (e.g. HF) are smaller for denser SiO_x films. Therefore, the temperature of 350 ℃ was chosen for the growth of silicon nitride and silicon oxynitride films in order to obtain films suitable for optical

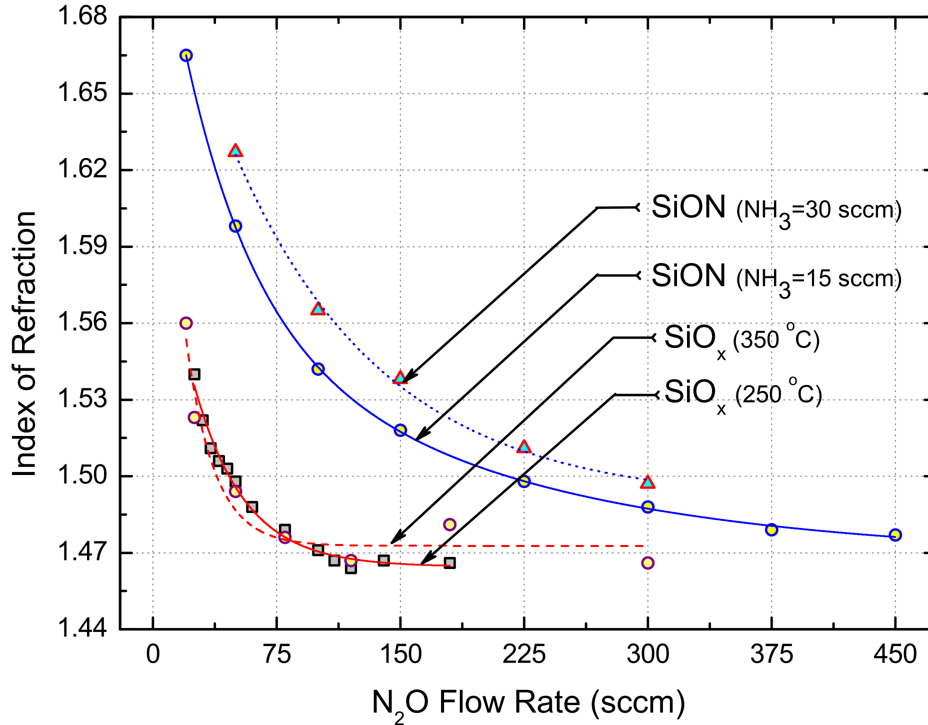

Figure 2.2: Variation of index of refraction of SiO_x and $SiON$ films with N_2O and NH_3 precursor gases flow rates and growth temperature.

applications. Moreover, the hydrogen incorporation into the layers is reported to be less at higher deposition temperatures [28], thus resulting in potentially low propagation loss waveguide materials.

A general trend of decreasing refractive index with increasing N_2O ratio was observed in all cases (see Fig. 2.2) (for both silicon oxide and oxynitride layers), which comes about because of oxygen's greater chemical reactivity compared to nitrogen. In addition, as the flow rate of ammonia was increased, the film index increased due to their higher nitrogen content, thus gaining more resemblance with the silicon nitride layers. It was found that increasing the nitrous oxide flow rate results in an increase of film growth rate as well. Moreover, the deposition rate was observed to be decreasing with increasing ammonia flow rate. The decrease of the growth rate with increase in nitrogen concentration in the film

can be explained by increasing probability of the nitrogen related bonding so that the nitrogen concentration in the film increases [32]. Thus, the layers become more silicon nitride–like, the growth rate of which is smaller than that of silicon oxides [13]. In fact, if we consider the growth rates for these films, they increase in the following order: silicon nitride, silicon oxynitride, silicon oxide, exhibiting a smooth transition of the physical properties of silicon oxynitride from those of silicon oxide to silicon nitride [13, 33].

The compositional properties of these three types of films were investigated via Fourier transform infrared transmission spectroscopy (FTIR). Special attention was given to the absorption band of N−H bond stretching vibration, since its first overtone is known to be the main cause of the optical absorption at 1.55 μm wavelength (the technique is to be discussed in detail in the following chapters) [7, 29]. For silicon oxide films the N−H bond concentration was found to vary between 7.4×10^{21} cm^{-3} and 0.4×10^{21} cm^{-3}, while the same bond variation for silicon nitride layers was between 9.6×10^{22} cm^{-3} and 7.9×10^{22} cm^{-3}. For the silicon oxynitride films, the corresponding variation of the N−H bond concentration was observed to be 0.6–1.7 $\times 10^{22}$ cm^{-3}. It was found that the observed N−H bonds resulted in propagation losses larger than 4 dB/cm. Low-loss waveguides (<1 dB/cm), therefore, were only possible to obtain after an annealing treatment at temperatures higher than 1100 ℃ [13].

2.3 Germanium Doped Layers

During the first stage of this Ph.D work, there were three different precursor gases available for film growth, namely silane, nitrous oxide, and ammonia. Tuning the refractive index of the “optical–grade” layers was possible only through variation of the N_2O gas flow rate at fixed flow of SiH_4 and NH_3. However, during the M.Sc. study [33], it was verified that this gas acts as a primary source for the N−H bonding in the layers, which needs to be eliminated in order to decrease the propagation losses in the waveguides [13]. In order to be able to vary the refractive index of the PECVD grown material without possibly including extra

Table 2.2: Refractive index values for some of the silicon based dielectrics.

Film Type	PECVD Gas Flow Rates (*sccm*) SiH_4	GeH_4	N_2O	NH_3	Refractive Index (λ = 632.8 nm)
SiO_x	180	-	225	-	1.46
SiON	180	-	100	15	1.54
SiON	180	-	225	15	1.50
SiON:Ge	180	50	225	15	1.76
SiO_x:Ge	180	20	225	-	1.49
SiO_x:Ge	180	50	225	-	1.53
SiO_x:Ge	180	90	225	-	1.66
SiO_x:Ge	180	120	225	-	1.94

N−H bonds into the films, we have introduced germane (2% GeH_4/He) gas into the PECVD system. This gas has given us an opportunity to dope the films with *Ge*.

As far as integrated optical applications are concerned, using germane as the core dopant and silica as the cladding, ensures nearly identical characteristics for planar waveguides with the existing fiber technology [15]. Moreover, promising phenomena such as significant UV photosensitivity [34] and second–harmonic generation [35] have already been shown in germanosilicate waveguides, providing great potential for optical applications [36].

As a result, in addition to silicon oxide, silicon nitride and oxynitride films, we gained a capability of growing the following types of dielectric films: germanosilicate (SiO_x:*Ge:N:H*), germane doped silicon oxynitride (*SiON:H:Ge*), and germanate (GeO_x:*N:H*) glasses. Table 2.2 gives examples for some of the refractive index values obtained by combination of different flow rates of the available gases (as measured by ellipsometry at λ = 632.8 nm).

In addition to the index of refraction, we focus on the compositional properties of the grown layers and mainly aim for low N−H bond concentration in the films with possibly high refractive index. In light of these criteria, various dielectrics (germanosilicates, germanium doped oxynitrides, and germanate glasses) were investigated. An important initial finding was that the germanate and high–germanium–content glasses are easily oxidized shortly after the deposition. FTIR

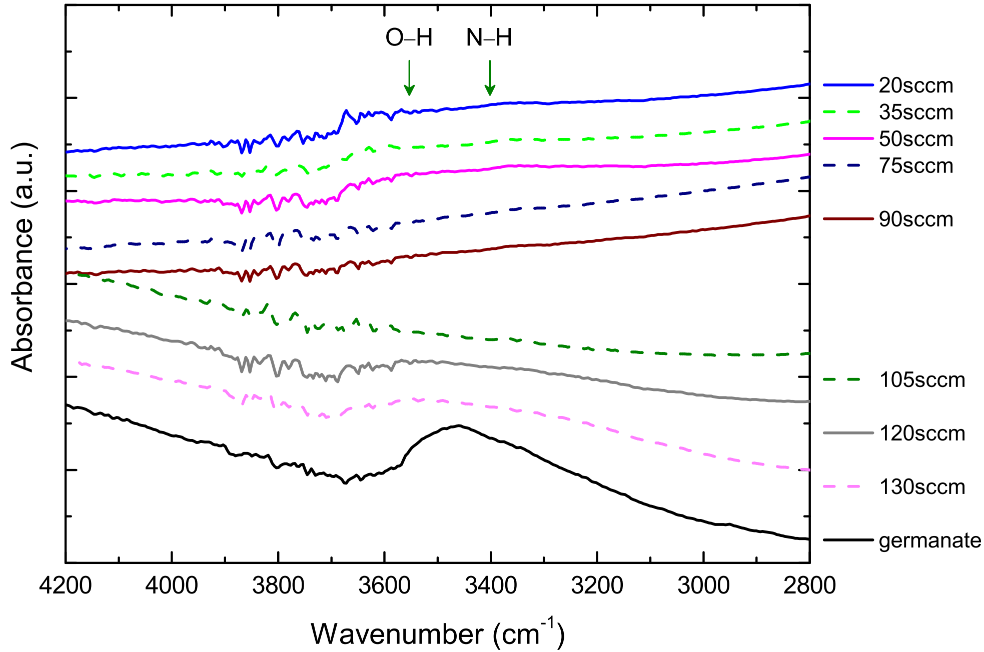

Figure 2.3: Comparison of the O−H and N−H stretching bands as obtained with FTIR absorbance spectroscopy for germanosilicate and germanate films as a function of GeH_4 flow rate at fixed SiH_4 and N_2O flows.

analysis shows large amounts of O−H bonds indicating the possible absorption of water vapor. This property ruled out the possibility of their usage as a dielectric material for integrated optical devices. FTIR spectroscopy also shows that the most suitable material, compared to the previously mentioned ones due to their minimum N−H bond content (comparing materials with the same index of refraction) turned out to be the germanium–doped silica (or germanosilicate $SiO_x{:}Ge$) films. Germanate (GeO_x) glasses contained the largest amount of the N−H and O−H (see Fig. 2.3), which decreased in silicon oxynitride layers and were minimum in germanosilicate glasses. Figure 2.3 shows the variation of the O−H and N−H stretching bands with the GeH_4 flow rate for germanosilicate films. The quantitative analysis of these bonds in germanosilicate films will be a subject of another chapter. At this point, the most important finding was that the films suitable for integrated optics are germanosilicates, rather than silicon oxynitride and Ge doped oxynitride films, due to their low N−H bond content

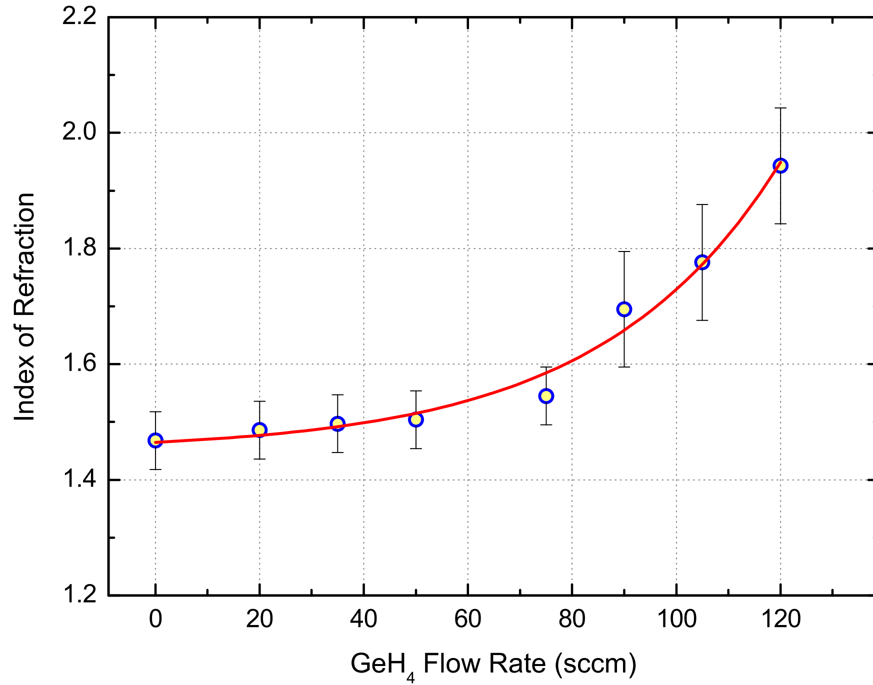

Figure 2.4: Variation of index of refraction for germanosilicate layers with GeH_4 flow rate.

and hence low propagation losses.

The effect of adding Ge into SiO_x layers on refractive index of the material is of great interest. Therefore, the variation of index of refraction with GeH_4 flow rate was characterized (see Fig. 2.4). The samples analyzed were grown at 350 ℃, with 10 W RF power, under 1 $Torr$ pressure, and using constant 180 sccm SiH_4 and 225 sccm N_2O flow rates. The GeH_4 flow was varied between 0 and 120 $sccm$ resulting in a steady refractive index increase from 1.46 up to 1.94, as measured by an ellipsometer ($\lambda = 632.8$ nm). The index of refraction was lower at low GeH_4 flow rates and increased with increasing Ge incorporation into the film. The observed growth rates, however, did not show a significant change with the change of germane flow. A small decrease from about ∼340 Å/min down to ∼290 Å/min was identified.

Thus, as an outcome of these preliminary results, we decided to concentrate

on germanosilicate glasses. These dielectric layers will further be investigated in terms of suitability for integrated optical applications. One of the methods to be used for the characterization of these layers will be the prism coupling technique. This method is to be discussed in detail In Chapter 4.

Chapter 3

Germanosilicate Dielectrics I: Compositional Analysis Using FTIR

Based on analysis of Section 2.3, germanosilicate is selected to be the material system on which further investigations are to be carried out. Considering the goals of our work, in addition to characterizing the optical properties of germanosilicate films, we would benefit much from learning about the composition of grown layers. Thereby, an attempt is made towards relating the material composition to film characteristics such as index of refraction and optical loss. For this purpose, widely-used Fourier Transform Infrared (FTIR) spectroscopy together with prism coupling methods (PCM) will be employed. Below, some general remarks on infrared spectroscopy are given, followed by the description of the experimental setup. Subsequently, the results obtained from a thorough compositional analysis are presented.

3.1 General Remarks on FTIR Spectroscopy

Infrared (IR) absorption makes use of the vibration of atoms in molecules. The spectrum is obtained by having IR radiation pass through a sample and analyzing the absorption features at particular energies, which in turn correspond to the frequency of vibration of a part of a molecule in the structure [37].

A polyatomic molecule consisting of N atoms has $3N-6$ ($3N-5$ if it is linear) *normal modes* of vibration [38]. Actually, the total vibrational motion of the molecule is resolved into components which consist of mixture of angle–bending and bond–stretching vibrations called as the normal modes (see Figure 3.1). In a normal mode of vibration, all the nuclei move in phase, have the same frequency of vibration, and in general move with different amplitudes. In this motion, the center of mass of the molecule does not move and the molecule as a whole does not rotate. Moreover, any vibrational motion of this polyatomic molecule is expressible in terms of linear combination of its normal modes. Here it should be mentioned that, in addition to the basic stretching and bending vibrations, there are other termed kinds such as rock, twist, scissors, wag, and breathing, which are frequently used to describe the group vibrations of molecules [33].

As an illustrating example one can look at the possible transitions in a vibrational spectrum that are possible for diatomic molecules. In the framework of quantum mechanics, this is determined by the interaction of the dipole moment

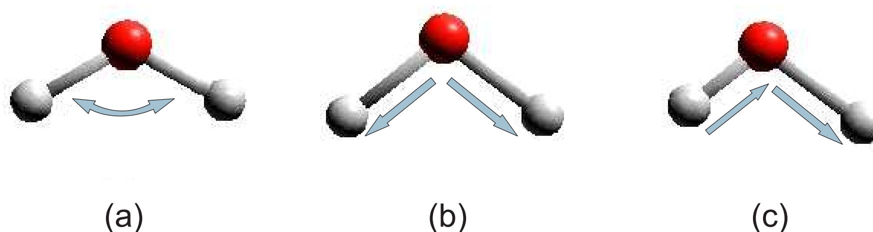

Figure 3.1: Illustration of (a) bending, (b) symmetric stretching, and (c) antisymmetric stretching vibrations for a polyatomic molecule.

of the molecule with the electric field component of the incident radiation [38]. Explicitly, the transition probability is given by the square of the transition dipole moment $\vec{R}_{nm}$, given by

$$\vec{R}_{nm} = \int \Psi_n^* \hat{\mu} \Psi_m d\tau, \tag{3.1}$$

where $\hat{\mu}$ is the electric dipole moment operator and

$$\hat{\mu} = \sum_i q_i \vec{r}_i, \tag{3.2}$$

where the sum is carried over all nuclei and electrons of the molecule, q_i is the charge and $\vec{r}_i$ is their position vector. The transition dipole moment $\vec{R}_{nm}$ can be thought as the oscillating electric dipole moment due to the transition.

For a diatomic molecule of two different species the electric dipole moment μ is non–zero and varies with distance, x. This variation is expressed as a Taylor series expansion about equilibrium point x_e, referring to equilibrium internuclear distance, as

$$\vec{\mu} = \vec{\mu_e} + \left(\frac{d\mu}{dx}\right)_{x_e} (x - x_e) + \frac{1}{2!}\left(\frac{d^2\mu}{dx^2}\right)_{x_e} (x - x_e)^2 + ... \tag{3.3}$$

Now, for a molecule in a given electronic state, the transition dipole moment takes the form of

$$\vec{R}_{v'v''} = \vec{\mu}_e \int \Psi_{v''}^* \Psi_{v'} dx + \left(\frac{d\vec{\mu}}{dx}\right)_{x_e} \int \Psi_{v''}^* (x - x_e) \Psi_{v'} dx + ... \tag{3.4}$$

The first term of this equation is zero because the vibrational wave functions for different v (states) are orthogonal. The second term is non–zero if

$$\Delta v = \pm 1, \tag{3.5}$$

which imposes a vibrational selection rule. Another condition for the non–vanishing of this term is that the dipole moment should be a function of the internuclear distance x. This means that homonuclear diatomic molecules, e.g. N_2 and H_2, have zero dipole moments for all bond lengths and, therefore, show no vibrational spectra. For the higher terms of Eq. (3.4) we would expect that their contribution is small and can thus be neglected. If they are neglected, the harmonic oscillator model would give us only single vibrational absorption at a

specific frequency; otherwise, the higher terms do give rise to *overtone transitions* of $\Delta v = \pm 2, \pm 3, ...$ (i.e. $v_0 \rightarrow v_2, v_0 \rightarrow v_3$, etc.) with rapidly decreasing intensities.

The final remark is about the selection rules for infrared active vibrations. The main rule is that any normal mode will have a vibrational spectrum only if its displacements cause a change in the dipole moment. The process of this determination of the vibrational modes that are infrared active is performed by making use of group theory, i.e., identifying the symmetry properties of the molecule and possible vibrations that result in dipole moment change.

3.2 Experimental Setup

Throughout our experiments a *Bomem H&B Series* FTIR spectrometer has been used (see Fig. 3.2). Its basic operation relies on a Michelson interferometer, which is built into the spectrometer. The advantages of this technique over the other spectroscopic methods derive from using a large aperture at the signal input and having the entire spectrum at once at the output. Namely, using a large aperture results in a large energy throughput and is called the *Jacquinot* advantage. Moreover, the ability to simultaneously process the entire spectral range in a single scan gives an advantage known as the *Fellget* advantage [33].

As a source in the spectrometer, a Nerst solid glower is used, which radiates continuous light in the mid–infrared region in accordance with blackbody radiation. The light is then directed to the beam splitter of the Michelson interferometer, after which it is reflected from two perpendicular plane mirrors one of which is movable. The radiation reaching the detector (pyroelectric deuterium tryglycine sulfate: $DTGS$) consists of two components that have a path difference of δ with its magnitude changed by displacing the movable mirror. The intensity of light measured at the detector, which represents the interference between the two beams, is of the form of

$$I(\delta) = \int_0^\infty B(\omega) \cos(2\pi\omega\delta)\, d\omega, \tag{3.6}$$

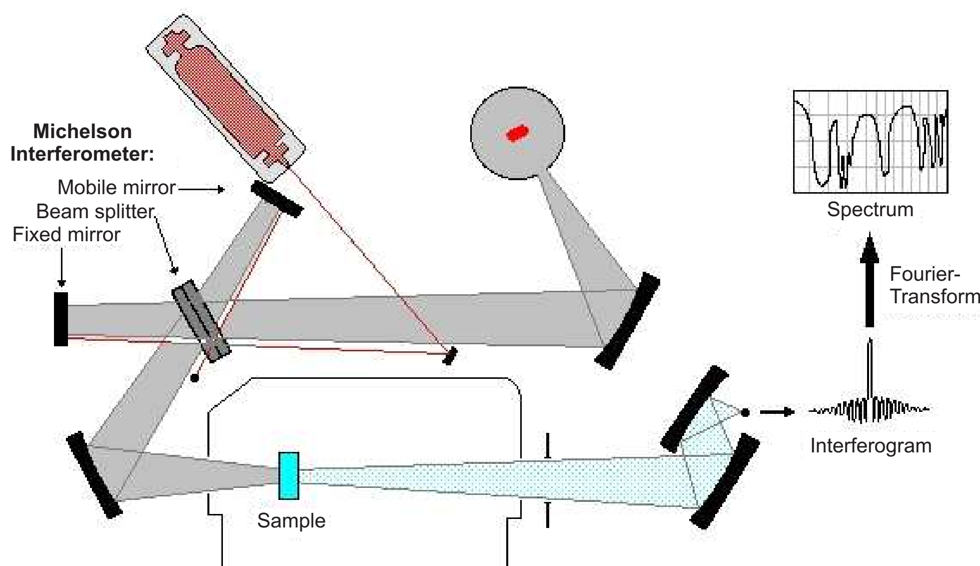

Figure 3.2: The FTIR experimental setup used for infrared absorbance measurements.

where ω is the wavenumber and $B(\omega)$ is the source intensity at that wavenumber. This expression is also called as *interferogram* and its Fourier transform gives the desired spectrogram of the transmitted intensity as a function of the wavenumber, i.e. $B(\omega)$ given by

$$B(\omega) = 2 \int_0^\infty I(\delta) \cos(2\pi\omega\delta) d\delta. \tag{3.7}$$

The process of this transformation is performed by a computer.

In order to understand the significance of the spectrum, it is necessary to closely look into what it represents. When we pass radiation of intensity I_0 through a sample, the transmitted intensity is I. The ratio I/I_0 is called the transmittance of the sample. If we have a sample of thickness t and concentration c of bonds that absorb light, we can define *absorbance* A, which is directly proportional to above quantities as

$$A = \alpha t c, \tag{3.8}$$

where α is a constant of proportionality called as *molar absorptivity* having dimensions of inverse concentration $\times$ length. The absorbance (A) and transmittance

(T) are related by

$$A = \log_{10}\left(\frac{I_0}{I}\right) = \log_{10}\left(\frac{1}{T}\right), \tag{3.9}$$

which is known as *Beer's law.* In the obtained IR spectrum the total intensity of a specific absorption band is measured by the integrated intensity, which is carried out over the band of interest. The integrated absorption coefficient is defined by (see e.g. [39])

$$\int_{band} \alpha(\omega) d\omega. \tag{3.10}$$

The results of Eqs. (3.6)–(3.10) are to be used in the following sections for determination of the relevant bond concentrations.

3.3 IR Analysis of Germanosilicate Layers

A series of germanosilicate films was grown by using parallel–plate type *Plasmalab 8510C* PECVD reactor. The layers were grown on high resistivity silicon wafers with polished sides at 350 ℃, under a pressure of 1 *torr*, and with an RF power of 10 W at a frequency of 13.56 *MHz*, applied to the plates with a diameter of 24 cm (see Table 3.1 for summary). Silane (2% SiH_4/N_2) and nitrous oxide (N_2O) gas flow rates were kept constant at 180 and 225 *sccm*, respectively, while that of germane (2% GeH_4/He) was varied between 0 and 70 *sccm*.

The compositional analysis of the germanosilicate films were performed by making use of Bomem H&B Series FTIR spectrometer. The spectra were obtained

Table 3.1: Growth parameters for germanosilicate films used in FTIR measurements.

Parameter	Value
Silane (2% SiH_4/N_2) Flow Rate	180 *sccm*
N_2O Flow Rate	225 *sccm*
Germane (2% GeH_4/He) Flow Rate	0–70 *sccm*
Process Pressure	1000 *mTorr*
RF Power	10 W
Temperature	350 ℃

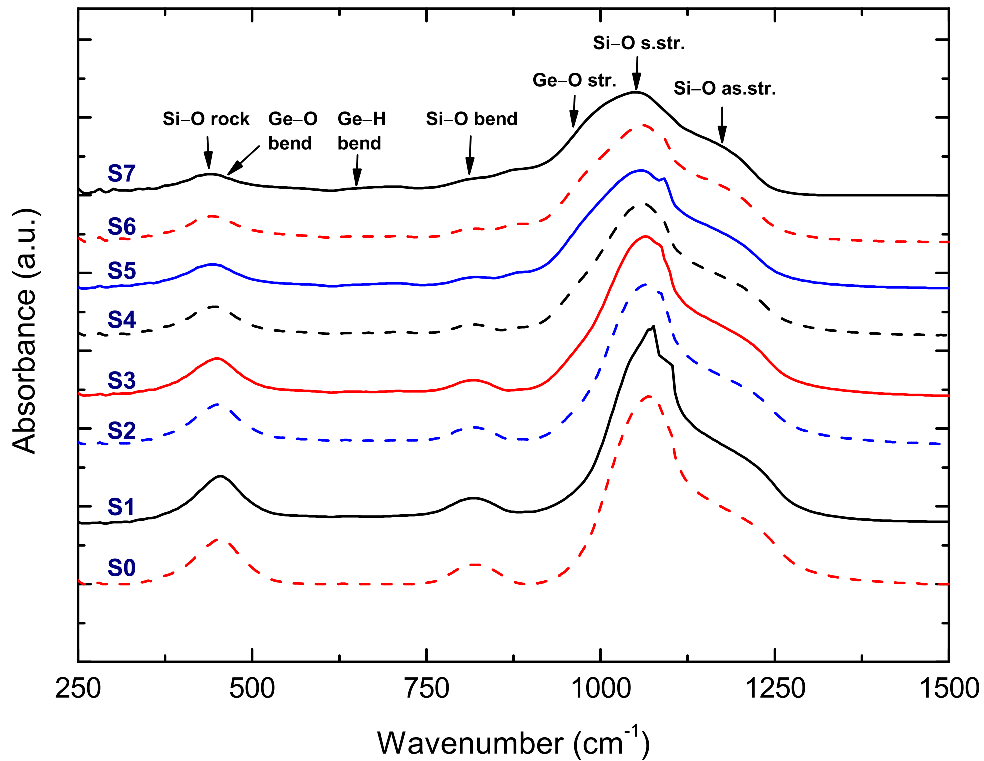

Figure 3.3: Infrared absorption spectra of germanosilicate samples at 250–1550 cm^{-1} range with the the following GeH_4 flow rates; s0: 0, s1: 5, s2: 10, s3: 20, s4: 30, s5: 50, s6: 60 and s7: 70 *sccm*.

in the 5500–250 cm^{-1} range with 8 cm^{-1} resolution. The thicknesses of the SiO_x:Ge layers deposited for FTIR characterization were between 1.5 and 2.5 μm. Eight samples, s0–s7, with corresponding GeH_4 flow rates of 0 (i.e. SiO_x), 5, 10, 20, 30, 50, 60, and 70 *sccm* were used for compositional characterization. Thickness normalized absorbance spectra of the samples in 250–1500 cm^{-1} range are shown in Fig. 3.3.

All the samples show a dominant absorption feature around 1050 cm^{-1} which can be resolved into Si–O symmetric and asymmetric stretching and Ge–O stretching vibrations [40, 41] at frequencies of about 1065, 1150 and 980 cm^{-1}, respectively. Si–O rocking and bending vibrations were identified at ∼450 and ∼820 cm^{-1}, while Ge–O and Ge–H bending vibrations were observed at ∼420 and ∼650 cm^{-1}, respectively.

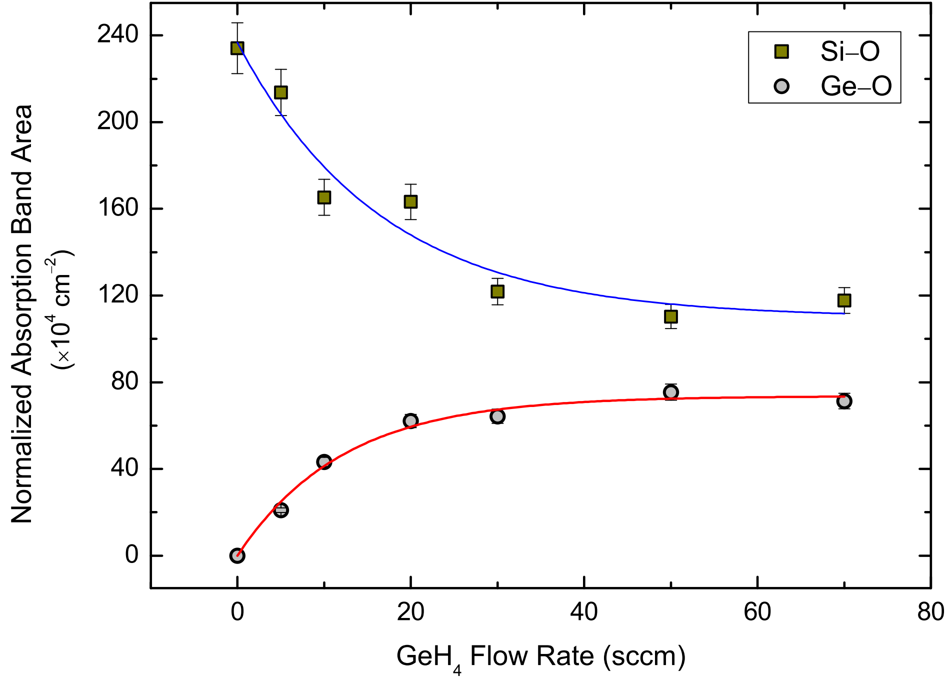

Figure 3.4: Variation of normalized absorption band area for Si−O and Ge−O related bonds with increasing GeH_4 flow rate.

Analysis of the oxygen bond concentration was performed by integrating over the relevant bands. The bands were decomposed using nonlinear curve fitting, assuming that the peaks are in the form of symmetric Gaussians. The results of this analysis are plotted in Fig. 3.4. The normalized integrated absorption $\left[\int_{band} \alpha(\omega) d\omega\right]$ of the Si−O bonds exhibited a gradual decrease, while that of Ge−O bonds showed a steady increase as a function of germane flow rate. Both reached saturation at a GeH_4 flow rate of about 50 *sccm*. Assuming that the infrared absorption cross section for the bonds of interest are similar, it can be stated that *Si* and *Ge* are incorporated into the film matrix at nearly equal concentrations for GeH_4 flow rate of 50 *sccm* and larger, in the range investigated.

The most striking result of the FTIR analysis was that the observed amount of both N−H and O−H bonds decreased with increasing GeH_4 flow rate (see Fig. 3.5) [42]. The N−H stretching vibrations were observed at ∼3380 cm^{-1}, GeO−H

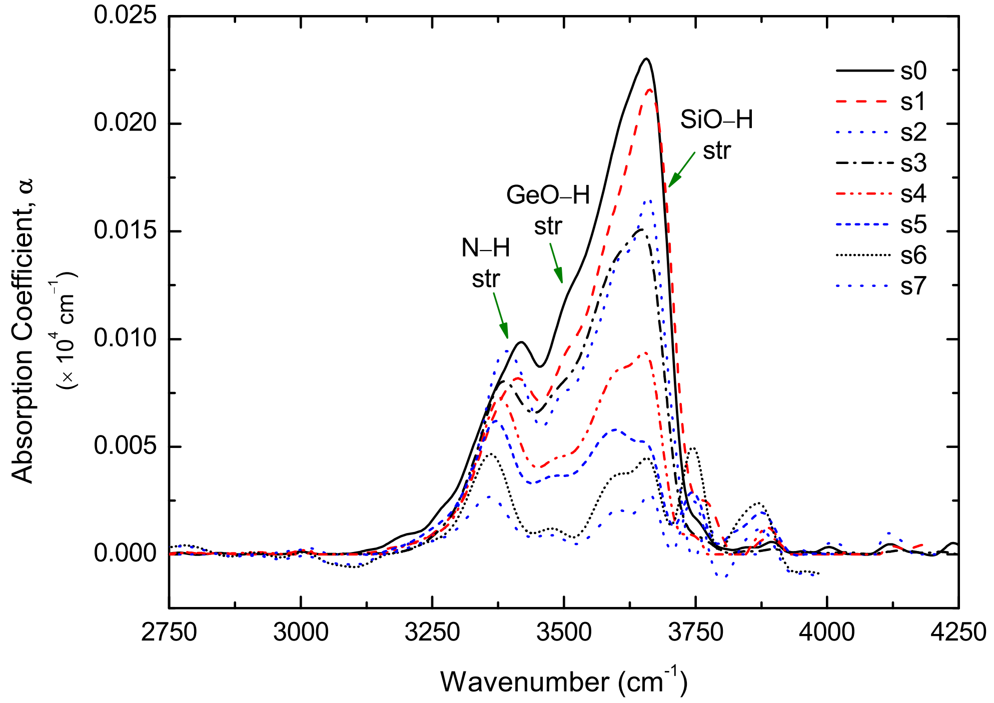

Figure 3.5: FTIR absorption coefficient, α vs incident wavenumber for the germanosilicate samples in the N$-$H and O$-$H absorption band region.

stretching vibrations at ~3470 and ~3515 cm^{-1}, and finally SiO$-$H stretching vibrations at ~3600 and ~3665 cm^{-1} [43]. As the GeH_4 flow rate in the grown samples increased, the N$-$H stretching vibrational frequency shifted about 30 cm^{-1} towards lower frequencies, while that of GeO$-$H and SiO$-$H remained constant.

The vibration band of N$-$H bond stretching is of special interest for us, since it is the main cause of the optical absorption at 1.55 μm wavelength for the optical waveguides that we aim to fabricate. Thereby, special attention was paid to its properties and evolution for the studied samples. The N$-$H and O$-$H bond concentrations were calculated for all the grown layers by using the method of Lanford and Rand [39], by the expression

$$[X-H] = \frac{1}{2.303\ \sigma_{X-H}} \times \int_{band} \alpha(\omega)\ d\omega, \tag{3.11}$$

where σ_{X-H} is the absorption cross section for the N$-$H or O$-$H bonds, $\int \alpha(\omega) d\omega$

is the normalized absorption area of the band, and $\alpha = \left(\frac{2.303}{t}\right) A$ is the absorption coefficient, A being the absorbance and t the film thickness [32]. The integration is carried over the band of consideration, which was decomposed using nonlinear curve fitting and assuming that the peaks are in the form of symmetric Gaussians. The absorption cross section value $\sigma_{N-H} = 5.3 \times 10^{-18}\ cm^2$ used in our calculations was obtained by Lanford & Rand [39] through a resonant nuclear reaction and the uncertainty of the calibration technique that they had proposed is reported to be about ±15% [44]. The corresponding value for O−H bonds was $\sigma_{O-H} = 1.5 \times 10^{-21}\ cm^2$, obtained by Rostaing *et al.* [45]. In spite of the relatively large uncertainty for the O−H bond absorption cross section, we believe that the results obtained can be safely used in the relative comparison of O−H bond concentrations of the samples. For other quantities such as peak wavenumber (ω), full width at half maximum ($FWHM$), and normalized absorption band area ($\int \alpha d\omega$) of each absorption band we estimate typical uncertainty values of $\pm 5\ cm^{-1}$, $\pm 5\ cm^{-1}$, and ±4 %, respectively [13]. The results of the calculations of concentrations are plotted in Fig. 3.6 and those for the N−H bonds are summarized in Table 3.2.

As seen from the figure, the N−H bond concentration has decreased from $0.43{\times}10^{22}\ cm^{-3}$ down below our detection limit of $0.06{\times}10^{22}\ cm^{-3}$, by a factor of seven as the GeH_4 flow rate increased from 0 (silicon oxide) to 70 sccm. As for the O−H bonds, their concentration showed a sharp decrease, as well from about $2.27{\times}10^{22}\ cm^{-3}$ down to $0.23{\times}10^{22}\ cm^{-3}$, by a factor of ten in the same germane flow range. The observed decrease of these bonds has an important impact on propagation losses at $\lambda = 1.55\ \mu m$ of the waveguides grown using germanosilicate films. This issue is going to be further investigated by prism coupling technique and is to be discussed in the next chapter.

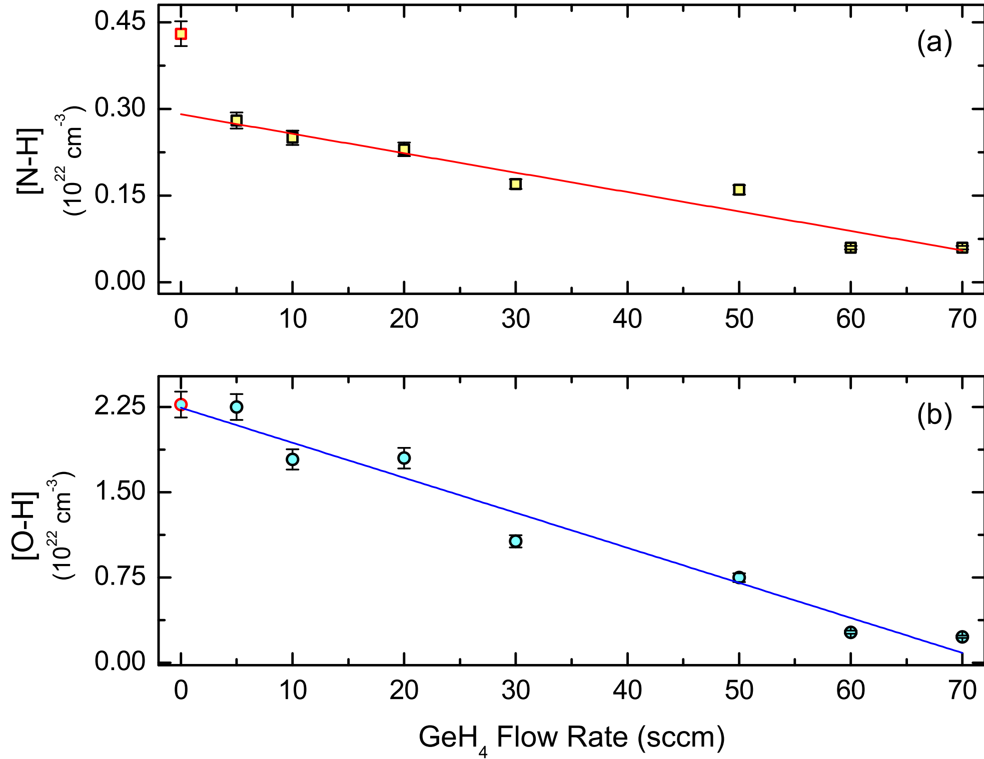

Figure 3.6: Variation of calculated N−H (a) and O−H (b) bond concentrations for germanosilicate samples with increasing GeH_4 flow rate.

Table 3.2: N−H bond str. concentration calculation details for germanosilicate films by using FTIR transmittance spectroscopy.

GeH_4 Flow Rate (sccm)	Central Frequency (cm^{-1})	FWHM (cm^{-1})	α_{max} (cm^{-1})	Sum of Norm. Band Area ($\times 10^4$ cm^{-2})	N−H bond Concentration ($\times 10^{22}$ cm^{-3})
0 (oxide)	3433	229	93	5.23	0.43
5	3416	176	80	3.44	0.28
10	3395	132	92	3.00	0.25
20	3392	145	78	2.79	0.23
30	3380	126	69	2.13	0.17
50	3370	139	61	2.07	0.16
60	3357	101	29	0.71	0.06
70	3353	124	25	0.75	0.06

Chapter 4

Germanosilicate Dielectrics II: Index of Refraction and Propagation Loss Measurements Using PCM

Optical characterization techniques are crucial for investigation of thin film properties. Among various methods, prism coupling technique has received much interest due to several advantages it offers. Development of optical waveguide techniques has provided a convenient method for measuring the refractive indices and thicknesses of thin dielectric films. Due to the ease of operation and high measurement accuracy, the prism waveguide coupler has been used to determine the refractive index and birefringence of thin films as well [48–50, 52], making this method superior to standard ellipsometry. The prism waveguide coupler is particularly suitable for isotropic and anisotropic thin film studies because of the quantitative character of the information obtained.

In this chapter, the prism coupling method will be described in detail. After the prism coupling basics the description of the method for optical propagation loss measurements is presented. Next, the propagation loss characteristics of the germanosilicate films are investigated prior to a report on the effects of annealing of germanosilicate dielectrics. Finally, a study on the refractive index of the materials upon application of external stress is presented. This study resulted in development of a new technique for evaluation of the elasto-optical properties of thin films and results obtained for several polymer waveguides are presented.

4.1 Basic Principles of the Prism Coupling Method

Since the introduction of the prism coupling method (PCM) by Tien and Ulrich in 1970's, it has become a widely used tool for refractive index, film thickness and optical loss measurements in thin film structures [48–51]. In this method, the film of interest has to be in the form of a planar waveguide and support at least two modes at the measured wavelength. As depicted in Fig. 4.1, a beam of incoming light is coupled into the waveguide (i.e. waveguide modes) via a prism and is monitored at the other edge of the waveguide as the angle of incidence (α) is changed.

The refractive index of the prism used (n_p) has to be larger than that of the guiding film (n) and a load has to be applied onto the prism in order to achieve the optical coupling. The maximum power transfer (~80 %) to the mode is achievable when the gap between the prism and guiding film is about $\lambda/4$ [49]. Each mode of the waveguide is excited individually at a specific angle of incidence. The excited modes can be traced visually as streaks along the waveguide. Hence, the observation of the modes can either be done by detecting the light at the waveguide output, or the reflecting light from the base of the prism, and/or using a screen on which m–lines are formed [49]. In either method, one obtains the coupling angle data at which each of the waveguide modes is excited. Based on these data, one can evaluate the index of refraction and thickness of the film.

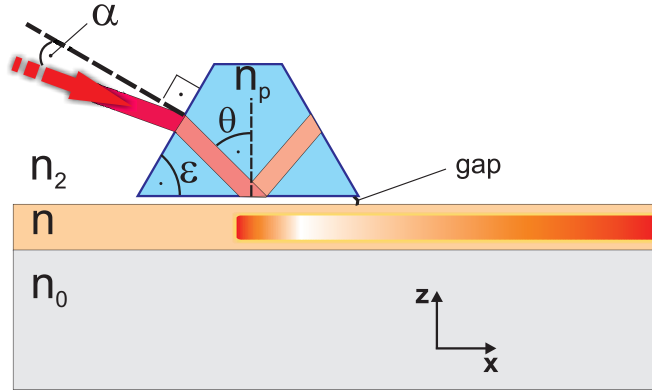

Figure 4.1: Schematic representation of a prism coupler.

The optical coupling of an incident beam is possible when the angle of incidence exceeds the critical angle and the evanescent waves that extend beyond the prism base penetrate into the waveguide. The condition for total internal reflection is satisfied when [50]

$$\theta > \arcsin\left(\frac{n_2}{n_p}\right). \tag{4.1}$$

This gives rise to standing wave formation inside the prism, the k vector of which is given by

$$\begin{aligned} \vec{k_0}n_p &= n_p\left(k_x\ \hat{x} \pm\ k_z\ \hat{z}\right) \\ &= n_p\left(k_0 \sin\theta\ \hat{x} \pm\ k_0 \cos\theta\ \hat{z}\right). \end{aligned} \tag{4.2}$$

Outside the prism the field decays exponentially, but the z component of the wavevector remains the same. As evident from Eq. (4.2) and Fig. 4.1, the wavevector k depends on the angle of incidence α, which enables one to adjust and possibly match the velocity of propagation of the wave in the prism with that in the guide.

The parameters effecting the coupling condition such as prism angle (ϵ) and refractive index (n_p) are critical. They define the range of the propagation constant that are possible to excite in a waveguide. The expression relating the propagation constant ($\beta = n_p \sin\theta$) along the prism base with the angle of incidence α

and the prism angle ϵ is given by

$$\beta = \sin\alpha\ \cos\epsilon + \sqrt{\left(n_p^2 - \sin^2\alpha\right)}\ \sin\epsilon. \tag{4.3}$$

Evaluation of the film index and thickness relies on the measurement of the coupling angles of waveguide modes. Here, we assume two successive modes[1] (μ and ν), for which the observed propagation constants β_μ and β_ν are related to the unknown index (n) and thickness (W) by the dispersion equation for planar dielectric waveguides in the form of [49]

$$kW\sqrt{n^2 - \beta_m^2} = \Psi_m(n, \beta_m), \tag{4.4}$$

where

$$\Psi_m(n, \beta_m) = m\pi + \phi_0(n, \beta_m) + \phi_2(n, \beta_m) \tag{4.5}$$

and

$$\phi_j(n, \beta_m) = \arctan\left[\left(\frac{n}{n_j}\right)^{2\rho}\left(\frac{\beta_m^2 - n_j^2}{n^2 - \beta_m^2}\right)\right]^{1/2} \tag{4.6}$$

with n being the refractive index of the film, W the film thickness, β_m the propagation constant of the mth mode, ρ polarization ($0 \equiv$ TE, $1 \equiv$ TM), and j defining the boundary ($0 \equiv$ upper, $2 \equiv$ lower).

Inserting β_μ and β_ν into Eqs. (4.4)–(4.6) enables kW to be eliminated, yielding a single equation for n that can be written in the following form

$$n^2 = F\left(n^2\right), \tag{4.7}$$

where

$$F\left(n^2\right) \equiv \frac{\left(\beta_\mu^2\Psi_\nu^2 - \beta_\nu^2\Psi_\mu^2\right)}{\left(\Psi_\nu^2 - \Psi_\mu^2\right)}. \tag{4.8}$$

The Eq. (4.8) cannot be solved explicitly, however the solution can be found by iterative techniques. Namely, the series $n^2_{[q]}$ for q = 1,2,3,... is calculated by the recursion formula [49]

$$n^2_{[q]} = F\left(n^2_{[q-1]}\right). \tag{4.9}$$

[1]The treatment of a case with a larger number of modes requires a different approach [49], it was implemented in the numerical code developed for this study but will not be discussed here.

This series converges to the solution of interest

$$n^2 = \lim_{q\to\infty} n_{[q]}^2 \tag{4.10}$$

provided that

$$\left|\frac{\partial F}{\partial\left(n^2\right)}\right| < 1\ . \tag{4.11}$$

Numerically, it can be shown that the statement is true in case that the first term of the series $(n_{[0]})^2$ satisfies the following conditions

$$n_{[0]}^2 > \beta_\mu^2 \qquad and \qquad n_{[0]}^2 > \beta_\nu^2\ . \tag{4.12}$$

These conditions are physically reasonable and can always be satisfied by a suitable choice of the initial term as a guess value. The solution of the series has an alternating behavior and, after ten to twenty steps of iteration, an error of less than 10^{-6} is reached. Solving for the unknown refractive index n by this method and inserting it into Eq. (4.4) one obtains the thickness value W of the film. The implementation of all of the above routine has been realized with a Mathcad™ code which uses directly the measured data as input giving the desired values as an output.

4.2 Propagation Loss Measurements and PCM

As a guided wave travels through a waveguide it experiences an attenuation or loss ($\propto e^{-\alpha L}$). It is common to describe optical loss in terms of dB/cm and is defined as the logarithm of the power (intensity) ratio [53, 54]

$$Loss\ (dB/cm) = \frac{1}{L} 10 \log \left(\frac{P_{in}}{P_{out}} \right), \tag{4.13}$$

where $L\ (cm), P_{out},\ and\ P_{in}$ are the waveguide length, output and input power, respectively (see Fig. 4.2).

The measured total loss is the sum of the individual losses due to different mechanisms. These mechanisms include scattering losses credited to surface roughness or scattering centers, radiation losses due to the leakage of the mode into the substrate or bends, and material losses such as vibrational absorption, being particularly relevant in our material system.

There are a number of different methods for the measurement of the propagation losses via PCM. Among these, the most common one is the measurement of the optical power at the output (P_{out}) for several lengths of propagation (L) at fixed detector distance, the so called "moving prism" method (Fig. 4.2, case

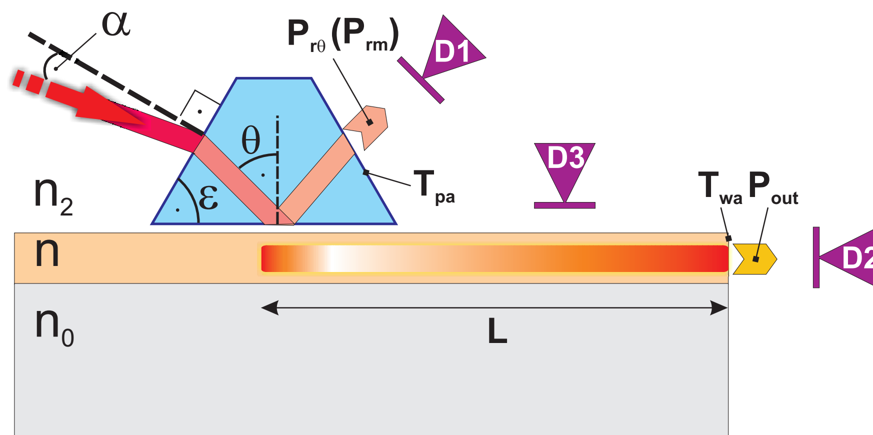

Figure 4.2: Schematic representation of the commonly used propagation loss measurement techniques based on prism coupling.

D2). The challenging issue in this technique is the difficulty in achieving identical coupling at each L. This issue was overcome by using a load cell (see Fig. 4.17), guaranteeing identical coupling condition [55].

Another method is to monitor the scattering loss on the surface of the waveguide by capturing an image of the formed streak and making an image analysis of it [56]. This technique was tested for our configuration as well, however it was found to be useful only for propagation losses larger than $\sim$5 dB/cm. A slight modification of this method results in two new techniques. Namely, one can observe the scattered light streak either with a fiber or free space optics and a detector (Fig. 4.2, case D3) at different L and thereby obtain propagation loss values. Yet, it was difficult for these methods to be implemented and obtain reliable results. Additional technique that was investigated was to analyze the intensity of the mode captured at the output of the waveguide by a CCD camera, again with limited success. Consequently, at a wavelength of 1.55 μm the method to be used for slab waveguide propagation loss measurement was determined to be the "moving prism" technique.

For propagation loss measurements at $\lambda = 632.8$ nm an additional method of Ramponi *et al.* [57] was tested. It was not applicable at $\lambda = 1.55$ μm due to the geometry and the small area of the Ge-photodetector. A large area (1 cm^2) Si photodetector was included in the setup for this purpose. In this method the reflected light intensity at one edge of the prism is measured together with the intensity of the propagated light (Fig. 4.2, cases D1 & D2). The propagation loss (dB/cm) value is evaluated with the following relation

$$Loss = \frac{1}{L} \times 10 \log \left[\frac{(P_{r\theta} - P_{rm})}{P_{out}} \times \frac{T_{wa}}{T_{pa}} \right], \tag{4.14}$$

where L is the length of propagation of the light, $P_{r\theta}$ and P_{rm} are the maximum and minimum power of the reflected light, while P_{out} is the power of the propagated light (Fig. 4.2). T_{wa} and T_{pa} are the Fresnel transmission coefficients at

the waveguide–air and prism–air interfaces given for our case by [58]

$$T_{pa} = 1 - \left[\frac{n_p \cos(\theta_1) - \cos(\theta_2)}{n_p \cos(\theta_1) + \cos(\theta_2)} \right]^2 \quad \text{for TE polarization,} \tag{4.15}$$

$$= 1 - \left[\frac{\cos(\theta_1) - n_p \cos(\theta_2)}{\cos(\theta_1) + n_p \cos(\theta_2)} \right]^2 \quad \text{for TM polarization,} \tag{4.16}$$

and

$$T_{wa} = 1 - \left(\frac{n-1}{n+1} \right)^2 . \tag{4.17}$$

Here, θ_2 is the angle of maximum reflected light (usually around 0°) and θ_1 is given by

$$\theta_1 = \arcsin \left[\frac{\sin(\theta_2)}{n_p} \right] . \tag{4.18}$$

Having briefly discussed the propagation loss measurement methods for slab waveguides based on PCM in general and the ones used in this study, the measurement results for germanosilicate slab waveguides are reported in the next sections.

4.3 Experimental Setup

A schematic representation of the prism coupling measurement setup built in our laboratory is given in Fig. 4.3. Alignment optics includes a polarization rotator and an analyzer in addition to a chopper. A beam splitter was also included to calibrate the relative orientation of the laser beam with respect to the coupling prism and was used to establish the origin of the angular displacement. The coupling pressure was adjusted by a micrometer holder in contact with a calibrated spring system that allowed us to monitor the applied force onto the prism.

The operational procedure of the PCM is simple. The linearly polarized monochromatic light, of 632.8 nm wavelength from a He–Ne laser (or at 1.55 μm from a DFB laser), with either transverse electric (TE) or transverse magnetic (TM) polarization, was incident onto the prism. The waveguide and the coupling prism were rotated on a high precision motorized rotary stage on which they were mounted under computer–control. All the measurements were performed by using a single prism to determine the coupling angles of each mode.

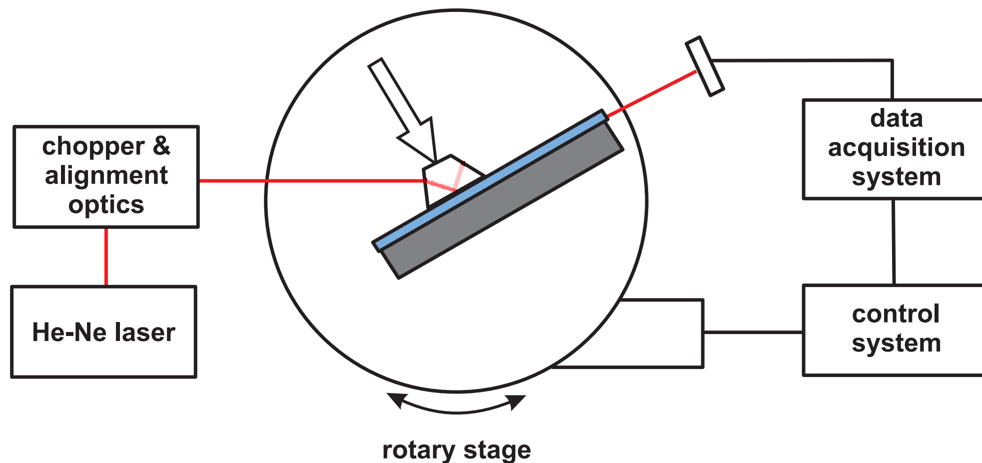

Figure 4.3: Experimental setup for measuring the coupling angles. The laser beam is incident on the coupling prism. The prism coupler setup is mounted onto a high precision rotary stage with stepper motor having a precision of better than $\pm$ 0.01°.

Initially, both symmetric trapezoid shape and right angle prisms made of SF–14 with base angles (ϵ) of 60° and refractive index (n_p) of 1.7561 ($\lambda = 632.8$ nm) were tried. Guided intensity was measured on the opposite side of the waveguide by a Si photodetector as a function of the incident angle (α). In order to minimize the noise, we used a lock–in amplifier which was connected to a computer that also controlled the rotary motor. From the angles, at which local intensity maxima are observed, the refractive index and thickness of the measured film can be obtained by solving the waveguide mode equations for TE and TM polarizations (see Section 4.1) [59–61].

Attention must be paid towards properly aligning the coupling prism. The repeatability of the measured coupling angle has been checked and found to be less than ±0.01°. Typical error in the refractive index and thickness values is found to be less than ±0.0002 and ±0.3 %, respectively. All the experiments were carried out at a constant temperature of 21.0 ± 1.0 ℃.

4.4 Propagation Loss and Refractive Index Analysis of Germanosilicate Layers

Planar germanosilicate layers are conventionally grown by RF sputtering [35], sol–gel methods [15], powder melting [43, 46] or plasma enhanced chemical vapor deposition (PECVD) techniques [36]. As–deposited SiO_x:Ge optical waveguides grown with these methods all share the shortcomings of having relatively large propagation losses at wavelengths of 632.8 nm and 1.55 μm. In particular, loss at $\lambda = 1.55$ μm is known to be caused mainly by N−H and O−H bonds incorporated into the film matrix [13, 33] while loss at 632.8 nm is mainly due to scattering mechanisms [29]. Although there was previously no systematic study of propagation loss in germanosilicate planar waveguides, the reported values range between 3.5−10 dB/cm [15, 34] at $\lambda = 632.8$ nm and are larger than 2 dB/cm at $\lambda = 1.55$ μm [14]. To reduce the loss, it is common practice to anneal the as–grown layers at temperatures as high as 1100 ℃ for prolonged times [15, 16]. Recently, Zhang *et al.* [16] reported CVD grown germanosilicate planar waveguides with propagation losses of about 2 and 1 dB/cm at wavelengths of 632.8 and 1550 nm, respectively. However, due to low index contrast, almost half of the mode power in those waveguides propagate in the cladding material, the effect of which is not taken into account in the previously reported loss values.

In this section, we report on systematic characterization of as–grown germanosilicate waveguides. The layers were grown by standard PECVD technique by using silane, germane and nitrous oxide as precursor gases. It was shown in the previous section (Section 3.3) that increasing the germane flow rate leads to reduction of the hydrogen related bonds and thus decrease in the propagation loss is to be expected [13].

The samples to be used for this study were grown with identical parameters with those used for FTIR analysis. The refractive index of the films were measured by prism coupling technique [48] at $\lambda = 632.8$ nm and 1550 nm (see Section 4.1) and the film thicknesses were determined by the same method and by the stylus profilometry (see Fig. 4.4 and Table 4.1).

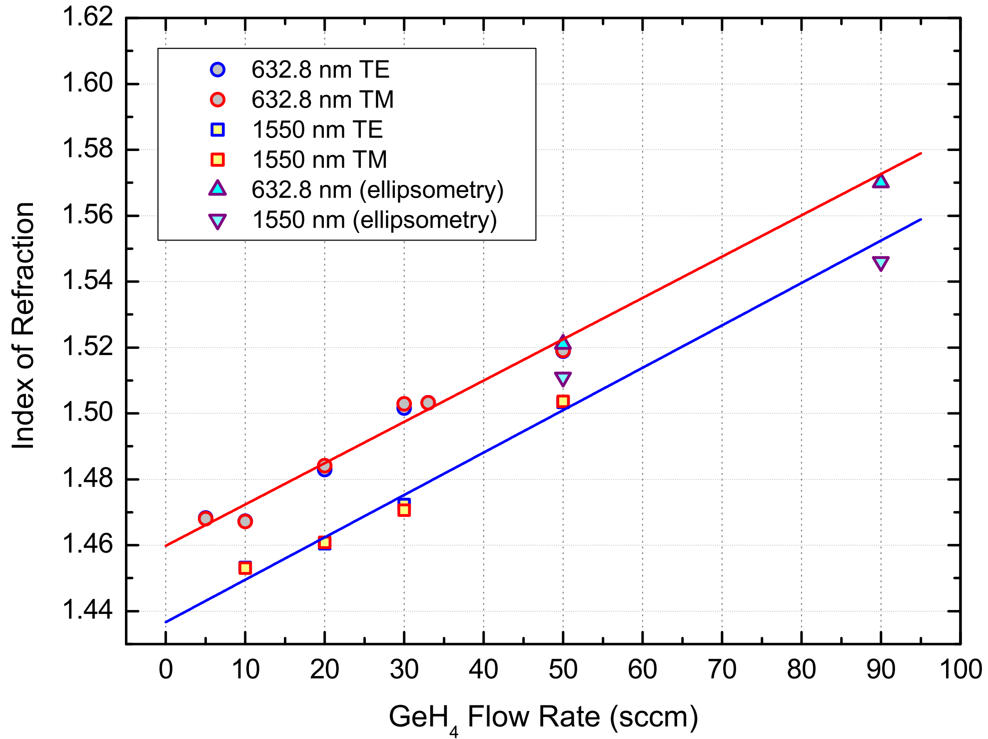

Figure 4.4: Variation of the index of refraction for germanosilicate layers with GeH_4 flow rate at $\lambda = 632.8$ and 1550 nm for both TE and TM polarizations.

Table 4.1: Summary of the measurements of index of refraction for germanosilicate layers for TE & TM polarization at $\lambda = 633$ and 1550 nm, with varying GeH_4 flow rate.

GeH_4	633 nm		1550 nm	
$(sccm)$	TE	TM	TE	TM
5	1.4683	1.4681	-	-
10	1.4673	1.4672	1.4533	1.4530
20	1.4830	1.4841	1.4604	1.4609
30	1.5016	1.5029	1.4723	1.4706
33	1.5032	1.5032	-	-
50	1.5189	1.5191	1.5033	1.5037
50*	1.522 ±0.005		1.511 ±0.005	
90*	1.570 ±0.005		1.546 ±0.005	

*– as measured by ellipsometry.

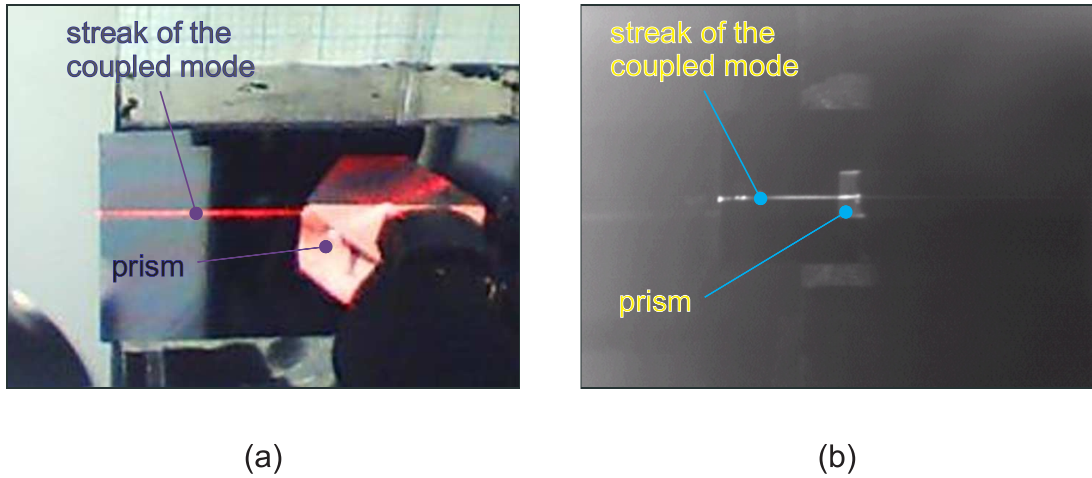

Figure 4.5: Photographs of the experimental configuration for prism coupling technique used for index of refraction and propagation loss measurements at (a) λ= 632.8 nm and (b) 1.55 μm.

At $\lambda = 1550$ nm the corresponding refractive indices were measured to vary between 1.4530–1.5033 and 1.4527–1.5032 for TE and TM polarizations, respectively. Variation of the refractive index for investigated germanosilicate films as measured by prism coupling method is shown in Fig. 4.4 and summarized in Table 4.1. For these films the growth rates were observed to increase gradually from 370 to 440 Å/min with increasing GeH_4 flow rate.

The propagation losses of the waveguides were measured by using prism coupling technique. The waveguides were grown on oxidized silicon wafers with a SiO_2 thickness of 9.8 μm. The core layer thicknesses were varied between 4−6 μm, by using the same parameters as the samples used in FTIR characterization. At $\lambda = 1.55$ μm the moving prism method was used, in which light was coupled into the waveguide at different lengths and the output power was monitored at the end of the slab waveguide. At $\lambda = 632.8$ nm the method of Ramponi *et al.* [57] was employed, in which a single prism and measurement of reflected and transmitted light are used to determine the propagation losses (see Section 4.2). The pictures of experimental configuration for the both types of measurements are shown in Fig. 4.5.

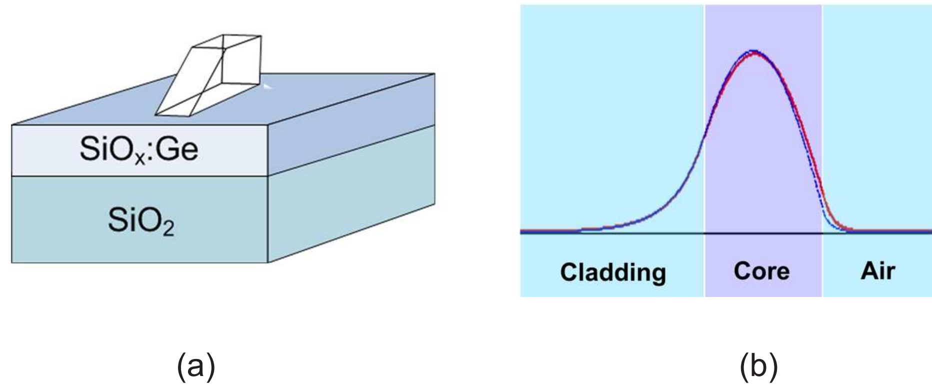

Figure 4.6: A schematic picture of the mode profile of (a) the slab waveguides used for propagation loss measurements using prism coupling method along with (b) a simulated mode profile.

In order to compare the propagation losses of our films, care was taken to take the confinement factor of each waveguide into account. Depending on the index contrast and thicknesses of the layers, some fraction of the total time averaged power travels in the core layer of the waveguide and the remaining power propagates in the cladding layer a schematic representation of which is given in Fig. 4.6 (b). In Fig. 4.6 (a) the prism coupler and waveguide structure is sketched. This issue can be overcome by normalizing the measured loss to identical predetermined fraction of the total power propagating in the core layer (P_{core}), given by [53]:

$$\frac{P_{core}}{P_{total}} = \frac{\displaystyle\int_0^{t_{core}} E_y(x) H_x^*(x)\ dx}{\displaystyle\int_{-\infty}^{\infty} E_y(x) H_x^*(x)\ dx} \ . \tag{4.19}$$

With this approach, loss values of germanosilicate planar waveguides with different index contrast and thicknesses can be compared to each other. In this work, the fraction of power travelling in the guiding layer was chosen to be same as in the waveguides studied by Zhang *et al.* [16]. The results of the loss analysis for three representative waveguides grown with different germane flow rates are summarized in Table 4.2. For purpose of completeness, raw values of the measured loss rates for TE polarization at $\lambda = 1.55\ \mu m$ are 0.55 $\pm$0.06, 0.37 $\pm$0.10 and

Table 4.2: Propagation loss variation with GeH_4 flow rate for three representative germanosilicate planar waveguides at $\lambda = 1.55$ μm.

Sample no.	GeH_4 flow rate (sccm)	N−H bond concentration ($\times 10^{22}$ cm^{-3})	Propagation loss (dB/cm)	
			TE	TM
S1	5	0.28	0.32 ±0.03	0.22 ±0.04
S2	10	0.25	0.20 ±0.05	0.18 ±0.02
S5	50	0.16	0.14 ±0.06	0.18 ±0.07

0.27 ±0.11 dB/cm for the samples $s1$, $s2$ and $s5$, respectively. The measured propagation loss values at $\lambda = 632.8$ nm for the same samples at TE polarization are 0.20 ±0.02, 0.34 ±0.17, and 6.46 ±0.04 dB/cm, respectively. The observed trend of propagation loss increase at $\lambda = 632.8$ nm is similar with the results available in the literature. Specifically, as the Ge content of the layers increase the propagation loss increases as well due mainly to scattering mechanisms [34,47]. As for the propagation loss values at $\lambda = 1.55$ μm, they are in agreement with our expectations based on FTIR analysis. The normalized propagation loss rates showed a decrease by a factor of two, while approaching our measurement limit, and following the decreasing N−H bond concentration [27].

In summary, we have grown germanosilicate layers using the PECVD technique. Compositional analysis using FTIR spectroscopy showed that the amount of N−H and O−H related bonds exhibited a drastic decrease with increasing GeH_4 flow rate. Planar waveguides fabricated with germanosilicate core layers showed the lowest propagation loss values reported so far both for as deposited and annealed layers at $\lambda = 1.55$ μm [16], eliminating the need for costly and cumbersome annealing process [27].

4.5 Effects of Thermal Annealing on Germanosilicate Layers

Although in the previous section we have demonstrated the lowest propagation loss values for as–deposited germanosilicate layers [27], it would be interesting to see the effects of thermal annealing, that is usually used for these type of layers. While we do not need to further reduce the propagation losses by annealing, it is important to investigate its effects on the properties of these dielectric films.

For this purpose, several germanosilicate films were grown by PECVD technique with identical parameters with the films investigated in the previous sections. The GeH_4 flow rate of the samples was varied between 0 and 120 *sccm* resulting in thicknesses between ∼0.5 and ∼0.7 μm, as measured by the stylus profilometer (see Table 4.3). The samples were annealed in a N_2 environment at 1000 ℃ for one hour, ramping up from room temperature and back for a total annealing time of 10 hours.

In order to observe the distribution of the atoms in the dielectric layer upon annealing, secondary ion mass spectroscopy (SIMS) data of the films were obtained (see Fig. 4.7). According to the results, for the as–deposited germanosilicate layers (Fig. 4.7 (a)) the concentration was uniform for O, Ge, and Si throughout

Table 4.3: List of the germanosilicate samples investigated by secondary ion mass spectroscopy.

Sample no	Growth Parameters			Film Thickness	Annealing Temperature
	GeH_4 (*sccm*)	SiH_4 (*sccm*)	N_2O (*sccm*)	(μm)	(℃)
simsio	0	180	225	∼0.70	1000
sims1	20	180	225	∼0.63	1000
sims2	50	180	225	∼0.60	1000
sims3	90	180	225	∼0.48	1000
sims4	90	180	225	∼0.48	as–deposited
sims5	120	180	225	∼0.46	1000

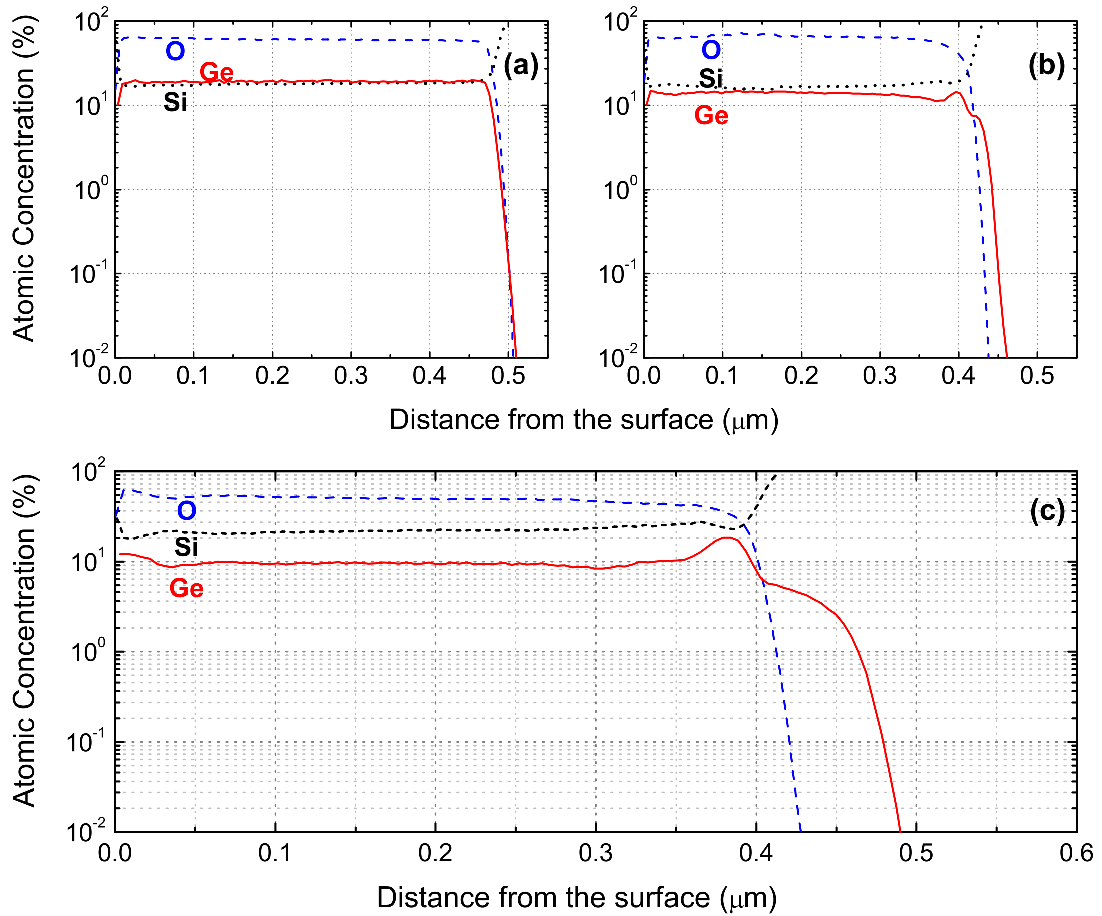

Figure 4.7: SIMS profiles for the (a) as deposited GeH_4= 90 sccm , (b) GeH_4= 90 sccm and annealed at 1000 ℃, and (c) GeH_4= 120 sccm and annealed at 1000 ℃ samples.

the film. As had been estimated by FTIR analysis (Fig 3.6), the atomic concentrations of Ge and Si were equal (∼20 %) and that of O atoms was about ∼60 % (GeH_4= 90 sccm). Upon annealing (Fig. 4.7 (b)), Ge and Si seem to diffuse inside the germanosilicate film in order to compensate for the initial imbalance of the stoichiometry (due to minor impurities such as H and N). Being a fast diffuser in oxide, the excess Ge in the film precipitated towards the silicon substrate, some of it slightly diffusing into Si. It was evidenced that, upon availability of excess Ge in the matrix, precipitation results in formation of a Ge–rich layer at the interface (Figs. 4.7 (b) and (c)). The thickness of this layer

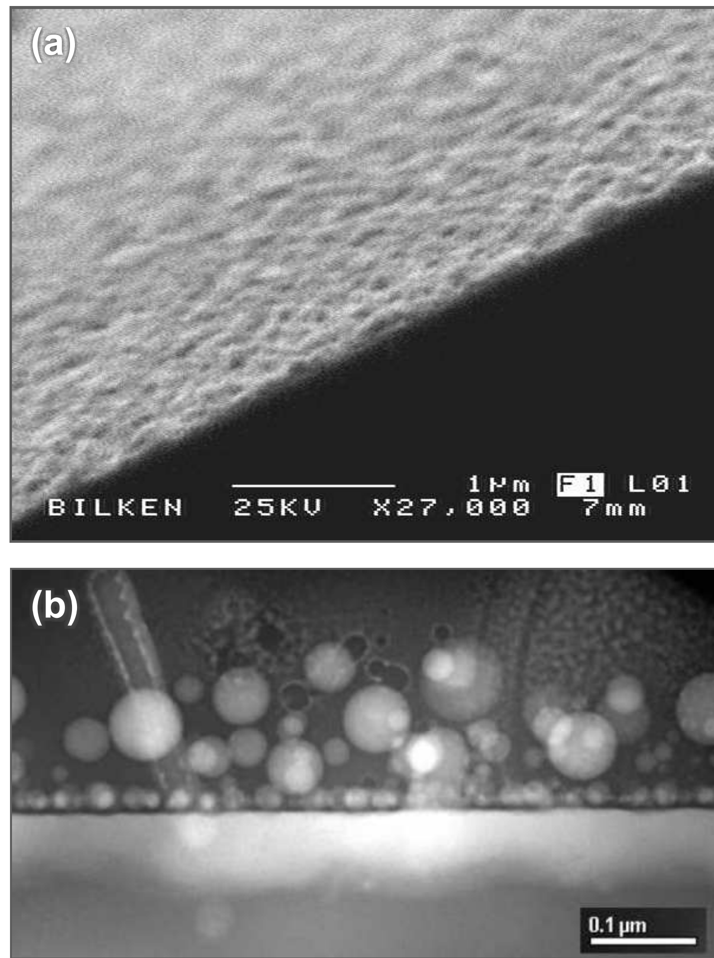

Figure 4.8: (a) Scanning electron and (b) transmission electron microscopy images of the *Ge* precipitate formed at the silicon/dielectric interface for the sample *sims3*.

was found to be determined by the excess amount of *Ge* and varied from few to 100 nm. This issue was further confirmed by microscopic techniques. In the first case, the sample *sims3* was etched in dilute hydrofluoric acid (HF). Since the germanosilicate film dissolves in HF we expected the *Ge*–rich precipitate to remain in the interface, as was confirmed by electron microscopy (Fig. 4.8 (a)).

Further analysis of this precipitate was done by transmission electron microscopy (TEM). This technique further proved the above arguments. That is, segregation of *Ge* at the interface was validated and image of the interface is

given in Fig. 4.8 (b). An important outcome of this analysis was the formation of *Ge* nanocrystals within the dielectric layer, size of which depend on the initial *Ge* concentration and annealing conditions. Analysis of these layers became a subject of another project and is out of the scope of this study.

As for the part relevant to integrated optical devices, attention should be paid when thermal treatments are to be applied to germanosilicate films since the segregation of *Ge* can cause extra unwanted propagation losses in the waveguides. In fact, minor precipitation of *Ge* on the interface was noticed even for as–deposited layers that had been grown for long durations ($>$ 2 hrs.) at 350 ℃.

4.6 Improvement of the Prism Coupling Method

In the course of our study the prism coupling technique has been used extensively. Prism coupling measurements are often complicated by the softness of the films under investigation when stress is applied to the prism to couple light into the waveguides (see Section 4.1). Although this technique has been used for more than 30 years, the dependence of the refractive index, film thickness, and birefringence on the applied stress was not examined. The applied pressure is not an issue if the waveguides investigated have hardness comparable with that of the prisms (glass) used, e.g. germanosilicates. However, the effect of the applied stress is expected to become pronounced when “softer” layers are to be analyzed by prism coupling method (PCM). We have faced such problems during our study and due to lack of necessary investigation in the literature we have focused on the problem. An attempt was made in order to investigate the effects of the applied stress onto the prism and film, and possibly to develop a procedure for the elimination of complications arising from pressure application to the prism and to measure optical properties of some polymer films, for the first time. As a concluding remark we report on a newly developed approach for the determination of elasto–optical constants.

4.6.1 Stress Effects in Prism Coupling Measurements of Thin Polymer Films

A growing number of investigations are currently being carried out on polymeric amorphous materials, because of their potential properties for photonic applications [61–64]. While many kinds of polymers are used in integrated optical devices and in the microelectronics industry, polystyrene (PS), polymethyl–methacrylate (PMMA), and benzocyclobutane (BCB) are among the most promising [65, 66]. Polymers are typically spin-coated onto substrates where the spin-coating and curing processes may introduce in-plane orientation of polymeric chains. It has been proposed that this is due to a biaxial tensile stress caused by substrate

confinement when the solvent evaporates [67]. This leads to a molecular ordering resulting in in-plane and out-of-plane optical anisotropy for the thin polymer films, as was confirmed by several investigations analyzing optical anisotropy, for films with thicknesses in the range of a few micrometers [68, 69]. To study optical and mechanical properties of polymeric systems, birefringence measurements have been used for a long time [70, 71]. The most important origin of birefringence in polymeric thin films is the chain orientation of molecules comprising the polymer which depends on the method of preparation of the thin film. As discussed above, intrinsic stress during sample preparation is also related to the chain orientation. Finally, extrinsic stress applied during the measurement process may influence the observed stress considerably.

To prepare optical waveguide structures for PCM measurements, fabricating thin films is an important first step. PMMA, BCB and PS are all well suited for fabricating excellent polymer waveguide layers by means of spin coating [61]. In this work, PMMA and PS were obtained from Sigma–Aldrich. The molecular weight (Mw) of PMMA and PS were 15 000, and 150 000, respectively. The PMMA and PS polymers were dissolved in chloroform at 15 wt% and 6 wt%, respectively. The polymer solution obtained in this manner was prepared by spin coating from the solution at 3000 and 2000 rpm for 40 seconds on a SiO_2 coated Si wafer. The films were then cured at a temperature of 110 ℃ for 30 minutes. BCB thin films were spin–coated at spin speeds of 5000 rpm for 40 seconds. Fine control of the film thickness was best obtained by adjusting the spin speed. The BCB polymer is supplied as a metasilyene solution of the pre–polymer. The pre–polymer Cyclotone 3022–46 was obtained from Dow Chemical Company for this purpose. These samples were cured in an oven under nitrogen atmosphere at 250 ℃ for 60 minutes. The substrates were silicon slices of 3 cm $\times$ 1.5 cm with CVD grown SiO_2 layers. The thickness of the SiO_2 layers was 7.2 μm and the refractive index was 1.4568 at 632.8 nm. PMMA, PS, and BCB layers had thicknesses of 2.30, 2.37, and 2.38 μm , as measured by stylus profilometer (*Sloan Dektak 3030ST*), respectively.

4.6.2 Measurement Results and Discussion

The planar polymer waveguides were characterized for their refractive index, film thickness and birefringence. In the experiments, two types of prisms were used: A symmetric trapezoid prism and a right angle prism. An example of the coupled intensity as a function of rotation angle for both prisms is shown in Fig. 4.9.

As is clearly observed in Fig. 4.9 (a), the right angle prism gives broad peaks that are shifted with respect to those obtained by the symmetric trapezoid prism. The broadening of the peaks results in lower precision in the exact determination of the mode coupling angle leading to larger errors in the refractive index and film thickness. The shift of the mode coupling angle results in loss of accuracy in determination of the mode coupling angle and hence in the refractive index and film thickness. The application of loading force on the right angle prism results in the rotation of the prism about an axis through the coupling edge

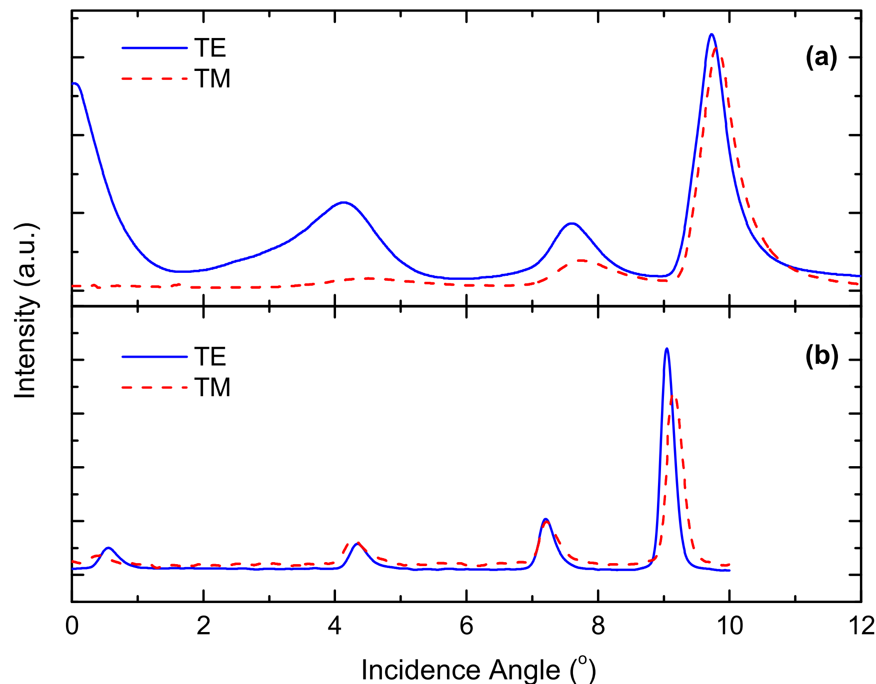

Figure 4.9: Coupled light spectrum for both (a) triangle and (b) trapezoid shaped prisms for PS films.

during the measurement, due to the softness of the underlying polymer film. Coupled with a local reduction of thickness under the prism in the coupling region, this leads to both broadening and shift of the observed peaks. Repeated measurements show that the coupling spectrum with narrower coupling peaks is obtained using a symmetric trapezoid prism (Fig. 4.9 (b)). Symmetric trapezoid prism was used throughout the rest of these experiments. The results showed that symmetric trapezoid prisms are more suitable for measurement of refractive index and thickness using prism coupling methods in thin film polymer waveguides.

With the introduction of the prism coupling method by Tien and Ulrich the possibility of the coupling strength causing a shift and broadening of the modes due to presence of the prism in the vicinity of the film has been argued [49, 50]. Decrease of the air gap that originates from the dust particles and is located between prism and the film due to the applied pressure has been seen as the source of this artifact. Recent theoretical analysis made to estimate the angular shift observed in m–lines prism coupling method by Monneret *et al.* [72] shows that for $SrTiO_3$ prisms and a film with refractive index of 2.27, the shift results in an index change of 5×10^{-5}, which is well below our precision. In our experiments, the prism used is of lower refractive index and the index contrast between the film and the prism is low, which should result in even smaller changes in the refractive index [49]. Additionally, the decrease of the air gap and thus the coupling efficiency is a function of the mechanical properties of the film under investigation. Our thin film polymers are softer than the ordinary glassy dielectric materials [73]. Therefore, it is reasonable to assume that decreasing of the air gap thickness with applied pressure is small in the range of the thickness variations of the polymer films used in this work [74]. Figure 4.10 shows coupling intensity dependence on applied force.

It can be seen from the figure that the pressure is critical in getting optimum coupling efficiency. When the air gap between prism and polymer film is about a fraction of λ, maximum energy is transferred into the polymer waveguide [75]. However, it should be noted that as long as there is sufficient signal to noise ratio, accurate measurements of the coupling angles can be made under a variety of applied stresses.

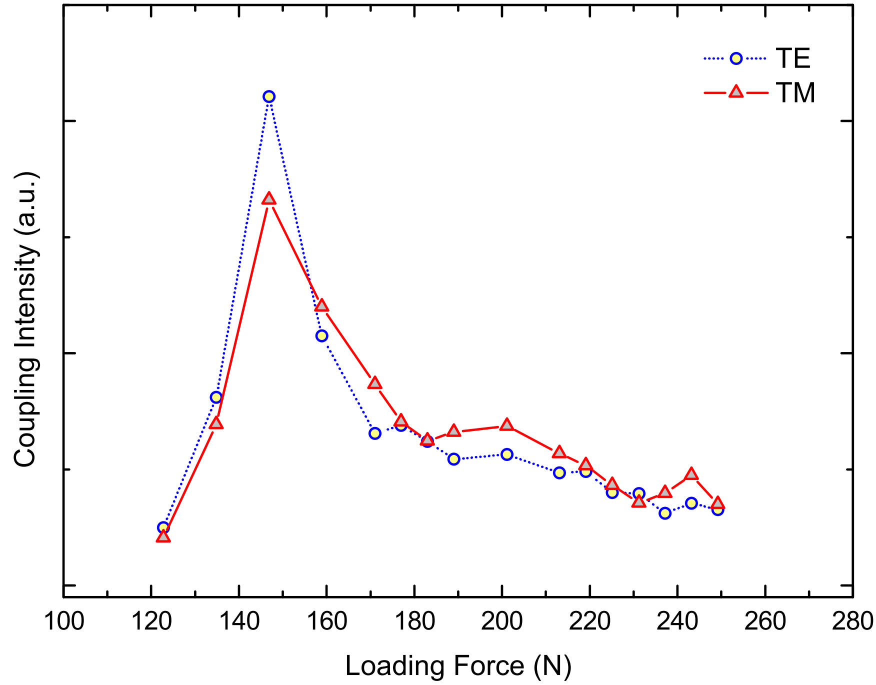

Figure 4.10: Light coupling efficiency vs. loaded force for both TE and TM polarizations as observed for PS films.

Considering that the polymer films form a slab waveguide with SiO_2 as the lower cladding and air acting as the upper cladding, the number of modes for both TE and TM polarizations were calculated, by solving the Maxwell's equations with the corresponding boundary conditions [53]. Finally, the number of modes was also confirmed with the calculations of the mode spectrum using beam propagation simulations. The number of modes calculated in this manner was in agreement with the number of modes observed in the measurements. In Fig. 4.11, the vertical line represents the out–coupled mode spectrum excited for m = 0, 1 and 2 modes for TE polarization and m = 0 and 1 modes for TM polarizations. Two guided modes have been excited with TM polarization at $\alpha = -2.475°$ & –3.825° angles, while three modes have been obtained in TE spectrum at $\alpha =$ –2.490°, –3.885° and –5.230°.

Starting from the angles of TE and TM (Fig. 4.11) guided modes, both the refractive index and thickness of our waveguide polymer films were computed.

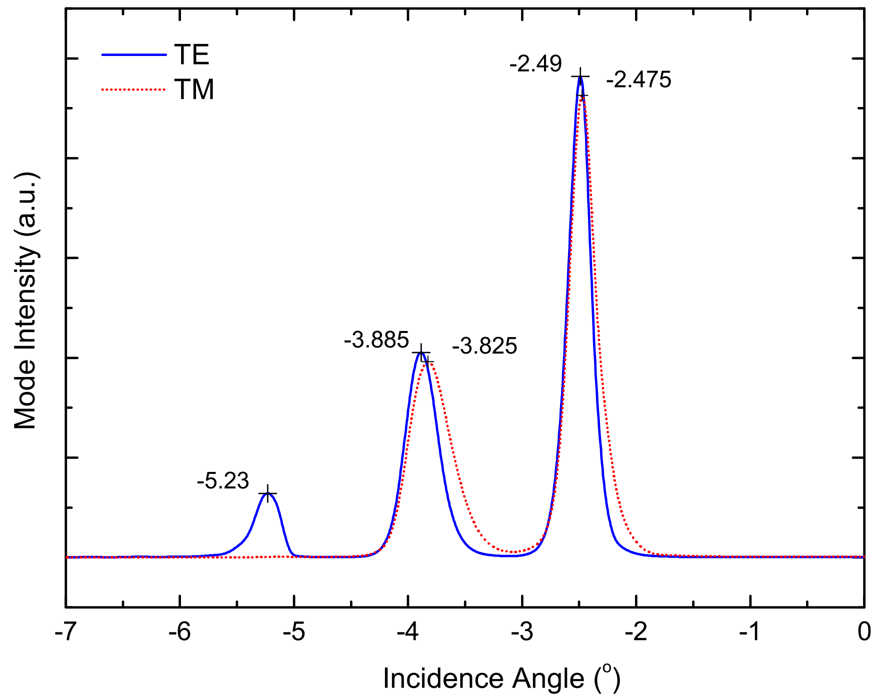

Figure 4.11: Typical spectrum of guided modes with TM (or TE) polarized light for PMMA.

Due to the softness of the polymer films, a reduction in polymer film thickness may be expected as the applied stress is increased, as indeed observed experimentally. A change in refractive index is also observed which is shown in Fig. 4.12 as a function of the reduction in thickness of the polymer film for PMMA samples. Applied stress causes a steady decrease of film thickness resulting in a reduction displacement of up to 0.06 μm. The value of the refractive index extrapolated to zero applied stress is found to be 1.4869. As the refractive index of bulk PMMA is given to be between 1.48 and 1.49 [76], the value we obtained is in very good agreement with the literature. At higher stress values represented with the film thickness displacement in Fig. 4.12, refractive index increases at a rate of 0.0133 μm^{-1} in the elastic region for both TE and TM polarizations.

A nonzero value of $\Delta n = n_{TE} - n_{TM}$ indicates that the material is birefringent and hence anisotropic. Birefringence gives the level of optical anisotropy in the

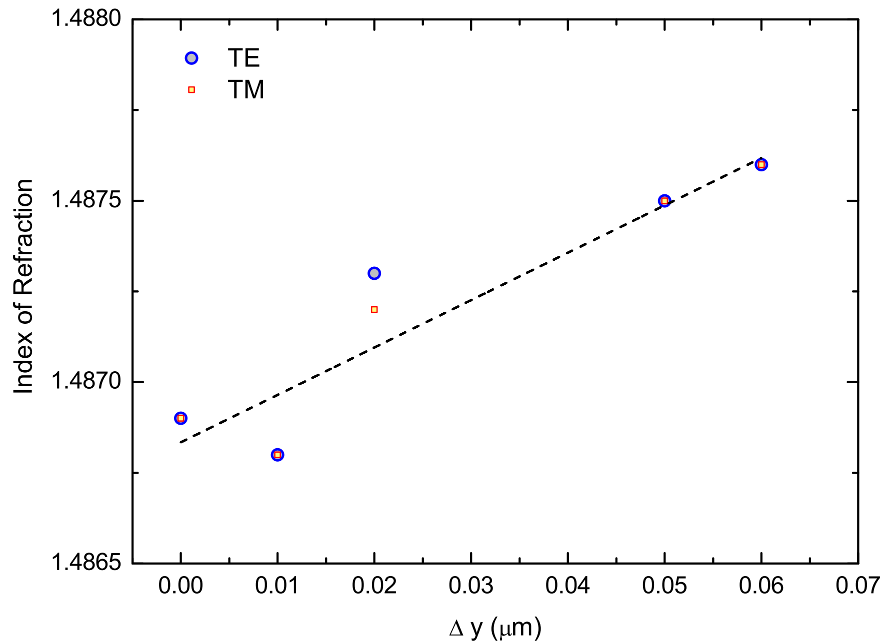

Figure 4.12: Calculated refractive index values vs. thickness change of PMMA films. A small but steady increase of the refractive index is clearly observed for both polarizations.

film that is the difference in refractive index between orthogonal planes of polarization. Thus, birefringence may be an indication of the molecular orientation. The data in Fig. 4.13 reflect the birefringence of PMMA.

Birefringence of PMMA slab waveguides was found to be zero. This result is supported in the literature [76]. Additionally, negative birefringence was observed for PS and positive birefringence for BCB slab waveguides with values of Δn = – 0.0008 and Δn = + 0.0022 at unstressed condition (Δy = 0 μm), respectively. The birefringence results indicate that for BCB and PS films the polymer molecules are preferentially oriented in and out of the film plane, respectively [66]. An increase of the applied pressure on the prism, accompanied by the film thickness reduction (Δy), results in enhancement of the negative birefringence of PS and decrease of the positive birefringence of BCB films. Both can be attributed to the greater increase of n_{TM} compared to n_{TE} as the stress is increased in the out–of–plane direction for both PS and BCB layers. Table 4.4 summarizes the

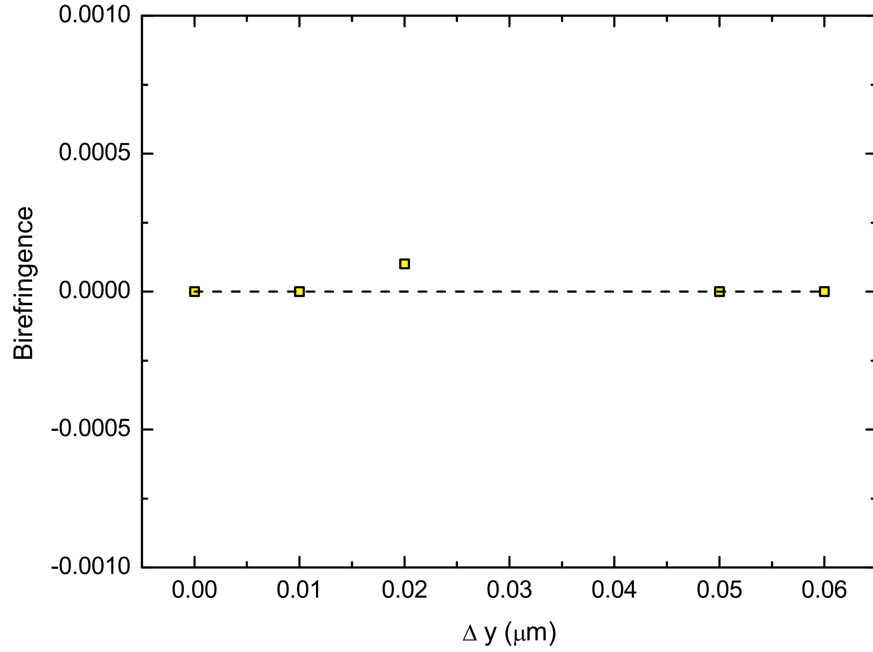

Figure 4.13: Birefringence vs. thickness change of PMMA polymer films.

results of optical properties of PMMA, PS and BCB polymer thin films.

As a result, we have measured the effective index and thickness of spin–coated polymers on silicon substrate by using well known prism coupling technique. It has become clear during our measurements that symmetric trapezoid prisms are better suited to couple light into the polymer thin film instead of right angle prisms. Applied stress results in the elastic reduction of the polymer thin film thickness as well as an increase in the refractive index. Measurements of the

Table 4.4: Summary of all refractive index and thickness measurements for polymer films in this study.

	Δy = 0 μm				Δy = Δy$_{max}$			
	n_{0TE}	n_{0TM}	t_0(μm)	n_{0TE}–n_{0TM}	n_{TE}	n_{TM}	t(μm)	n_{TE}–n_{TM}
PMMA	1.4869	1.4869	2.30	0	1.4876	1.4876	2.24	0
PS	1.5844	1.5852	2.37	–0.0008	1.5857	1.5874	2.21	–0.0017
BCB	1.5575	1.5553	2.38	+0.0022	1.5586	1.5570	2.31	+0.0016

refractive index for both TE and TM polarizations for PMMA, BCB and PS thin films all show that refractive index increases with applied stress. We have shown for the first time that, in contrast with PMMA thin films which showed no birefringence at any applied stress levels used in this study, PS and BCB both showed increasing birefringence as a function of applied stress, the former of negative sign and the latter of positive sign. We have shown that prism coupling method is a useful technique to measure opto–mechanical properties of thin polymer films, with proper choice of the coupling prism [74].

4.7 A New Approach: Elasto–Optical Properties of Small Young–Moduli Films By Prism Coupling Method

Based on the results and findings reported in Section 4.6.2, a new approach is proposed here for elasto–optic characterization of thin polymer films, making use of the well known prism coupling technique [48]. This method allows us, to determine the optical anisotropy and out–of–plane mechanical properties and to correlate both in order to obtain the elasto-optical properties of thin polymer films, for the first time [77].

4.7.1 Current State of the Problem - Literature Review

For optical waveguide devices, deposited onto substrates, the mechanical properties of thin polymer films may differ by several orders of magnitude from those of bulk materials [60]. Furthermore, it is known that the stresses generated in the films cause the polymer chains to orient in the plane of the film resulting in anisotropic optical properties. Therefore, it is important to be able to measure mechanical and optical properties of thin polymer films simultaneously.

There are a number of recent studies that have analyzed polymeric films showing in–plane and out–of–plane optical anisotropy (birefringence) [66,78]. In addition, there are also studies investigating the mechanical properties of thin polymer films, most of which are limited only to the in–plane direction. This is due to the difficulty of measuring small thickness changes of thin films in the out–of–plane direction [79]. The refractive index measurements of thin films ($t < 10$ μm) are usually done by making use of ellipsometry or prism coupling methods, the latter is preferred due to the higher accuracy and capability to measure birefringence. For the out–of–plane mechanical properties, on the other hand, there are several methods that have been reported recently. Kumer *et al.* measured the out–of–plane modulus by Brillouin scattering technique, but the method is limited to minimum film thickness of 100 μm [80]. Another method is the parallel plate capacitor method, where metal layers are deposited onto polymer surfaces, which could modify the mechanical properties of the film [81]. Other approaches include use of nanoindentor [82], atomic force microscopy [83], and precision capacitance dilatometry [67]. While all of these methods measure the out–of–plane mechanical properties of the polymer films, they do not measure optical properties simultaneously. Therefore, the relation between the stress and the optical properties can only be established indirectly for thin polymer films. While much of the above mentioned shortcomings may be overcome with the use of prism coupling technique, the effect of applied stress on the measured quantity during the use of prisms to couple light into the film have not, so far, been taken into account.

As discussed in the previous section, the decrease of the air layer thickness and thus of the coupling efficiency is a function of the mechanical properties of the film under investigation. In our case, the Young's moduli of the polymers are few orders of magnitude smaller than that of the ordinary glassy dielectric materials, which makes them softer [84]. Therefore, it is reasonable to assume that the reduction of the air gap thickness with applied pressure is small in the range of the thickness variations of the polymer films used in this study.

The out–of–plane elastic moduli of the thin polymer films were deduced by using the same prism coupling setup. The thickness change was used together

with the applied stress information in order to obtain the corresponding stress–strain curves. Use of finite element calculations was made to establish connection between measured values and elasto–mechanic properties, such as the Young's modulus. Since the polymers under investigation are viscoelastic, both plastic and elastic deformations may be expected to occur during the loading process. Therefore, all measurements of out–of–plane modulus and refractive index were performed during the unloading process [67].

4.7.2 Index of Refraction and Birefringence

In order to be able to mutually compare the stress effects on the guiding films, the polymer layer thicknesses were adjusted to be nearly identical. Film thicknesses had values of 2.37 μm for PS, 2.38 μm for BCB, and 2.30 μm for PMMA layers, as verified by both stylus profilometer and prism coupling methods, being in good agreement. These thicknesses were chosen so that there are at least two guided modes in the waveguides. The mode calculations were done by solving the Maxwell's equations with the corresponding boundary conditions [53]. The number of modes calculated in this manner was further confirmed by calculating the mode spectrum of the same slab waveguides using beam propagation techniques employing finite difference methods. The calculations predicted four modes (both TE and TM) for the BCB, four modes for PS and three modes for PMMA slab waveguides. The predictions were in agreement with the observed number of modes.

The results of refractive index variation versus the thickness change with the applied pressure for PS films are given in Fig. 4.14. A steady increase of the refractive index is clearly observed for both polarizations. The out–of–plane refractive index (n_{TM}) increased from a value of 1.5852 up to a value of 1.5874 as the film thickness decreased by 0.15 μm with the applied pressure. Similarly, the in–plane refractive index (n_{TE}) increased from 1.5844 to 1.5856 in the same range. At higher applied stresses, there is a flat region, where the in–plane refractive index does not increase with the applied stress. This may be attributed to the saturation of the alignment of molecules contributing to refractive index as well

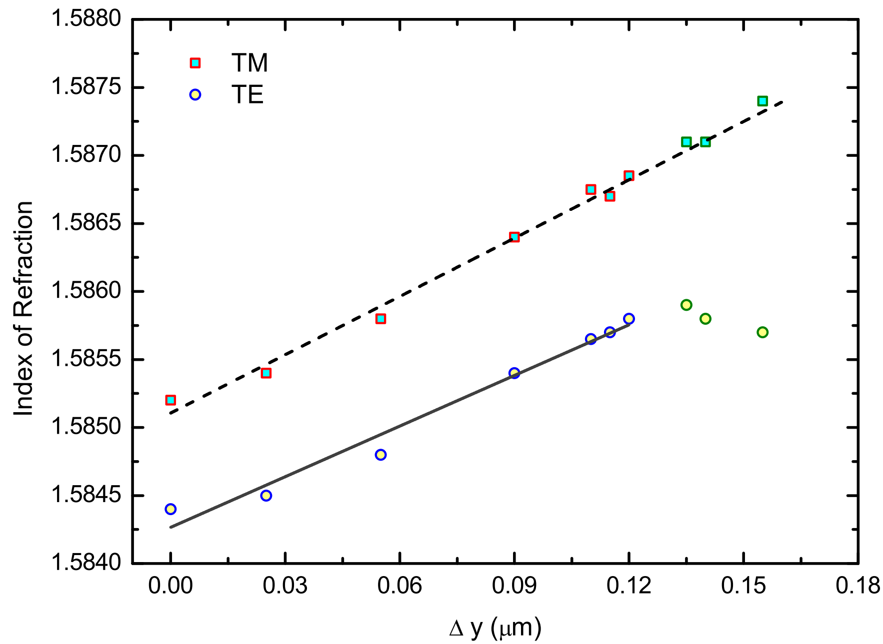

Figure 4.14: Change of the TE and TM refractive index for PS films with change in the film thickness.

as the saturation of the density variation of dipoles contributing to index of the polymer in the in–plane direction. On the other hand, the density of the polymer continues to increase with the applied pressure leading to an increase in the refractive index for the out–of–plane direction. The flat region was not taken into account in the calculations of the elasto–optical constants, to be discussed below.

Similar trends for refractive index increase were observed for both BCB and PMMA layers. Fig. 4.15 shows the results obtained for BCB films. An increase for both polarizations is observed with the decrease of the film thickness as pressure is applied on the polymer layer. The value of n_{TE} increased from 1.5575 up to a value of 1.5586 as the thickness of the guiding film was reduced by about 0.07 μm with the applied pressure, while n_{TM} has increased from 1.5553 to 1.5566 in the same range. As for the PMMA layers, the refractive index was measured to increase from about 1.4869 to 1.4876 for the both polarizations.

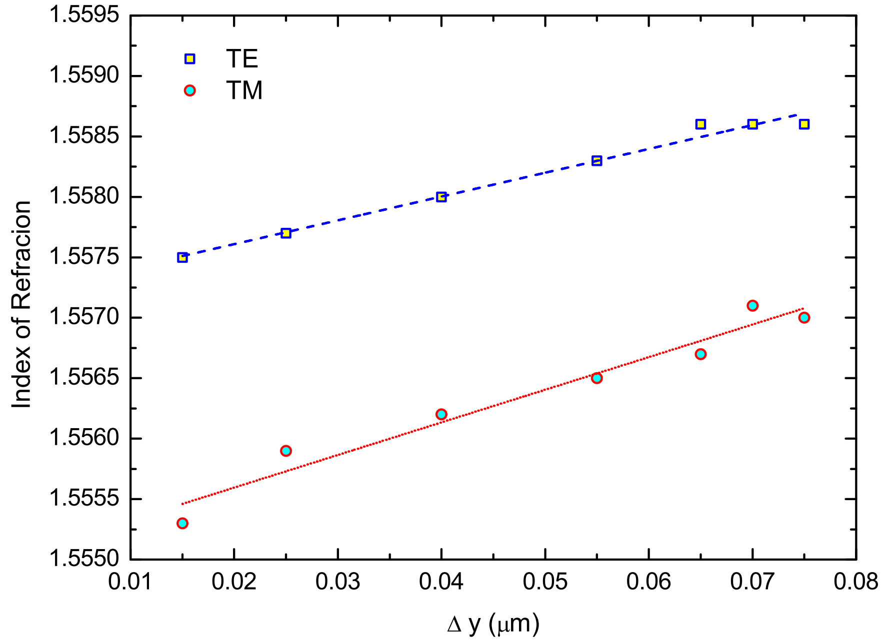

Figure 4.15: Change of the TE and TM refractive index for BCB films with change in the film thickness.

Another interesting outcome of the refractive index measurements is the evolution of birefringence ($\Delta n = n_{TE} - n_{TM}$) with the applied pressure. The birefringence for the PS films was measured to be negative (see Fig. 4.16) with an initial value of about –0.0007 which increased slightly in the negative direction up to a value of about –0.0011, as the film thickness decreased by 0.12 μm, with applied pressure. BCB layers have also been measured to be birefringent, however with a positive sign. For these layers, the value of the birefringence was initially about 0.0022, which decreased slightly down to 0.0017 with the film thickness decrease of 0.07 μm, as a result of the applied pressure [77]. On the other hand, the PMMA films have been found to be optically isotropic. Zero birefringence was observed in the unstressed condition and there was no change in the birefringence as the pressure was increased (see Fig. 4.13), although both n_{TE} and n_{TM} showed small increases with applied pressure.

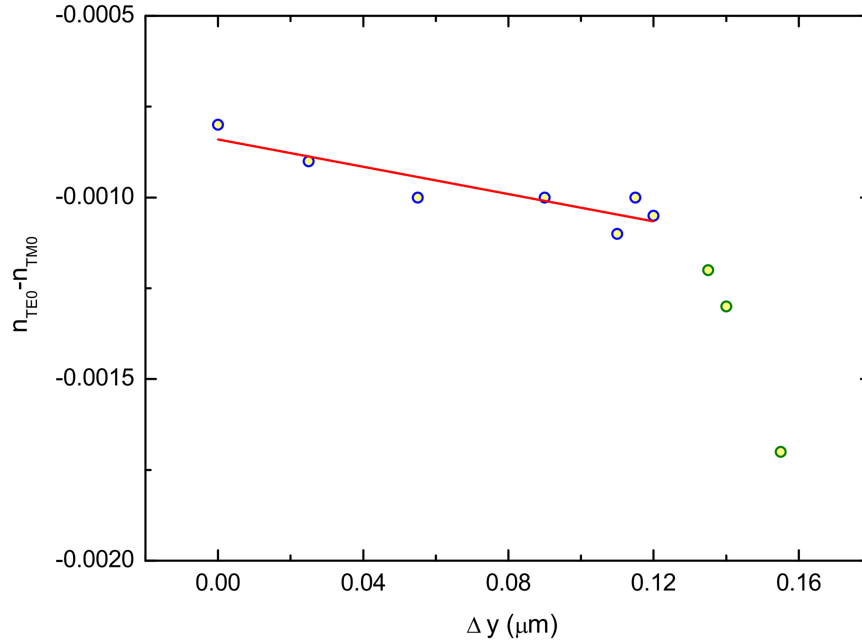

Figure 4.16: Change of birefringence for PS films with change in the film thickness.

The refractive index values determined from these measurements are in agreement with those reported in the literature. The refractive indices of $n_{TE} = 1.587 \pm 0.002$ and $n_{TM} = 1.582 \pm 0.002$ were previously reported for the atactic PS films having negative birefringence that are in good agreement with our results [85]. For the BCB films, to the best of our knowledge, the number of polarization dependent refractive index values reported is very limited. For BCB type similar to ours the only measurement was reported by Tanikella *et al.*, where it was reported that $n_{TE} = 1.55$ with a positive birefringence of $\Delta n = 0.002$ [86]. These values are also in a very good agreement with ours. As for the PMMA layers, they are known to be optically isotropic, and White *et al.* reported a refractive index of 1.488, identical with our measurements [87]. However, in all of these reports no mention of stress induced changes in the quantities measured were made. Finally, the measurements that we report for PS, BCB, and PMMA [77] have higher precision from those reported in literature.

4.7.3 Out–of–Plane Mechanical Properties by Prism Coupling Method

The out–of–plane elastic moduli for the polymer films were calculated by using the applied stress and film thickness measurements. In calculation of the applied stress the area considered was the coupling area having size of 8 mm $\times$ $\sim$1 mm at the base of the coupling prism. The size of the coupling area was measured by inspecting the dark region formed at the base of the prism. For this purpose the prism coupling setup has been modified so as to incorporate a load cell (see Fig. 4.17). The load cell was Sensotec Model 13 (AL322BN) subminiature compression only load cell allowing measurement of loads of up to 50 lbs. The value of the force was measured by a means of the load cell and ranged approximately between 0 and 150 N. The coupling pressure was adjusted by a micrometer in contact with a calibrated spring system.

The values obtained for out–of–plane elastic moduli were $0.3 \pm 0.1 \times 10^9$ N/m^2, $0.3 \pm 0.1 \times 10^9$ N/m^2, and $0.9 \pm 0.1 \times 10^9$ N/m^2 for PS, BCB and PMMA thin films, respectively. The elastic moduli obtained for the investigated three polymer layers are approximately one order of magnitude smaller than those reported in the literature for their bulk counterparts. For PS films, the

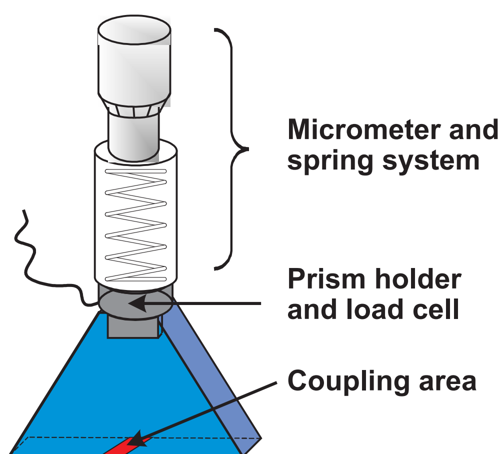

Figure 4.17: Detailed representation of the system used for pressure application and readout in the modified prism coupler setup.

corresponding value is reported to be about 2–3 $\times$ 10^9 N/m^2 [71,88]. Most of the films studied in the literature were bulk PS specimens with typical dimensions of the order of millimeters. The moduli were measured under tensile stress in stretching condition corresponding to an in plane modulus. Thus, we can expect these values to differ from our thin film results in the out–of–plane direction. For PMMA layers, the reported Young's moduli are approximately 3.2 $\times$ 10^9 N/m^2 [61, 88], again measured for bulk material under the in-plane stretching condition. As for the BCB films, there are several studies reporting on the out–of–plane modulus of thin BCB films ($\sim$15 μm) with value of 3 $\times$ 10^9 N/m^2 [81,89]. In these reports the authors made use of parallel plate capacitor method, where metal layers are deposited onto polymer surfaces, which may result in modification of the mechanical properties of the film itself.

Although there are studies that report moduli of thin films close to their bulk counterparts, a number of studies were also done analyzing the thickness dependence of the out–of–plane mechanical properties of thin polymer films. They report clear differences between thin film and bulk polymers. For example, Liou *et al.* measured out–of–plane elastic properties for thin polyimide films as a function of thickness using precision capacitance dilatometer [67,90]. They have found that the out–of–plane elastic moduli of the thin polymer films decrease with decreasing film thickness. For polyimide films, Liou *et al.* obtained one order of magnitude decrease from about 2.8 $\times$ 10^9 N/m^2 down to 0.3 $\times$ 10^9 N/m^2 in the out–of–plane modulus as the film thickness decreased from $\sim$15 μm to $\sim$4 μm and verified that the in–plane modulus has a larger value.

A similar behavior of modulus anisotropy and decrease of the out–of–plane modulus with decreasing thickness can be expected for the polymer films studied in this work. This possibility was tested by performing out–of–plane modulus measurements for PMMA films of various thicknesses. In this series PMMA was dissolved in chlorobenzol and was spincoated at 2000–5000 rpm in order to obtain varying thickness films, which were not obtainable by using chloroform as solvent. Five PMMA films with thicknesses of 3.10, 3.22, 4.30, 4.75 and 6.10 μm were obtained. The values of out–of–plane moduli for these films were obtained as described above.

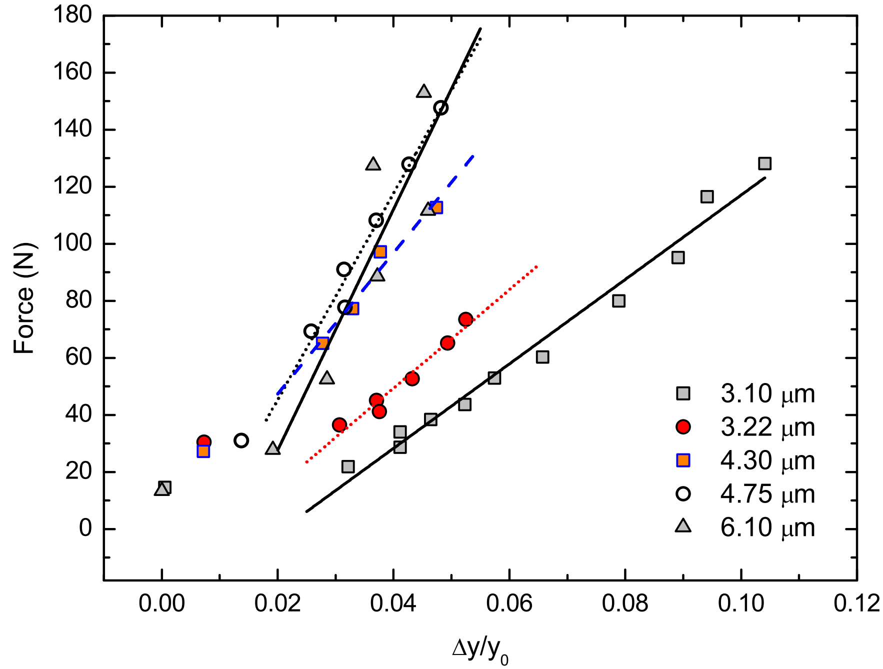

Figure 4.18: Experimental data for variation of $\Delta y/y_0$ with the applied force F for PMMA films with thicknesses of 3.10, 3.22, 4.30, 4.75, and 6.10 μm. Note that the coupling is completed for F $>$ 15 N.

Figure 4.18 shows the experimental data for variation of $\Delta y/y_0$ with the applied force (F). As is observed, the slopes of the graph increase with increasing film thickness. For all the polymer films a minimum force of about 15 N is required to obtain strain larger than zero, i.e. to obtain coupling between the prism and polymer film. Thus the variation of $\Delta y/y_0$ with the applied force can only be observed for applied force of about 15 N or greater. As the value of strain increases the variation becomes linear due to the stabilization of the coupling area between the prism and the film and this is the region which was used to determine the out–of–plane elastic moduli of the layers.

The slopes are directly proportional to the out–of–plane moduli of the films and therefore our expected trend has been verified. The calculated out–of–plane moduli variation with film thickness for PMMA layers are depicted in Fig. 4.19. The geometry and coordinate axis convention is illustrated in the inset of the

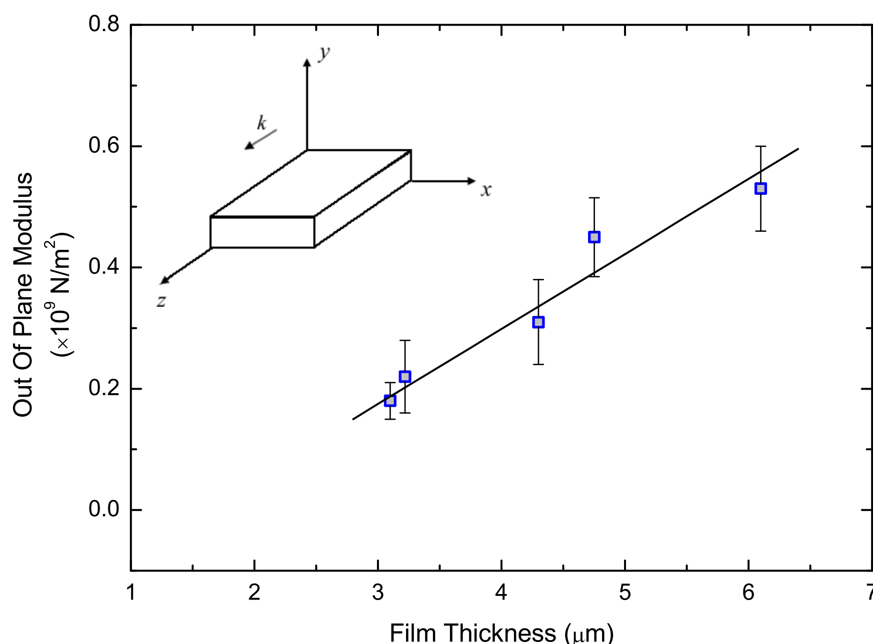

Figure 4.19: Variation of the out–of–plane elastic modulus with films thickness for PMMA films.

figure. It is evident form the figure that the out–of–plane moduli of the layers show a steady increase with increasing film thickness. Namely, the modulus showed an increase from $0.18 \pm 0.03 \times 10^9$ N/m^2 up to $0.5 \pm 0.1 \times 10^9$ N/m^2 with increase in thickness from 3.10 μm to 6.10 μm. Therefore, the analysis of the change of the out–of–plane elastic modulus with change in film thickness has two important results. First, as was expected, the moduli increase with increasing film thickness. If the increase is assumed to be linear, the moduli are expected to reach their bulk value at a thickness of about 27 μm. The second finding that should be mentioned is the effect of the solvent used in preparation of the films. It was found that the PMMA films produced using chloroform as solvent resulted in larger out–of–plane elastic moduli compared to the ones prepared using chlorobenzol.

4.7.4 Elasto–Optical Properties

The stress dependence of the refractive index is expressed in terms of the Fresnel's index ellipsoid and the Cauchy's stress ellipsoid. In the elastic range of the material and when the ellipsoids are coaxial, the principal refractive indices are related to the principle stresses by the Neumann–Maxwell stress equations:

$$n_i = n_0 + C_1\sigma_i + C_2\left(\sigma_j + \sigma_k\right), \tag{4.20}$$

where n_i are the principal refractive indices, σ_i are principal stresses and C_1, C_2 are the elasto–optic coefficients [70, 91]. The difference $(C_1 - C_2) = C$ is the usually reported and widely used value for the stress–optic coefficient of a material when a measurement of the birefringence is made under uniaxial stress conditions [71, 92].

The bulk counterpart of the polymer films investigated in this study are known to be isotropic. In the thin film form, on the other hand, these polymers were found to be slightly anisotropic. The observed anisotropy is mainly due to effects such as in-plane orientation of the polymeric chains during the spinning process and solvent evaporation and may depend on the specific type of polymer itself [67, 74]. Due to the spinning process, the expected anisotropy of the layers is of uniaxial type and one of the principal axis of symmetry is parallel to the incident polarization. The measured birefringence in this case is less than 0.002 and in this regime the isotropic assumption for mode equations remains as a reasonable approximation [93, 94]. The variation of birefringence under stress, on the other hand (i.e. stress induced birefringence), is governed by Neumann–Maxwell stress equations. Therefore, in our case, we assume that the polymer films are isotropic in the in–plane direction and with the described coordinate system convention the following stress equations can be written as [70, 91]

$$n_x = n_{0x} + C_1\sigma_x + C_2(\sigma_y + \sigma_z), \tag{4.21}$$

$$n_y = n_{0y} + C_1\sigma_y + C_2(\sigma_x + \sigma_z) \tag{4.22}$$

In order to be able to obtain the elasto-optic coefficients, the variation of the refractive index and film stress should be expressed in terms of identical quantities. For this reason 3D finite element method (FEM) analysis was used so as to

obtain the principal stresses for each polymer system. The material properties were defined by their elastic moduli (E), Poisson's ratio (ν), and initial thickness (y_0). The out–of–plane elastic moduli and film thicknesses were determined experimentally as described above, while the values of Poisson's ratio for each film were used as reported in the literature. In particular, the following values of were employed: 0.33, 034, and 0.35 for PS, BCB, and PMMA, respectively [81,84,95]. The change of the film thickness (Δy) with applied stress was simulated and equations of the following form were obtained for each direction and polymer film:

$$\sigma_i = constant \times \Delta y = K_i \times \Delta y \tag{4.23}$$

Moreover, the refractive index variations with the applied pressure can also be expressed in terms of Δy. As seen from Figs. 4.12, 4.14, and 4.15 the following linear relations can be written:

$$n_x = n_{0x} + m_x \Delta y, \tag{4.24}$$

$$n_y = n_{0y} + m_y \Delta y, \tag{4.25}$$

where m_x and m_y are the slopes obtained from the linear fits to the refractive index measurements. Substituting Eqs. (4.23)–(4.25) into Eqs. (4.21) and (4.22) and taking their difference the equations for the elasto–optic coefficients C_1 and C_2 take on the form

$$C_1 = \frac{(m_x + m_y)(K_2 - K_1) - (m_x - m_y)(K_1 + K_2 + 2K_3)}{(K_1 + K_2)(K_2 - K_1) - (K_1 - K_2)(K_1 + K_2 + 2K_3)}, \tag{4.26}$$

$$C_2 = \frac{(m_x - m_y) - C_1(K_1 - K_2)}{K_2 - K_1} \tag{4.27}$$

Here, the elasto–optic coefficients C_1 and C_2 are expressed in terms of quantities determined from refractive index measurements (i.e. m_x and m_y) and the parameters found from FEM calculations (i.e. K_1, K_2, and K_3).

The results of FEM analysis and elasto–optic coefficient calculations are given in Table 4.5. The table contains the initial thickness of the guiding polymer films (y_0), maximum films thickness change with the applied pressure (y_{max}), calculated elastic moduli of the layers (E), constants (K_1, K_2, and K_3) determined by FEM

simulations as explained above, the slope values (m_x and m_y) given in Eqs. (4.24) and (4.24), and the calculated elasto–optic constants C_1, C_2 and C.

For PS thin films, the elasto–optical coefficients C_1 and C_2 were calculated to be -48 ± 3 Br and -29 ± 3 Br ($1Br = 10^{-12}$ m^2/N), respectively. To the best of our knowledge, there are no reported values of C_1 and C_2 for the any of the polymers studied here. Instead, there are strain elasto–optical coefficients (p_{11}, p_{12}) reported only for PS films [96]. These coefficients can be translated into the stress–optical coefficients by using the following relations [54]:

$$C_1 = -\frac{n^3}{2E}(p_{11} - 2\nu p_{12}), \quad (4.28)$$

$$C_2 = -\frac{n^3}{2E}(p_{12} - \nu p_{11} - \nu p_{12}) \quad (4.29)$$

Table 4.5: Results of FEM analysis and elasto-optic coefficient calculations. The tabulated data includes the initial thickness of the guiding polymer films (y_0), maximum film thickness change with the applied pressure (Δy_{max}), calculated elastic moduli of the layers (E), constants (K_1, K_2, and K_3) as determined by FEM simulations, the slope values (m_x and m_y), and the calculated elasto-optic constants C_1, C_2 and C.

Polymer	y_0	Δy_{max}	E	(10^{14} N/m^2)			(10^4 1/m)		(10^{-12} m^2/N)		
	(μm)	(μm)	(10^9 N/m^2)	K_1	K_2	K_3	m_x	m_y	C_1	C_2	C
PS	2.37	0.16	0.3	-0.9	-1.9	-0.9	1.241	1.428	-48	-29	-19
BCB	2.38	0.07	0.3	-1.0	-1.9	-1.0	1.969	2.698	-107	-30	-77
PMMA	2.30	0.06	0.9	-3.4	-6.3	-3.4	1.306	1.306	-10	-10	0

Using the reported p_{11}, p_{12}, E and ν values for bulk PS films in the above equations, we obtain $C_1 = -61.4$ Br and $C_2 = -69.7$ Br. First, we see that the values for the bulk material and those we obtained for thin PS films are of the same order. The difference of $(C_1 - C_2)$ can be used to compare our results with the widely reported stress–optic coefficient, C, for bulk polymers where measurement of birefringence is made under uniaxial stress conditions [71,92]. For bulk PS, C is positive with a value of 8.3 Br, whereas the calculated C for PS thin films is negative with a value of -19 Br. The bulk material value is in agreement with the value of $8-10$ Br in other reports in the literature [70,71,88]. The process of determination of the stress–optic constant (C) is the key factor in the apparent sign mismatch of the mentioned parameter. Namely, the reported stress–optical coefficients (C) for bulk PS materials are calculated from the birefringence and stress measurements when the material is under tensile stress. The extent of motion of the polymer chains is limited upon such deformation. It is known that the birefringence of PS is mainly determined by the orientation of the phenyl groups. As discussed by Rudd and Gurnee [88], upon the application of tensile stress, the phenyl groups tend to align in the direction of the applied stress, i.e. in the in–plane direction. This results in positive birefringence and positive stress–optic coefficient. However, in our case the stress is applied in the out–of–plane direction of the polymer film. We suggest that this should lead to at least partial alignment of the polymer chains in the out–of–plane direction and consequently to perpendicular alignment of the plane of the phenyl groups [68]. This, accordingly, should result in negative birefringence and negative stress–optic coefficient, as was observed for the PS films in this study.

The elasto-optic coefficients for the BCB layers were found to be as $C_1 = -107 \pm 8$ Br, $C_2 = -30 \pm 8$ Br, and $C = -77$ Br. To our knowledge, these are the first reported elasto–optic coefficient values for the BCB polymer films. As for the PMMA thin film layers, the obtained stress optic coefficients are $C_1 = -10 \pm 3$ Br, $C_2 = -10 \pm 3$ Br, and $C = 0$ Br. The results for PMMA are reasonable since for optically isotropic films equal elasto–optical coefficients and thus zero C are to be expected.

While the reported method for measuring the mechanical and optical properties simultaneously by making use of prism coupling technique is novel and interesting, we note that the measured values of the material properties such as out–of–plane elastic modulus and elasto–optical constants should be considered as preliminary. The technique still involves difficulties and assumptions that can possibly be improved. Namely, we have assumed that the applied stress is uniform across the coupling area and the Poisson's ratio (ν) was assumed to be identical with the bulk value.

In conclusion, results of 3D FEM analysis together with the refractive index measurements were applied to the Neumann–Maxwell stress equations in order to obtain the elasto-optic coefficients for the PS, PMMA, and BCB thin films. To the best of our knowledge, these values are the first reported results for thin film polymers. In contrast with the measurements of elasto–optic coefficients made under tensile stress conditions for bulk polymers, it was found that the applied stress in the out–of–plane direction of the thin films investigated leads to negative elasto–optic coefficients, as observed for all of the three thin polymer films.

Chapter 5

Germanosilicate Dielectrics III: Nonlinear Properties

This part of the thesis is devoted to non–linear properties of germanosilicate glasses. After a brief introduction to basic principles of nonlinear optics relevant to our study, the results obtained in literature for poled silica based dielectrics are summarized. We conclude with a study on the optimization of the second order nonlinearity $\left(\chi^{(2)}\right)$ in germanosilicates, upon which the largest nonlinearity coefficient was reported [97].

5.1 Nonlinear Optics in Brief

In general, when we discuss optics a linear behavior is presumed, i.e. we assume that the propagation of an electromagnetic wave through a medium is governed by a linear wave equation [98]. This in turn implies several assumptions such as: a light beam in a medium can be described sufficiently by its wavelength and velocity (n), the principle of superposition holds, light can not interact with light, the frequency of the light is not affected by the medium, etc. After the invention of laser in 1960, the notion of nonlinear optics has been introduced. Linear optics was not sufficient to describe the observed effects. As a result, it was extended so

as to account for observations such as: the intensity of lights affects the speed of light in a medium, i.e. refractive index, violation of the principle of superposition, control of light with light, etc.

Both linear and nonlinear phenomena are properties of the medium itself and are not exhibited in free space. Therefore, this opens a route for us to possibly enhance the nonlinearity in materials, e.g. germanosilicate glasses.

In general, an electric field $\big(\mathbf{E}(\mathrm{t})\big)$ applied to a medium induces a dipole moment within it. The dipole moment per unit volume, polarization $\big(\mathbf{P}(\mathrm{t})\big)$, can be expressed as a function of the electric field as follows [99]:

$$\mathbf{P}(t) = \epsilon_0 \Big[\underbrace{\left(1 + \boldsymbol{\chi}^{(1)}\right) \mathbf{E}(t)}_{\text{linear}} + \underbrace{\boldsymbol{\chi}^{(2)}\mathbf{E}^2(t) + \boldsymbol{\chi}^{(3)}\mathbf{E}^3(t) + \cdots + \boldsymbol{\chi}^{(n)}\mathbf{E}^n(t)}_{\text{nonlinear}} \Big], \qquad (5.1)$$

where in the frequency domain the polarization is related to the electric field by $\boldsymbol{\chi}^{(n)}$, being a $(n+1)^{\mathrm{th}}$ rank susceptibility tensor. For more insight, another notation could be [100]

$$\begin{aligned} P_i = \epsilon_0 \big[(1 + \sum_j \chi^{(1)}_{ij} E_j) \quad + \quad & \sum_j \sum_k \chi^{(2)}_{ijk} E_j E_k + \\ & \sum_j \sum_k \sum_l \chi^{(3)}_{ijkl} E_j E_k E_l + \cdots \big] \end{aligned} \qquad (5.2)$$

That is, the tensor product in Eq. (5.1) of the interacting electric fields at $\omega_1, \omega_2, \ldots, \omega_n$ and $\boldsymbol{\chi}^{(n)}(-\omega; \omega_1, \omega_2, \ldots, \omega_n)$ gives the nth order nonlinear polarization response at frequency ω of the medium, $\mathbf{P}^{(n)}_{\omega}(t)$, in other words

$$\mathbf{P}^{(n)}_{\omega}(t) = \boldsymbol{\chi}^{(n)}(-\omega; \omega_1, \omega_2, \ldots, \omega_n) \Big| \mathbf{E}_{\omega_1}(t) \cdots \mathbf{E}_{\omega_n}(t) \qquad (5.3)$$

The typical order of magnitudes of the susceptibilities are as follows: $\chi^{(1)} \sim 1,\ \chi^{(2)} \sim 10^{-12}\ m/V, and\ \chi^{(3)} \sim 10^{-21}\ m^2/V^2$. The higher order susceptibilities are even smaller and the most studied ones are the second and third order nonlinearities $\chi^{(2)}$ and $\chi^{(3)}$.

5.1.1 Second Order Nonlinearities

Among the most studied $\chi^{(2)}$ phenomena are the linear electro-optic effect and second harmonic generation (SHG). Note that the second-order term in Eq. (5.1)

makes no contribution to polarization in an isotropic material having a center of symmetry (centrosymmetric) [58]. In such a material, a change in radial coordinates, e.g. r to −r, leaves the crystal's atomic arrangement unchanged which responds in the same way to a physical influence. That is, if we have

$$P^{(2)} = \epsilon_0 \chi^{(2)} (+E)^2 \text{ and } -P^{(2)} = \epsilon_0 \chi^{(2)} (-E)^2 \tag{5.4}$$

the equality $P^{(2)} = -P^{(2)}$ is only possible if $P^{(2)} = 0$.

5.1.1.1 Second Harmonic Generation

Qualitatively, the second harmonic generation can be described as follows. The polarization effects of a material are mainly due to the outer valence electrons of the atoms of the medium since the inner ones are tightly bound. The intra-atomic field is at the order of 10 V/nm or 10^{10} V/m [101]. When the driving electrical field is weaker than that, the response of the material is linear. The response becomes increasingly nonlinear when comparable field is in play, so as to drive the electrons beyond the quadratic minimum of the interatomic potential. At this point, the polarized dipoles radiate at frequency 2ω, which in turn generates an electric field $\mathbf{E}_{2\omega}$. Informally, one can understand this with the following mathematical arguments [58]: If one of the Fourier components of the applied electric field is of the form

$$E = E_0 \cos(\omega t), \tag{5.5}$$

then the polarization response would be

$$P^{(2)} = \epsilon_0 \chi^{(2)} E_0^2 \cos^2(\omega t) = \epsilon_0 \chi^{(2)} E_0^2 \times \left[\frac{1}{2}(1 + \cos 2\omega t) \right] \tag{5.6}$$

thus

$$P^{(2)} = \frac{1}{2} \epsilon_0 \chi^{(2)} E_0^2 + \frac{1}{2} \epsilon_0 \chi^{(2)} E_0^2 \cos 2\omega t, \tag{5.7}$$

where the first component represents a constant DC rectification and the second one is a field at frequency 2ω.

Returning to the formal discussion and assuming that in a bulk nonlinear material the fundamental (ω) and second harmonic (2ω) fields are infinite plane

waves, a monochromatic electric field $\mathbf{E}$(t) can be written as

$$\mathbf{E}(t) = \frac{1}{2}\left(\mathbf{E}_\omega e^{j\omega t} + \mathbf{E}_{-\omega} e^{-j\omega t}\right) \quad \text{and} \tag{5.8}$$

$$\mathbf{E}_\omega = \hat{\mathbf{E}}_\omega e^{j\mathbf{k}_\omega \cdot \mathbf{r}}, \tag{5.9}$$

where $\mathbf{E}_\omega$ is a complex field amplitude and $\mathbf{k}_\omega$ is the propagation vector whose magnitude is given by $k_\omega = \omega n_\omega / c$, n_ω being the refractive index of the medium at frequency ω. Similarly, the related nonlinear polarization can be expressed as:

$$\mathbf{P}^{(n)}(t) = \frac{1}{2}\left(\mathbf{P}_\omega^{(n)} e^{j\omega t} + \mathbf{P}_{-\omega}^{(n)} e^{-j\omega t}\right). \tag{5.10}$$

The electric field behavior in this case is governed by the nonlinear wave equation that includes $\mathbf{P}_\omega^{(2)}$ as the source term [99]:

$$\boldsymbol{\nabla}^2 \mathbf{E}_\omega - \frac{\epsilon}{c^2}\frac{\partial^2 \mathbf{E}_\omega}{\partial t^2} = \mu_0 \frac{\partial^2 \mathbf{P}_\omega^{(2)}}{\partial t^2}, \tag{5.11}$$

where $c = 1/\sqrt{\mu_0 \epsilon_0}$ is the speed of light, ϵ is the dielectric permittivity and μ_0 is the permeability.

In the case of SHG it is useful to define a second harmonic nonlinear coefficient tensor [102]

$$\mathbf{d} = \frac{1}{2}\boldsymbol{\chi}^{(2)}(-2\omega; \omega, \omega) \tag{5.12}$$

and for a given symmetry of the material and electric field polarization, the electric field and nonlinear polarization are characterized by a scalar quantity, the effective nonlinear coefficient d_{eff}. In the case of a nonlinear slab of thickness L, for example, with a step profile of nonlinearity with d_{eff} from z=0 to L the solution of Eq. (5.11) can be written as [99]

$$\hat{E}_{2\omega}(z) = \frac{j\omega}{n_{2\omega} c} \hat{E}_\omega^2(0) d_{eff} z \,\text{sinc}\left(\frac{\Delta k z}{2}\right), \tag{5.13}$$

where when the phase-matching term Δk is non-zero a periodic conversion between the fundamental and second harmonic field occurs as a function of distance L, with a quadratic dependence on the fundamental field amplitude $\hat{E}_\omega$. The second harmonic intensity is given by:

$$I_{2\omega} = \frac{1}{2} n_{2\omega} \epsilon_0 c \left|\hat{E}_{2\omega}\right|^2. \tag{5.14}$$

Among the most common techniques to measure the nonlinear susceptibilities is the *Maker fringe* method [103, 104]. In this technique, the nonlinear susceptibility is determined by relative measurement of the peak amplitudes of the signal generated by the nonlinear material and a previously measured standard. The incidence angle between the surface normal and beam direction is measured (θ_ω). As the slab is rotated, the variation of the effective path length varies and the sinc^2 argument in Eqs. (5.13) and (5.14) results in several maxima and minima [99]. The sinc^2 argument takes the form:

$$\frac{\Delta k\ z(\theta_\omega)}{2} = \frac{4\pi}{\lambda}\frac{(n_\omega - n_{2\omega})L}{2\cos\theta_\omega}, \tag{5.15}$$

where $\Delta k = \lambda(n_\omega - n_{2\omega})$. Thus, the measurement of Maker fringes results in determination of d_{eff} for the investigated material.

5.1.1.2 Electro-Optic Effect

The electro-optic effect can be described as the change in the refractive index of the material under an applied electric field. It comprises the linear Pockel's effect and the quadratic Kerr effect. For an electro-optic refractive index change to occur, a presence of a large electric field at lower frequency than the optical field (e.g. DC) is necessary. Therefore, there is no need for a high-intensity optical field for observation of this second order phenomenon. Based on this fact, its theory was developed much earlier [105] than the invention of laser and therefore it is usually described by an electro-optic tensor **r**, rather than the nonlinear susceptibility $\boldsymbol{\chi}^{(2)}\ (-\omega;\omega,0)$.

In general, the dielectric tensor $\boldsymbol{\epsilon}$ and the refractive indices n_{ij} are related by

$$n_{ij}^2 = \epsilon_{ij} = 1 + \chi_{ij}^{(1)}(-\omega;\omega) \tag{5.16}$$

and for example for a non-centrosymmetric uniaxial crystal the dielectric tensor becomes

$$\boldsymbol{\epsilon} = \begin{bmatrix} n_o^2 & 0 & 0 \\ 0 & n_o^2 & 0 \\ 0 & 0 & n_e^2 \end{bmatrix}, \tag{5.17}$$

where n_o and n_e are the ordinary and extraordinary refractive indices. Traditionally, the electro-optic coefficient r_{ijk} is defined as:

$$\Delta\left(\frac{1}{n_{ij}^2}\right) = r_{ijk}E_k \tag{5.18}$$

and for $\Delta n \ll n$

$$\Delta n_{ij} \cong \frac{1}{2}n_{ij}^3 r_{ijk}E_k \ . \tag{5.19}$$

In the formalism of nonlinear optical theory [102] the general expression for nonlinear polarization is given by:

$$\mathbf{P}_{\omega_\sigma}^n = \epsilon_0 K(-\omega_\sigma;\omega_1,\ldots,\omega_n)\sum_{\alpha_1,\ldots,\alpha_n}\chi_{\mu\alpha_1\ldots\alpha_n}^{(n)}(-\omega_\sigma;\omega_1,\ldots,\omega_n)(E_{\omega_1})_{\alpha_1}\cdots(E_{\omega_n})_{\alpha_n}, \tag{5.20}$$

where summation is carried over the repeated indices and the numerical factor K is defined to be:

$$K(-\omega_\sigma;\omega_1,\ldots,\omega_n) = 2^{\ l+m-n}p. \tag{5.21}$$

Here, n is the order of nonlinearity, m is the number of present DC fields, $l = 1$ for $\omega_\sigma \neq 0$, otherwise $l = 0$, and p is the number of distinct frequency permutations [99]. For example, for SHG K=1/2, for DC Kerr effect K=3, and for linear electro-optic effect K=2. For the linear electro-optic (Pockel's) effect the second order nonlinear polarization is given by:

$$\mathbf{P}_\omega^{(2)} = 2\epsilon_0\boldsymbol{\chi}^{(2)}(\omega;\omega,0)\mathbf{E}_\omega\mathbf{E}_{DC}. \tag{5.22}$$

The displacement field $\mathbf{D}$ becomes

$$\mathbf{D}_\omega = \epsilon_0\mathbf{E}_\omega + \sum_{n=1}^{\infty}\mathbf{P}_\omega^{(n)} = \epsilon_0\left[\boldsymbol{\epsilon} + 2\boldsymbol{\chi}^{(2)}(-\omega;\omega,0)\mathbf{E}_{DC}\right]\mathbf{E}_\omega. \tag{5.23}$$

If a small perturbation in $\boldsymbol{\epsilon}$ then we have:

$$(n_{ij} + \Delta n_{ij})^2 = \epsilon_{ij} + 2\chi_{ijk}^{(2)}(-\omega;\omega,0)E_{DC_k}, \tag{5.24}$$

where summation over indices ijk is assumed and the DC field is applied alon k direction. Expanding the left hand side to the first order in Δn we obtain [99]

$$\Delta n_{ij} = \frac{\chi_{ijk}^{(2)}(-\omega;\omega,0)E_{DC_k}}{n_{ij}}. \tag{5.25}$$

The relationship between the electro-optic coefficient (r_{ijk}) and the second order susceptibility is found by comparing the Eqs. (5.19) and (5.25) to be:

$$r_{ijk} = \frac{2\chi^{(2)}_{ijk}(-\omega;\omega,0)}{n^4_{ij}}. \tag{5.26}$$

For an example, if we consider a crystal of uniaxial symmetry $C_{\infty\nu}$ or symmetry classes of *6, 6mm, 4, 4mm* that have identical symmetry properties for r_{ijk} [106] (poled glass posses the same symmetry and will be used in the following sections) and making use of contracted notation[1] for indices, the electro-optic coefficient is expressed as:

$$r_{ij} = \begin{bmatrix} 0 & 0 & r_{13} \\ 0 & 0 & r_{13} \\ 0 & 0 & r_{33} \\ 0 & r_{13} & 0 \\ r_{13} & 0 & 0 \\ 0 & 0 & 0 \end{bmatrix}. \tag{5.27}$$

Finally, as an electromagnetic wave of wavelength λ passes through an electro-optic material of length L the phase retardation is given by:

$$\Delta\phi = \frac{2\pi}{\lambda}\Delta n L = \frac{\pi}{\lambda}n^3 r E L = \frac{\pi}{\lambda}n^3\frac{V}{d}L\ . \tag{5.28}$$

5.1.2 Third Order Nonlinearity: Kerr Effect

Since we are interested in nonlinear properties of poled germanosilicate dielectrics in this section we will limit ourselves with discussion of the Kerr effect. The $\chi^{(3)}$ susceptibility gives rise to third order nonlinearity even in centrosymmetric materials. Among these nonlinearities we are especially interested in the electric field induced second harmonic generation (EFISH) and the DC Kerr effect (quadratic electro-optic effect), that are assumed to be the driving source of second harmonic generation and electro-optic modulation in nonlinear silica [107].

[1]Here r_{ijk} is symmetric in the last two indices. The assumption is valid for Kleinman's symmetry [106], i.e. $r_{ijk} \rightarrow r_{il}$, *l:jk* $\Rightarrow 1 \equiv 11,\ 2 \equiv 22,\ 3 \equiv 33,\ 4 \equiv 23,\ 5 \equiv 13,\ 6 \equiv 12$.

Similar to the derivation of Eq. (5.25) the refractive index change due to the third order nonlinearity can be shown to be

$$\Delta n_{\parallel} = \frac{3\chi^{(3)}_{1111} E_{DC} E_m}{n_o}, \quad (5.29)$$

$$\Delta n_{\perp} = \frac{3\chi^{(3)}_{1122} E_{DC} E_m}{n_o}, \quad (5.30)$$

where $\Delta n_{\parallel}$ and $\Delta n_{\perp}$ are the refractive index change experienced by the optical filed in parallel and perpendicular polarization to the applied DC electric field (E_{DC}), respectively[2] [99, 106].

5.2 Nonlinearity in Thermally Poled Germanosilicate Thin Films

In this section we report the poling process and measurements of the nonlinearity profile of thermally poled low-loss germanosilicate films deposited on fused-silica substrates by PECVD, of interest as potential electro-optic devices. The study was done in a close collaboration with A. Özcan, M.J.F. Digonnet and G.S. Kino, a group in Stanford University, working on poling and measurement of the nonlinearity profile in silica dielectrics [108]. Most of the poling process of the samples and the nonlinearity profile determination were done at Stanford University.

Poled glasses have been studied actively over the last few years because of the prospect of using these nonlinear materials for integrated electro-optic phase and amplitude modulators or parametric oscillators [112]. Poled silica-based glasses are particularly interesting in these applications because they exhibit low loss, broad transmission bands, and high optical damage threshold, and they are compatible with the current fiber technology. One of the main limitations of this material, however, is that its nonlinear coefficient is low, with a peak second-order optical nonlinear coefficient d_{33} of only ∼0.8 pm/V [113] (compared to ∼30 pm/V for $LiNbO_3$). Therefore, all poled-glass devices reported to date require

[2] The applied DC electric field is of the form $\mathbf{E}_0 = (E_{DC} + E_m \cos\omega_m t)\hat{\mathbf{z}}$.

high voltages and/or long lengths [114–116]. Increasing the nonlinearity of poled glasses, for example by improving the material composition or the poling conditions, is therefore an important step towards achieving practical poled-glass devices.

In the following sections, we report a poling study of germanosilicate films that makes significant progress in this direction. This choice of material has been made primarily for two reasons. First, since their propagation loss has been dramatically reduced in our previous study [27], germanosilicate films grown onto fused silica substrates are excellent waveguides with a refractive index close to that of silica, which makes them compatible with fiber-optic technology. Second, the addition of *Ge* to silica increases the refractive index of the glass, and thus its third-order optical susceptibility $\chi^{(3)}$, and since the nonlinear coefficient d_{33} of poled glass is proportional to $\chi^{(3)}$ it is expected that d_{33} will also be increased. Poled germanosilicate glass [116–118] is therefore a promising candidate for low-loss as-deposited integrated planar electro-optic devices. In this work, we have used thermal poling instead of UV poling because the later produces short-lived nonlinear regions [118]. We confirm these expectations with experimental investigations showing that the peak nonlinear coefficient of germanosilicate films with optimal Ge concentration, thickness, and poling time take a record value of ∼1.6 pm/V [97].

5.2.1 Second Order Nonlinearity in Poled Glasses

Since glasses are known to posses macroscopic inversion symmetry they do not normally exhibit second order nonlinearity. However, in 1991 Myers *et al.* [107] reported that thermal poling can be a simple and reproducible way to induce second order nonlinearity in glass. In this method, the sample is heated upto ∼300 ℃ and a high voltage (∼5 kV) is applied across the sample, generating a large electrostatic field inside the glass ($\sim 10^3$ V/μm). According to the charge separation model [107, 109], a permanent built-in electric field is frozen near the anode surface with a thickness of few micrometers, which occur due to migration of charges within the material [110]. This built-in field interacting with the third

order nonlinearity ($\boldsymbol{\chi}^{(3)}$) induces an effective second order non-linearity, expressed as:

$$\boldsymbol{\chi}^{(2)} \sim \boldsymbol{\chi}^{(3)} E_{dc}, \tag{5.31}$$

where E_{dc} in this case is the built-in electric field. More specifically, for the two processes of interest the relations are as follows: for the electric field induced second harmonic generation

$$\boldsymbol{\chi}^{(2)}(-2\omega;\omega,\omega) = 3\boldsymbol{\chi}^{(3)}(-2\omega;\omega,\omega,0)E_{dc}, \tag{5.32}$$

and for the electro-optic effect:

$$\boldsymbol{\chi}^{(2)}(-\omega;\omega,0) = 3\boldsymbol{\chi}^{(3)}(-\omega;\omega,0,0)E_{dc}^2, \tag{5.33}$$

known as DC Kerr effect. At this point it is useful to give the form of the nonlinear coefficient tensor **d**, (see Eq. (5.12)) for poled glass materials that have uniaxial symmetry $C_{\infty\nu}$ or symmetry classes of *6, 6mm, 4, 4mm.* The nonlinearity in this case is given by [106, 111]:

$$P^{(2)} = \begin{bmatrix} 0 & 0 & 0 & 0 & d_{31} & 0 \\ 0 & 0 & 0 & d_{31} & 0 & 0 \\ d_{31} & d_{31} & d_{33} & 0 & 0 & 0 \end{bmatrix} \begin{pmatrix} E_1^2 \\ E_2^2 \\ E_3^2 \\ 2E_2E_3 \\ 2E_1E_3 \\ 2E_1E_2 \end{pmatrix}, \tag{5.34}$$

where

$$d_{31} = \frac{1}{3}\, d_{33}. \tag{5.35}$$

5.2.2 Germanosilicate Growth Process

The germanosilicate films were deposited on square substrates of synthetic silica (Infrasil) 25 mm on the side and 150 μm thick using plasma-enhanced chemical vapor deposition (PECVD) in a parallel-plate reactor (Plasmalab 8510C). The films were grown at 350 ℃ and at a pressure of 1 Torr, with an RF power of 10 W at 13.56 MHz. The diameter of the plates was 24 cm. The precursor gases were silane (2% SiH_4/N_2), germane (2% GeH_4/He), and nitrous oxide (N_2O). The flow rates of silane and nitrous oxide were kept constant at 180 and 225 sccm, respectively, while that of germane was set at a constant value between 0 and 90 sccm that was varied from run to run. The growth rate of the films was ∼40 nm/min. A major problem in the application of CVD-grown silicon-based layers in integrated optics is the incorporation of hydrogen in the form of N−H bonds into the film matrix [13]. Annealing is usually required to reduce the propagation loss of the optical waveguides that utilize these layers as the core. Instead, the samples were manufactured using a new recipe that has produced the lowest propagation loss of as-grown germanosilicate films reported to date [27].

In order to study the effects of film composition, film thickness, and poling time on the nonlinearity profile and strength of poled germanosilicate films, seven germanosilicate films at four different germane flow rates (0, 33, 50, and 90 sccm) were grown. The characteristics of these films and the poling times are listed in Table 5.1. Mole fraction of GeO_2 of the grown films is estimated from the

Table 5.1: Characteristics and poling time of germanosilicate films poled in air at ∼5 kV and ∼280 ℃.

Sample #	Germane flow rate	Mole fraction of GeO_2 (%)	Refractive index @ 1550 nm	Film thickness	Poling time	Peak d_{33} (pm/V)
1	0 sccm	0	1.45	4 μm	10 min	0.54
2	33 sccm	∼20	1.475	4 μm	5 min	0.80
3	33 sccm	∼20	1.475	4 μm	10 min	1.59
4	33 sccm	∼20	1.475	4 μm	15 min	1.00
5	33 sccm	∼20	1.475	2 μm	10 min	1.02
6	50 sccm	∼30	1.504	4 μm	10 min	0.78
7	90 sccm	∼56	1.546	4 μm	10 min	0.81

measured dispersion curves of the films [119], as listed in Table 5.1. Based on previous measurements on similar samples [27], the propagation loss of the as-grown waveguides was estimated to be less than 0.5 dB/cm at 1550 nm.

5.2.3 Thermal Poling and Characterization of the Poled Germanosilicate Films

As-grown germanosilicate/Infrasil structures were thermally poled [107] using polished n-type silicon electrodes in air at ∼5 kV and 280 ℃, with the positive electrode facing the film. The experimental apparatus used for poling is depicted in Figure 5.1. After the sample is heated up to the desired temperature the voltage is applied across the sample. The poling process in general lasts for 5 to 15 minutes. Next, the heater is turned off and the setup cools down do room temperature in approximately half an hour. During the cooling process the voltage is still applied to the sample. After the process is over, the sample is removed for testing.

The nonlinearity spatial profile of each poled sample was measured using the

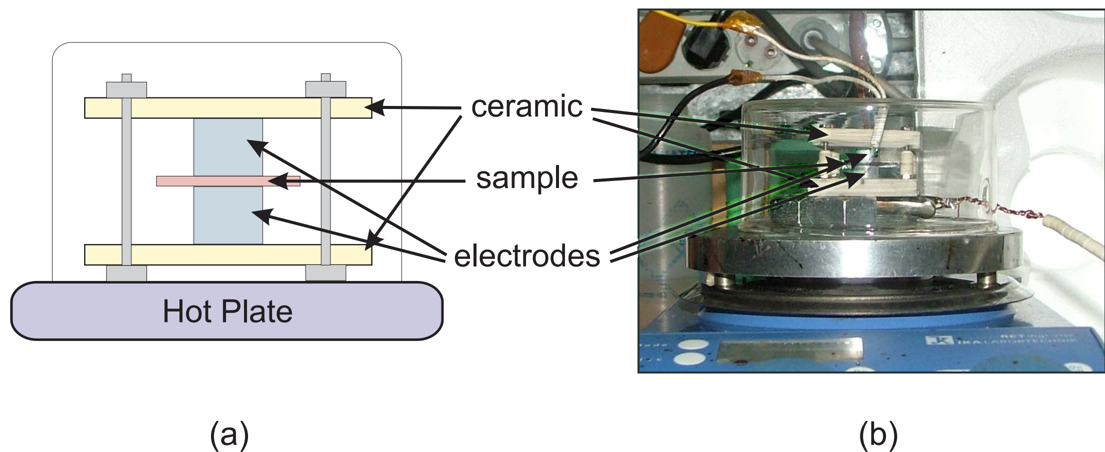

Figure 5.1: Thermal poling apparatus consisting of a hot plate and a pyrex beaker oven. The contact between the substrate and electrodes is maintained by a ceramic clamp.

Maker fringe-Fienup technique [120]. A fundamental laser beam at 1064 nm is launched onto the sample and the power in the second-harmonic (SH) signal (at 532 nm) generated within the nonlinear region is measured as a function of the angle of incidence of the fundamental laser beam, using the cylinder-assisted set-up described in Ref. [121]. The resulting curve is known as the Maker fringe (MF) curve [122]. Because of the refractive index mismatch between the Infrasil substrate and the germanosilicate film, angle-dependent spurious reflections occur at the film-cylinder and the film-substrate interfaces. Correction factors were thus applied to the measured MF curves to correct them for multiple reflections [123] and Fresnel reflection at both the fundamental and SH signal wavelengths. Furthermore, the sample grown at a 90 sccm germane flow rate, which physically looked brown, had higher loss, especially in the visible spectrum. The film's measured loss coefficients were thus used to correct the measured MF curve for this poled sample. Each of these corrected MF curves was finally processed using the iterative Fienup algorithm [124] to uniquely recover the second-order optical nonlinearity profile of each poled sample, as described in Ref. [120].

To identify the optimum poling time for these samples, we first poled samples #2, #3, and #4, all of which were grown at 33 sccm germane flow rate to a thickness of 4 μm, for 5, 10 and 15 minutes, respectively (see Table 5.1). The calibrated MF curves of these poled samples are shown in Figs. 5.2 (a)–(c). The nonlinearity depth profile of each sample recovered from these curves using the Fienup algorithm is shown in Fig. 5.3. All three profiles exhibit similar features, namely a sharp peak centered about 0.5 μm below the anode, followed by a weak pedestal that is approximately constant to a depth of $\sim 9-12$ μm and that gradually decreases to zero at a depth of $13-16$ μm. This sequence of profiles reveals that the optimum poling time for these germanosilicate/Infrasil structures at an applied E-field of $\sim$32.5 MV/m is 10 min. The peak d_{33} coefficient obtained under these poling conditions is as high as $\sim$1.6 pm/V. To our knowledge, this is the highest directly measured second-order nonlinear coefficient reported in thermally poled germanosilicate glass. This is about twice as high as the highest reliable peak d_{33} value reported for thermally poled fused silica, i.e., 0.8 pm/V [113]. The other measured peak d_{33} coefficients for poling times of 5 and 15 min

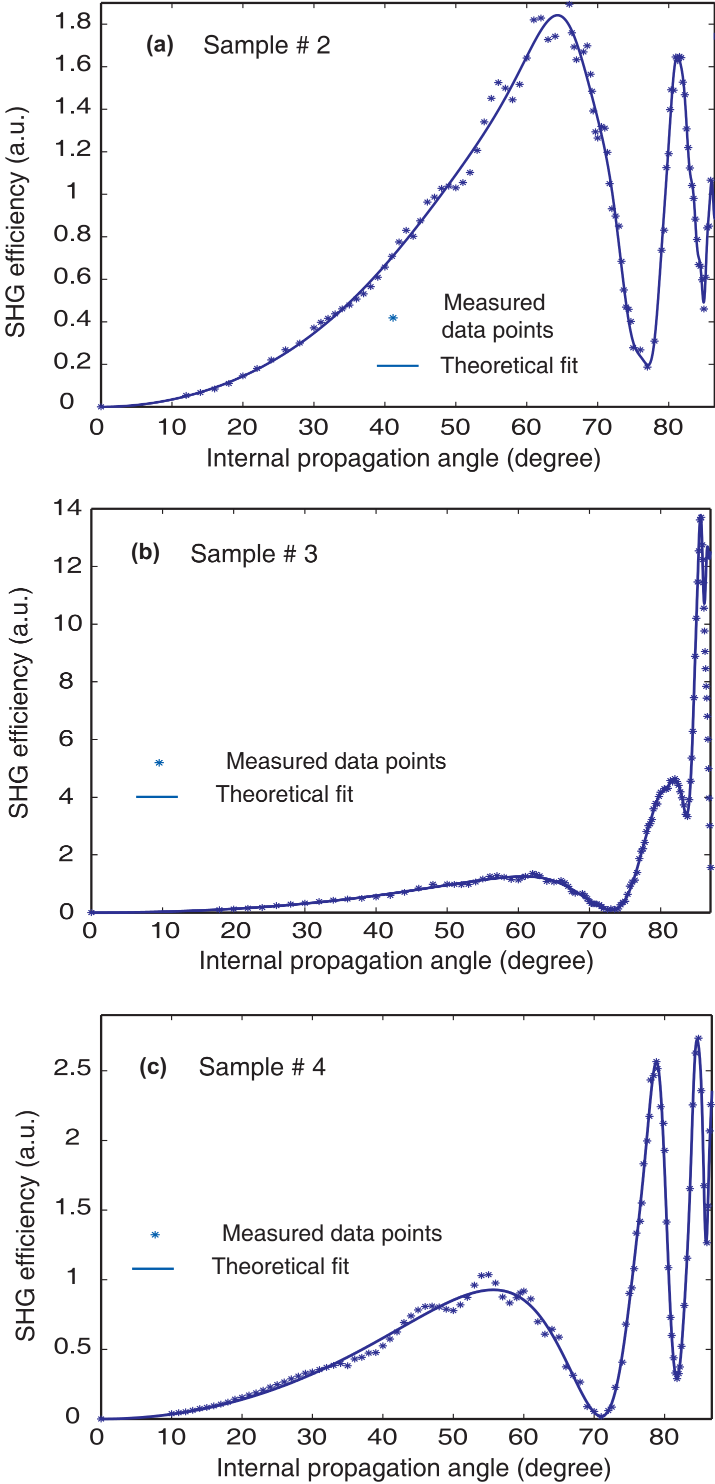

Figure 5.2: Calibrated MF curves measured for (a) sample #2, (b) sample #3, and (c) sample #4.

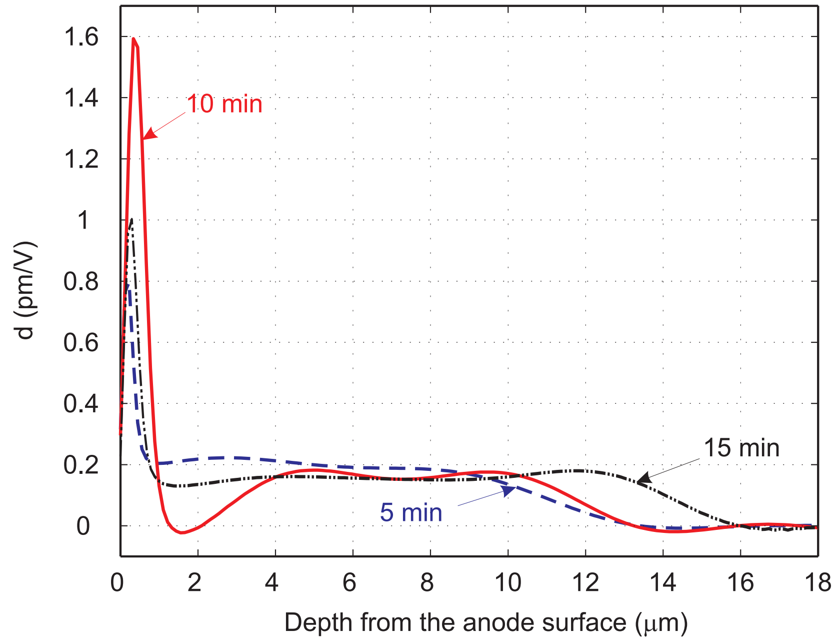

Figure 5.3: The recovered optical nonlinearity depth profiles of sample #2 (blue), #3 (red) and #4 (black).

are ~0.8 pm/V and ~1.0 pm/V, respectively. Note that the entire nonlinearity peak is contained in the germanosilicate film, while most of the pedestal is in the silica substrate. Furthermore, as physically expected, due to the diffusion of positive ions, the depth of the pedestal gradually increases from ~9 μm to ~12 μm as the poling time is increased from 5 min to 15 min (see Fig. 5.3).

It has been shown that most of the nonlinear coefficient of thermally poled silica arises from rectification of the third-order susceptibility $\chi^{(3)}$ of the material (see Section 5.2.1) by a DC electric field E that builds up in the material near the anode [117, 125, 126], i.e.:

$$d_{33} = \frac{3}{2}\,\chi^{(3)}\,E\ . \tag{5.36}$$

We postulate that same main mechanism is responsible for the nonlinearity of the present materials, and we attribute the observed increase in the peak d_{33} coefficient to the higher $\chi^{(3)}$ values in germanosilicate. To validate this point, we used an empirical relationship [127] to predict the nonlinear refractive index

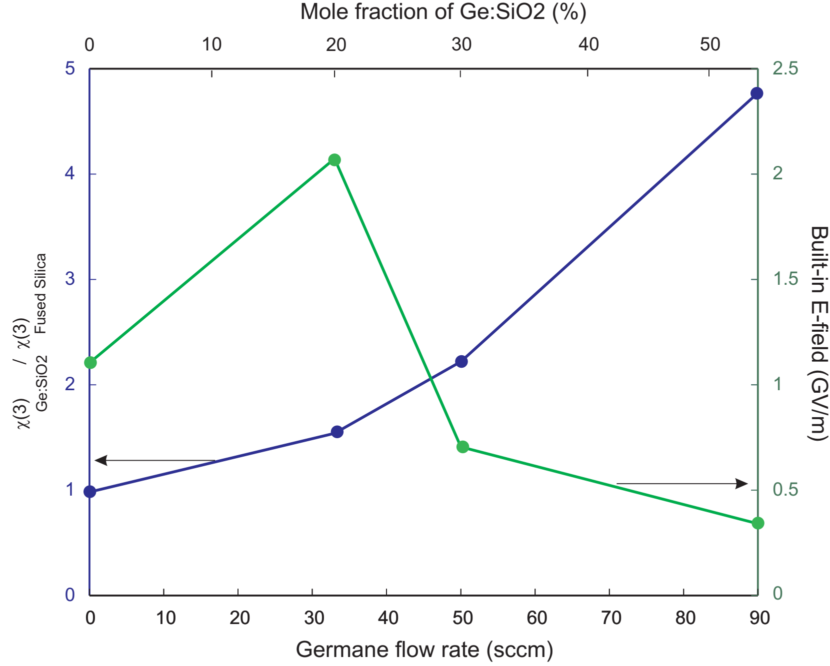

Figure 5.4: Left axis (blue curve): the ratio of the $\chi^{(3)}$ of the PECVD grown germanosilicate layer to the $\chi^{(3)}$ of fused silica; right axis (green curve): maximum built-in E-field measured in poled germanosilicate films.

of the germanosilicate films from their dispersion curves. The ratio of the third-order susceptibility of the PECVD grown layer, $\chi^{(3)}_{SiO_x:Ge}$, to the susceptibility of fused silica, $\chi^{(3)}_{Fused\ Silica}$, computed using the measured dispersion curves of the films grown at 0, 33, 50, and 90 sccm germane flow rates is plotted in Fig. 5.4 as a function of the germane flow rate. From the figure it is evident that as expected the $\chi^{(3)}$ of the 0–sccm germane flow rate film is very close to the $\chi^{(3)}$ of fused silica. Second, as the germane flow rate is increased, the $\chi^{(3)}$ of the germanosilicate film increases almost quadratically. Specifically, for sample #3 (flow rate of 33 sccm) $\chi^{(3)}_{SiO_x:Ge} \approx 1.54 \times \chi^{(3)}_{SiO_x}$. This enhancement factor contributes to $\sim 1.54/2 \approx 80\%$ of the two-fold increase observed in the peak d_{33} coefficient of sample #3. This suggests that the remaining contribution to the two-fold increase in peak d_{33} should be due to a 30% increase in the built-in field in sample #3 compared to the built-in field of poled fused silica [113].

The total depth of the induced nonlinear region ($\sim$13$-$16 μm) in Fig. 5.3 is

significantly narrower than for bulk Infrasil samples thermally poled under similar conditions, for which the depth is typically $\sim$40 μm [113, 121]. Furthermore, unlike in poled Infrasil samples, the $d_{33}(z)$ profile of the poled germanosilicate-Infrasil structures does not change sign. We believe that the reason for these differences is that the germanosilicate film limits the diffusion of positive ions such as H_3O^+ from the anode surface into the sample, which results in the formation of a narrower depletion region within the film itself. A similar blocking behavior in germanosilicate films, which also resulted in narrower nonlinear widths, has been previously reported [117].

Assuming that DC rectification of the third-order optical susceptibility of the glass is the main mechanism responsible for the observed nonlinearity, as is the case in silica [125,126,128], then the total voltage drop across the nonlinear region should be equal to the poling voltage [129]. To verify this point, we computed the integral along the depth z of each recovered nonlinearity profile of Fig. 5.3. The calculated voltages come out to be 4.77 kV, 4.77 kV and 5.21 kV for sample #2, #3 and #4, respectively. As expected, these values are close to the poling voltage ($\sim$5 kV), which lends further credence to the inferred profiles. We note that the true sign of all profiles in Fig. 5.3 cannot be inferred by using the Fienup algorithm alone. However, for almost all of the applications, this sign ambiguity, i.e., $\pm d_{33}(z)$, is not consequential. The fact that the integrated voltage drop across the recovered profiles has the same sign as the poling voltage (+5 kV) suggests that the inferred profiles as shown in Fig. 5.3 do have the correct sign (positive).

To provide further physical insight into the poling process for the germanosilicate-Infrasil structures, we calculated the charge density distribution frozen within the glass from the recovered nonlinearity profiles. Since the profile is proportional to the built-in E-field distribution, and since the distribution of space charge density in the glass is proportional to the derivative of the built-in E-field, the charge density can be obtained simply by taking the derivative of the measured profile. As an example, the charge density distribution of sample #4 (see Fig. 5.3) recovered by this process is shown in Fig. 5.5. This distribution

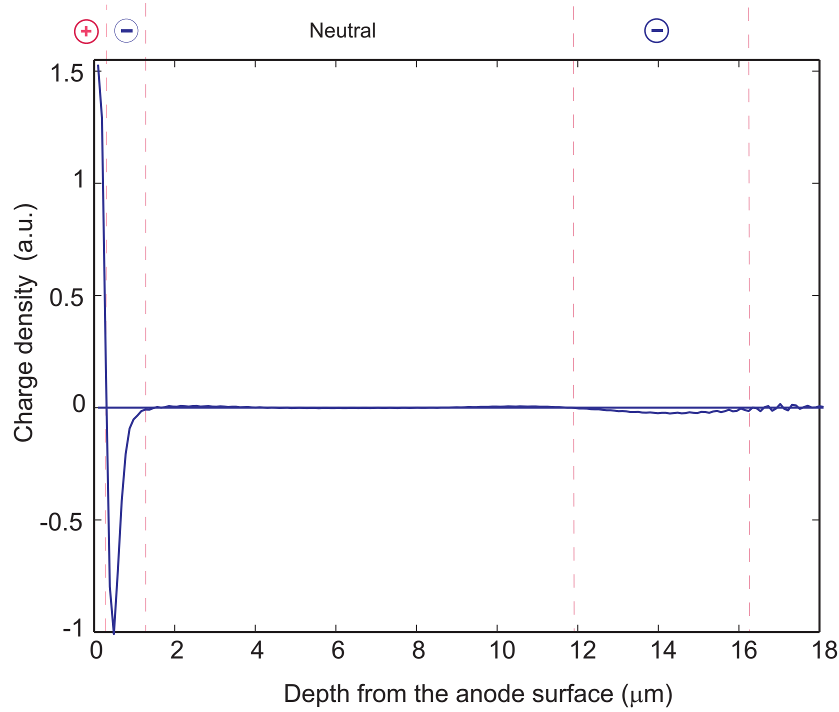

Figure 5.5: Charge density of poled sample #4, inferred by differentiating the recovered $d_{33}(z)$ profile.

exhibits a dipolar structure within the first micron below the anode surface, followed by a neutral region from $\sim$1 μm to $\sim$12 μm, which itself is followed by a weaker negatively charged region extending to a depth of $\sim$16 μm. The charge distributions recovered for the other samples show very similar features, the main difference being minor variations in the locations of these regions. The integral of the recovered charge distribution shown in Fig. 5.5 yields a total charge of -8.53×10^{-3} C/m^2. We believe that the neutrality of the sample is preserved by an equal amount of positive alkali ions (e.g. Na^+ or K^+) charge that is spread throughout the remaining bulk of the Infrasil substrate. Because it is spread over roughly 150 μm of glass, this charge density is much lower and thus contributes to a bulk second-order nonlinearity that is too weak to be measured. Furthermore, we anticipate that the depth of the neutral region shown in Fig. 5.5 reflects the total diffusion depth of the positive ions injected from the anode surface, which cancel out the negative sites left behind by the alkali ions such as Na^+ and K^+

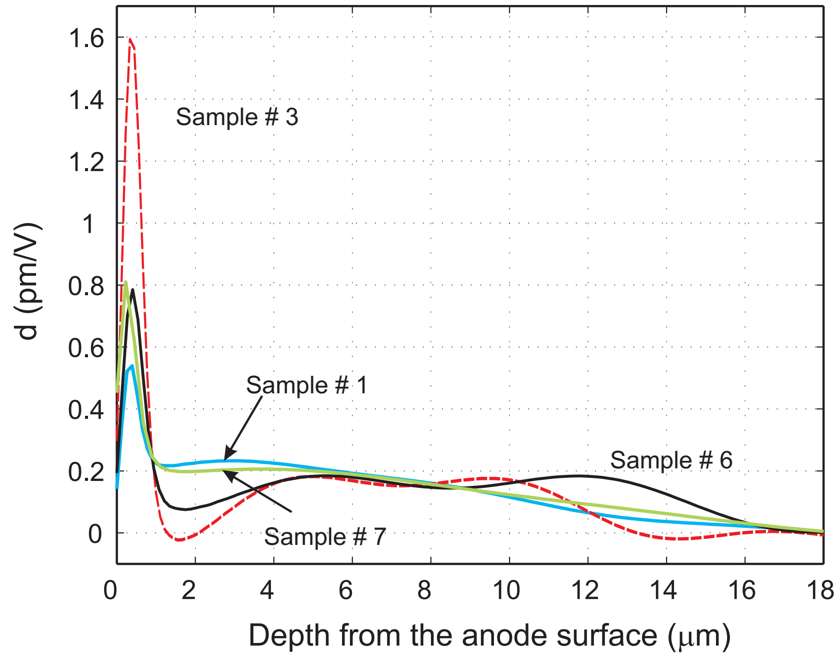

Figure 5.6: The recovered nonlinearity profiles of sample #1 (blue), #3 (red), #6 (black) and #7 (green).

that have migrated towards the cathode.

After optimizing the poling time, we investigated the effect of the germane flow rate on the induced nonlinearity profile. For this purpose, we poled samples #1, #3, #6, and #7, which all have 4-μm thick germanosilicate films but were grown with different flow rates, namely 0, 33, 50 and 90 sccm, respectively. The poling conditions for all four samples were identical, i.e., in air at ∼5 kV and 280 ℃, for 10 min. The recovered nonlinearity profiles are shown in Fig. 5.6.

The profiles exhibit the same characteristics as the previous samples (see Fig. 5.3), i.e., a dominant peak buried ∼0.5 μm beneath the anode surface, followed by an almost constant nonlinear region of same sign that gradually decreases to zero at a width of 13-16 μm. The peak d_{33} coefficients of samples #1, #6 and #7 are found to be 0.54, 0.78 and 0.81 pm/V, respectively. This investigation shows that the highest peak d_{33} coefficient (1.6 pm/V) is achieved for a germane flow of 33 sccm (sample #3). Even though a higher germane flow rate produces

a higher Ge concentration and thus a higher $\chi^{(3)}$, as confirmed in Fig. 5.4, the fact that the peak d_{33} coefficient is maximum in the 33–sccm sample suggests that the built-in field drops at higher Ge flow rates. To illustrate this point, the maximum built-in E-field in poled germanosilicate films, calculated from Eq. (5.36) using the measured peak d_{33} value and the calculated $\chi^{(3)}$ value for each sample, is also plotted as a function of germane flow rate in Fig. 5.4. The results reveal that the highest built-in field is achieved for the 33–sccm sample (#3) and that for higher germane flow rates the built-in field steadily drops. We mostly relate these observations to an increase in the film electrical conductivity as the Ge concentration in the film is increased, which has been previously confirmed [130]. On the other hand, the built-in field of the 33–sccm sample is higher than that of the 0–sccm sample (pure SiO_2), although the latter has a lower electrical conductivity. This points out that there exists an optimum electrical conductivity range for a given set of poling conditions. This hypothesis is supported by the fact that under similar poling conditions, Suprasil, which contains much less impurity than Infrasil and thus has a lower conductivity, develops a built-in field nearly one order of magnitude lower than Infrasil [112, 131].

Finally, we investigated the effect of the film thickness on the induced nonlinearity profile. For this purpose, we poled sample #5, grown with a 33–sccm germane flow rate to a final thickness of 2 μm, in air at $\sim$5 kV and 280 ℃, for 10 min. Fig. 5.7 shows the nonlinearity profile for sample #5. For comparison purposes, the nonlinearity profile of sample #3, which was grown at the same flow rate and poled under identical conditions but is thicker (4 μm), is also shown in Fig. 5.7. Note again that the nonlinearity peak is entirely contained in the film and the pedestal in the substrate. The two samples (#3 and #5) have very similar profiles, which was expected since they have the same material composition and were poled under the same conditions. However, the total depth of the nonlinearity is larger for sample #5 ($\sim$17 μm) than for sample #3 ($\sim$13 μm). We attribute this difference mostly to the fact that the 2-μm thick germanosilicate film in sample #5 acts as a weaker barrier for ion diffusion process than the 4-μm film in sample #3. Furthermore, we believe that this charge spreading is at the origin of the weaker peak d_{33} coefficient in sample #5 (1.02 pm/V, vs. 1.6 pm/V

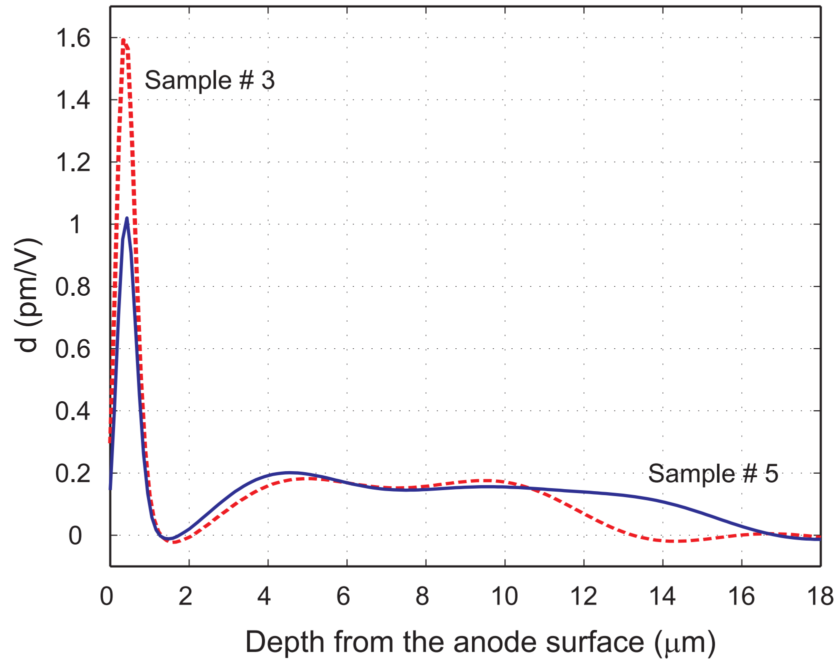

Figure 5.7: The recovered optical nonlinearity depth profile of samples #3 (red) and #5 (blue).

in sample #3).

In conclusion, we have reported measurements of the nonlinearity spatial profile of thermally poled germanosilicate films deposited on fused-silica substrates by PECVD. These films are interesting because they exhibit a low propagation loss and because they were expected to have a stronger nonlinearity than poled undoped silica due to the presence of Ge, which increases the third-order susceptibility of the glass. Inferred profiles all exhibit a sharp peak $\sim$0.5 μm beneath the anode surface, followed by a weaker pedestal of roughly constant amplitude and same sign down to a depth of 13$-$16 μm. These profiles are shallower and do not exhibit the sign reversal typical of poled undoped silica. These results suggest that during poling, the germanosilicate film significantly slows down the injection of positive ions from the anode surface into the structure. After optimizing the germane flow rate during deposition, the film thickness, and the poling time for maximum peak nonlinearity, we demonstrated a record peak nonlinear coefficient of $\sim$1.6 pm/V, approximately twice as strong as the highest reliable

value reported in a thermally poled fused silica glass. These findings are significant for the design of electro-optic devices using thermally poled germanosilicate thin films, especially for optimization of the overlap between the optical mode of the device and the nonlinear region.

Chapter 6

Application of Germanosilicate Layers to Ring Resonator Devices

Having optimized the compositional and nonlinear properties of germanosilicate dielectrics, we have demonstrated several applications of this technology in the field of integrated optics. Since optical waveguides constitute the building blocks of many integrated optical devices, we had first concentrated on design and optimization of waveguides employing germanosilicates as the core layers, as discussed in the first part of this chapter. The second part of the chapter deals with design and implementation of microring resonator devices based on germanosilicate layers. A systematic study carried out to determine the device geometry the best suitable for our purposes is reported. Finally, the obtained measurement results of various germanosilicate microring resonators are discussed.

6.1 Single Mode Germanosilicate Waveguides

Optical waveguides constitute the building blocks of many integrated optical devices. Consequently, their properties have to be optimized and analyzed in detail. For our purposes, in particular, we aim to use them in ring resonator based devices and all of the investigations to follow are carried out in the light of this goal. The core material to be made use of is germanosilicate, which has been optimized in terms of propagation loss (Chapters 3 and 4) and nonlinearity (Chapter 5) and a waveguide is to be tailored using optimized parameters.

6.1.1 Waveguide Structure

In the previous chapters the as-grown germanosilicate layers were shown to have promising characteristics such as adjustable index of refraction and low propagation losses for high refractive index ($\geqslant$1.50) materials. These properties make the mentioned material system a very attractive base for the realization of integrated optical devices, such as ring resonators.

For applications in ring resonators the waveguide structure is to be determined in accordance with the desired outcome. For example, in order to realize ring resonators with practical radii, the index of refraction of the material has to be relatively high, for strong mode confinement. On the other hand, for a device to be modulated electro-optically, the nonlinearity of the structure has to be high as well. Furthermore, the finesse (or Q-value) of the resonators should be as high as possible, i.e., the propagation losses are to be minimum. All these competing parameters are to be optimized for realization of a functional device relying on poled as-deposited germanosilicate layers. Based on the above mentioned restrictions the structure and geometry of the ridge waveguide was optimized.

Many applications in optical integrated devices require two dimensional optical confinement that is achieved by making use of, for example, ridge waveguides. The approximate modal characteristics of this structure can be calculated by using the well known effective index method [33, 53]. This method converts a

two-dimensional problem into several one-dimensional problems. The equations are solved for TE and TM modes in order to find the allowed values for the propagation constant at a particular wavelength. The method was implemented in a Mathcad code and the details of the calculation can be found elsewhere [33,53,54]. The mode spectrum and geometry of the waveguide were also tested by using a commercial BPM simulator (BeamProp). It employs numerical method known as Beam Propagation Method (BPM), by which the scalar or vector wave equation for any structure defined by $n = n(x, y, z)$ is solved. The germanosilicate based waveguides were simulated by this method as well, yielding a single mode operation, in accordance with the effective index method. The mode shapes of the TE and TM fundamental modes as obtained by BPM are depicted in Fig. 6.1. The parameters used in simulations were those determined to be the optimum ones. Namely the structure of the waveguide was as follows:

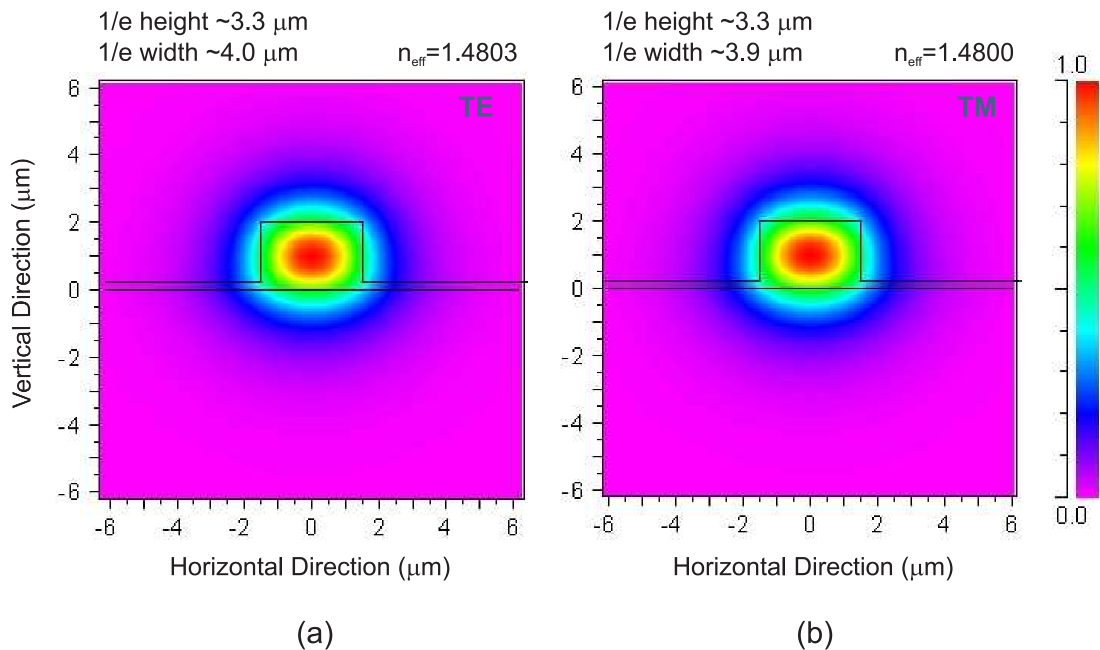

Figure 6.1: Fundamental mode profiles for (a) TE and (b) TM polarization of germanosilicate ridge waveguide as calculated by BPM.

Wavelength of operation → $\lambda = 1.55\ \mu$m
Upper and lower cladding: PECVD SiO_x → $n = 1.465$
Core layer: SiO_x:Ge → $n = 1.505$ (GeH_4 flow rate= 50 sccm)
Core thickness → 2.0 μm
Etch Depth → 1.75 μm
Waveguide width → 3.0 μm

The parameters were optimized after a systematic simulation process. The width of the waveguide was chosen to be 3 μm in order to maximize the interaction of the nonlinear region with the optical field. The height of the guiding film was chosen to be 2 μm in the first instance, and could be changed during the deposition process. The reason behind choosing this thickness was to minimize the distance between the planned top and bottom electrodes (for use in an electro-optical device). A GeH_4 flow rate of 50 sccm was chosen to have a higher index material in order to achieve better confinement and therefore smaller ring radii for the planned final device, though its nonlinearity coefficient was smaller than

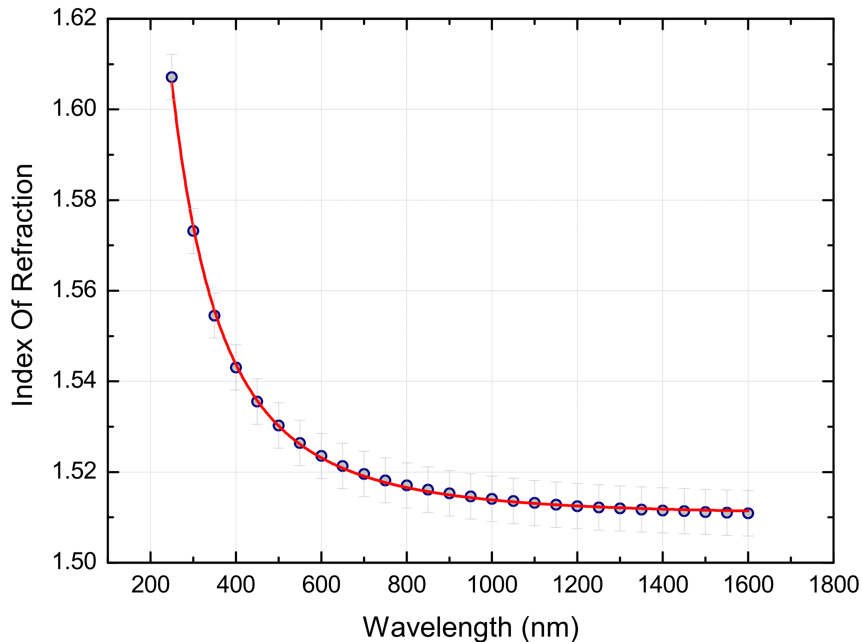

Figure 6.2: Index of refraction for the germanosilicate sample grown with GeH_4 flow rate of 50 sccm as a function of wavelength as measured by ellipsometry.

that of 33-sccm material (see Chapter 5). The wavelength dependent refractive index for the germanosilicate sample grown with GeH_4 flow rate of 50 sccm as measured by ellipsometry [132] is given in Fig. 6.2. The etch thickness could also be varied but the value of 1.75 μm was chosen considering the coupling factor and bending losses in ring resonator devices, to be discussed in detail in the next section.

Lastly, the structure of the waveguide aimed to serve as the building block for electro-optic ring resonator device was determined to be as follows: SiO_2 / electrode / PECVD SiO_x / PECVD $SiO_x : Ge$ / PECVD SiO_x / electrode. The vertical electrode structure here is preferred in order to take advantage of the fact that $d_{33} = 3 \times d_{31}$ (see Chapter 5). For the material of electrodes to be used we decided to concentrate on Indium Tin Oxide (ITO: 90% In_2O_3:10% SnO_2). The reason of preference of this material is its better performance in optical applications. Namely, it has been known for being transparent in optical wavelengths and introducing lower losses in the infrared region compared to metals such as gold, silver, nickel, etc. [133–135]. Having in mind these factors, the propagation loss of the waveguides should be measured and minimized, if possible. The following sections deal with the fabrication and optimization of the propagation loss for the above structure.

6.1.2 Fabrication Process

6.1.2.1 Growth of the Layers

The fabrication process of germanosilicate waveguides was performed in class 100 clean room environment. The process starts with an oxidized silicon wafer with SiO_2 thickness of $\sim$8 μm (see Fig. 6.3). The next step is to deposit a 150 nm thick ITO layer by reactive sputtering. For this purpose ultra high vacuum LE590 box coater, using radio frequency (RF) sputtering technique was employed. Prior to the sputtering process the pressure of the process chamber is lowered down to 5×10^{-6} mBar. The deposition rate and the total thickness of the film are monitored in-situ during the process. The sputtering is done in Ar atmosphere

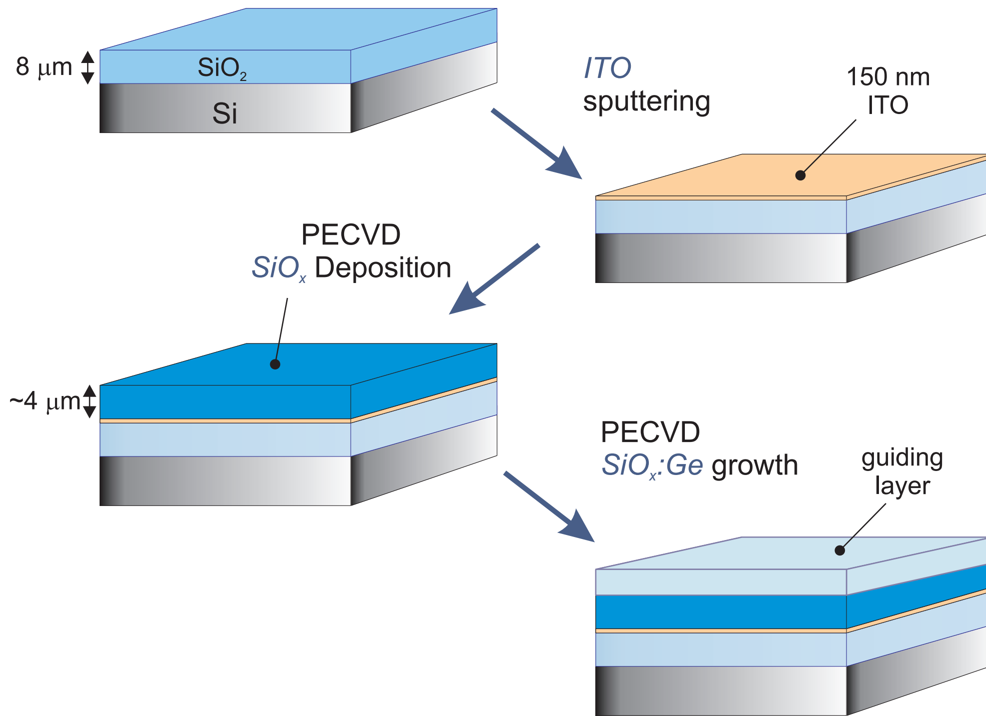

Figure 6.3: Schematic representation of the growth process of the layered structure for germanosilicate optical waveguides.

with a flow rate of 400 sccm and an RF power of 45 W. The resulting growth rate is about 2 Å/min.

Having grown an ITO layer of thickness of about 150 nm, the next step is to grow the SiO_x lower cladding layer by PECVD (see Fig. 6.3). This layer is deposited using the standard parameters of SiO_x growth (see Table 3.1). The growth of ITO onto silicon oxide and vice versa is highly favorable and was found not to cause any sticking problems due to the fact that both layers are oxides in nature thus easing the mutual atomic and molecular bond formation. After the lower silicon oxide cladding layer of thickness 3–5 μm has been grown, the germanosilicate layer aimed to serve as the core layer is grown by standard PECVD parameters and GeH_4 flow rate of 50 sccm. Thus, the initial layered structure for the optical waveguide is obtained.

6.1.2.2 Waveguide Ridge Definition

In order to transfer the waveguide strip pattern of the mask onto grown germanosilicate layer, a standard photolithographic process is used. The flowchart representation of the process is illustrated in Fig. 6.4.

The cleaned sample with previously grown layered structure is coated first with HMDS monolayer to improve the adhesion of the photoresist onto the surface of the film, spinning it at 5000 rpm for 40 seconds. The whole sample is then coated with AZ5214E negative photoresist (PR) material with thickness of ∼1.0–1.4 μm by spinning at 7000–5000 rpm (Fig. 6.4 (a)).

Following the application of PR, the sample is pre-baked for 50 s. at 110 ℃ to harden the photoresist and remove any residual solvents. The sample is then placed for alignment of the mask on a Karl Suss MJS33 mask aligner, that is used for UV exposure with a 365 nm Hg lamp in hard contact mode. In the image reversal pattern generation process the first exposure is done for 10 s. at 5.0 mW of optical power. Next, the reversal bake is done on a hot plate at 120 ℃ for 2 minutes. The sample is then placed in the aligner and a flood exposure is applied without the mask for 30 s. at 5.0 mW. Finally, the exposed photoresist is developed using 1:4 AZ400K:H_2O mixture in 30-50 s. (Fig. 6.4 (b)), depending on the exposure time and PR thickness.

The next step in the fabrication is to define the metal layer which is to serve as the hard mask during the reactive ion etching process (Fig. 6.4 (c)). Towards optimization of this step an extensive optimization of the PR thickness, development and metallic mask material was carried out. The first tested metal was Chromium (Cr). Several problems were identified and by varying the PR thickness, PR bake and development durations it was possible to partly overcome them. Namely, when the PR is spun at 4000 rpm, the resulting thickness of ∼1.4 μm is not sufficient for liftoff without ultrasound treatment. However, when the PR thickness was increased so as to obtain thickness of ∼1.65 μm, the liftoff was achieved.

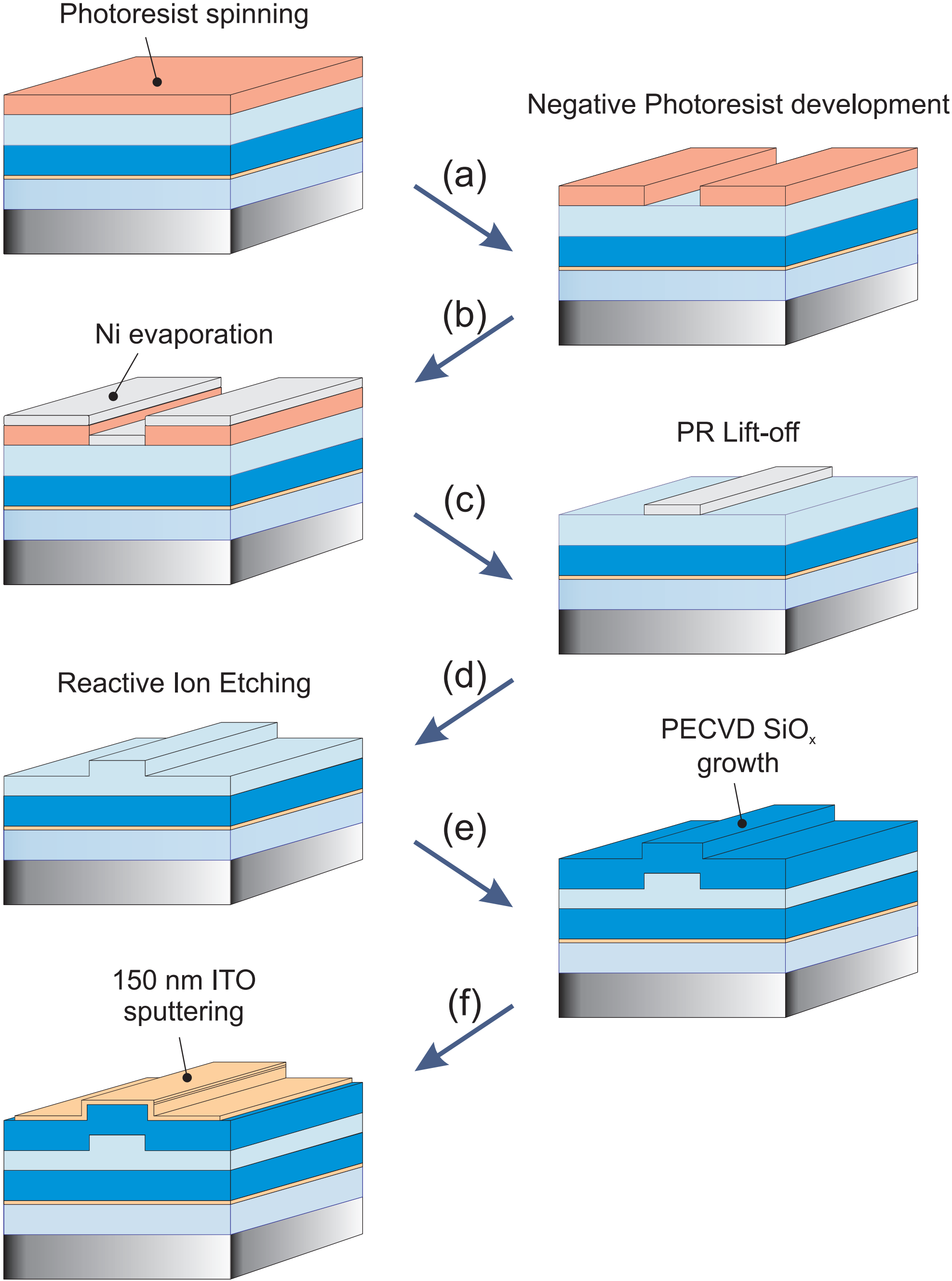

Figure 6.4: Schematic representation of the process of waveguide strip definition on the layered structure for germanosilicate optical waveguides.

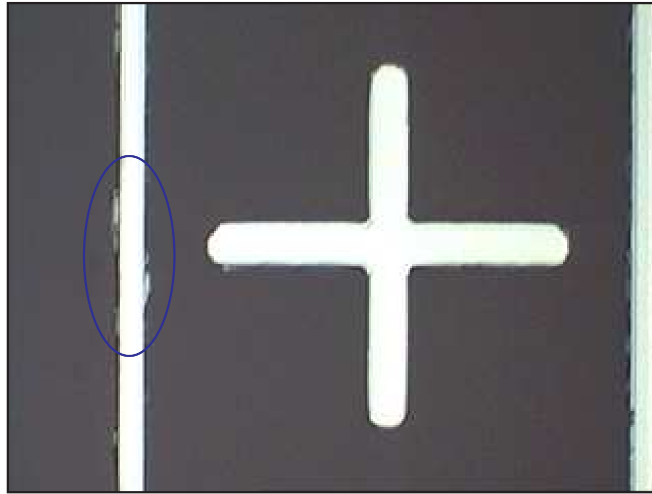

Figure 6.5: Formation of irregularities at the edges of the metal stripes after the liftoff process, as viewed with optical microscope. These wriggles are potential scattering sources increasing the propagation losses in optical waveguides.

An important problem worth mentioning was the formation of side defects (wriggles) at the edges of the metal layers after the liftoff process (see Fig. 6.5). In order to understand the origin of the problem the parameters such as pre- and post-bake, first and flood exposure durations had been varied. As a result, it was identified that the PR is being either under or over developed, thus resulting in poor liftoff, or liftoff with complications. For instance, in Fig. 6.6 the scanning electron microscope (SEM) image shows (a) the over developed PR structure and (b) the formed edge defects . Therefore, the problem could be avoided by either decreasing the exposure or the development time. However, the solution came with using Ni as a masking metal layer. Using this metal and optimized image reversal lithography proved to result in excellent waveguide strips defined without any wriggling and thus any extra propagation losses were avoided.

The next step in the fabrication is to etch the germanosilicate layer and define the strip of the ridge waveguide (Fig. 6.4 (d)). For this purpose a reactive ion etching (RIE) system reactor has been used, by which germanosilicate surface was etched using CHF_3 and O_2 gases. In the process of dry plasma etching, an RF glow discharge is excited in a high vacuum chamber between two electrodes, resulting

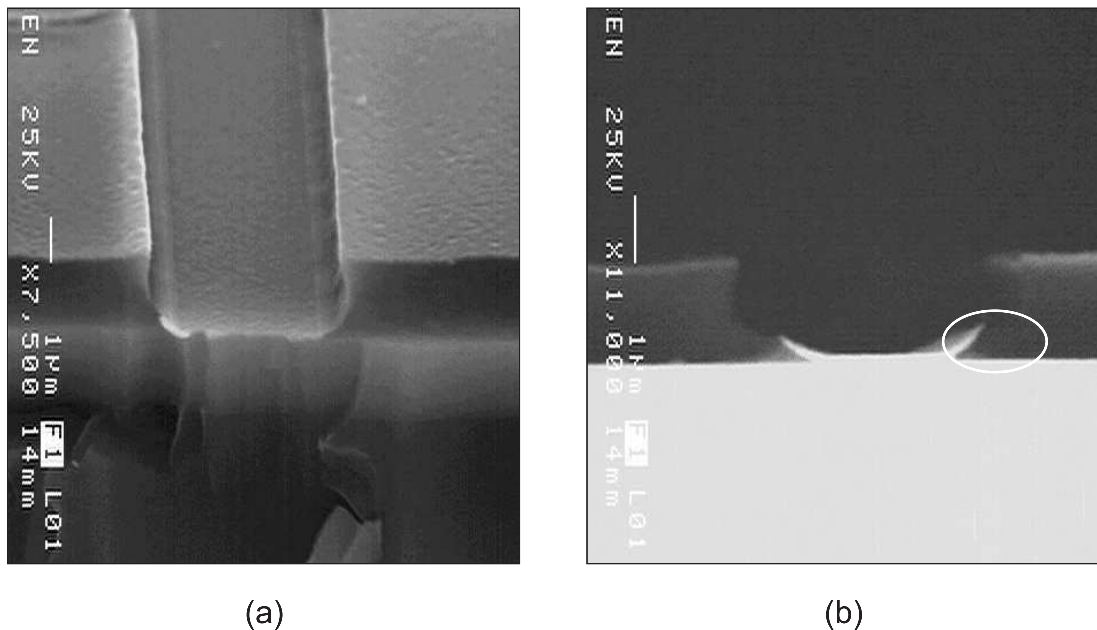

Figure 6.6: SEM images of the formed edge defects of Cr stripes in the overdeveloped samples after liftoff process. The over developed PR structure (a) and the formed edge defects (b) are clearly identified.

in chemically reactive species. These species react with the germanosilicate layer and form volatile products, which are pumped out from the chamber. In brief, the basic steps of the process are: 1) generation of reactive species from CHF_3 and O_2 by the plasma; 2) transportation of these species to the surface of germanosilicate layer; 3) adsorption of them on the surface; 4) formation of volatile products as a result of chemical reactions; 5) desorption of the by-products from the surface and pump-out. The overall process is a competition between physical sputtering and plasma etching, which favor anisotropic and isotropic etch, respectively.

The RIE process may have some side effects such as damage on the film surface, rough sidewalls of the defined rib, etc. A control over these parameters was established by careful optimization of the process conditions for a successful waveguide fabrication [33]. A study towards achieving this goal was performed by manipulating the variable parameters as indicated in Table 6.1. A delicate point is that production of waveguide strips having some degree of inclination was aimed.

Table 6.1: Optimized process parameters used in reactive ion etching of germanosilicate layers.

CHF_3 flow rate	150 sccm
O_2 flow rate	10 sccm
Process pressure	50 μbarr
RF power	150 W
Process time	30 min.

The driving reason behind this was to eliminate the problem of step coverage, during the final step of PECVD deposition of the upper cladding SiO_x layer. As a result, we were successful in fabricating strip side walls of ∼70° inclination, with good uniformity. The final steps towards fabrication of the germanosilicate waveguides is the growth of the upper cladding layers (Fig. 6.4 (e) & (f)). Upon the defined rib waveguide structure of germanosilicate, a SiO_x film is grown as an upper cladding. The growth parameters are identical with those of the lower cladding. The final step in the fabrication of waveguide devices is the sputtering

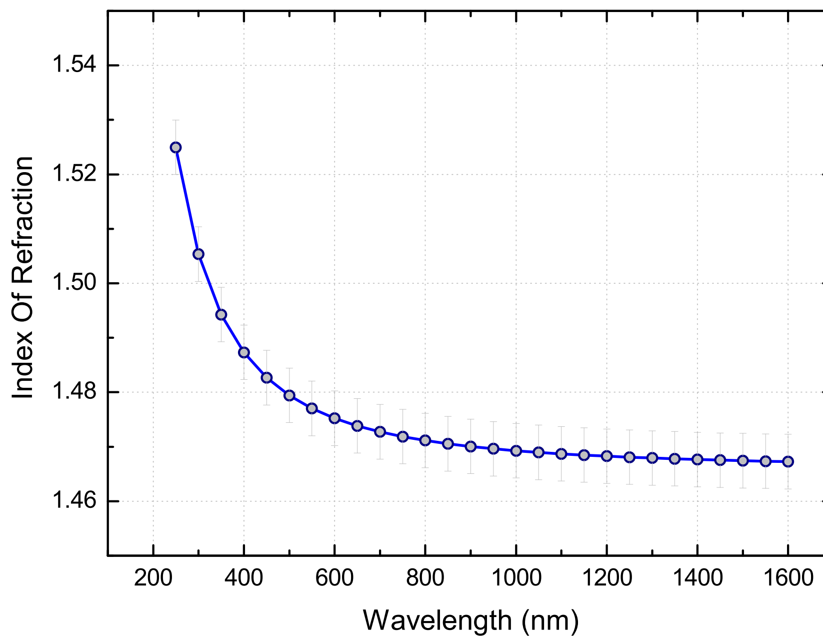

Figure 6.7: Index of refraction for the PECVD as-grown SiO_x film as a function of wavelength.

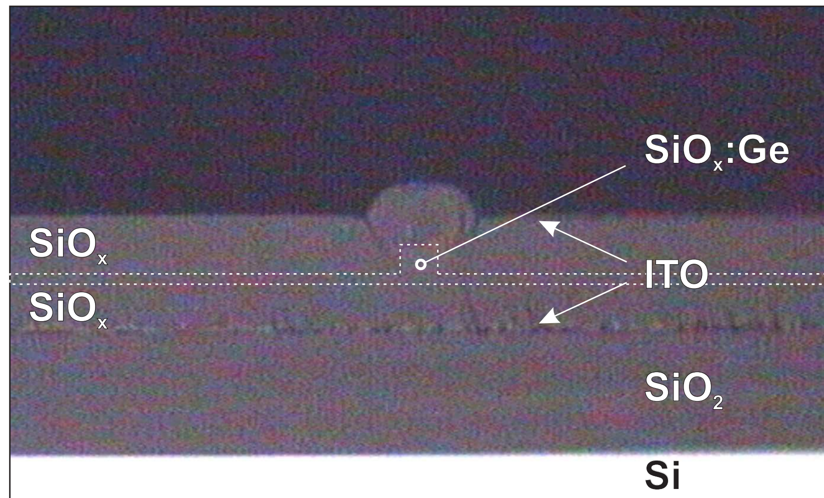

Figure 6.8: The final structure of the waveguide as viewed through an optical microscope. The Si, SiO_2, SiO_x, and ITO layers are clearly identified, while it is difficult to distinguish the SiO_x:Ge layer sue to the similar material nature.

of upper electrode ITO layer, which is done with the identical parameters as the lower one, discussed previously.

At this point it is useful to refer to the index of refraction of PECVD grown SiO_x as a function of wavelength. As it is evident from Fig. 6.7, the refractive index of the as-grown PECVD oxide is higher than that of thermally grown or annealed PECVD oxide [33]. For instance, at $\lambda = 1.55$ μm one would expect a refractive index of $\sim$1.45, while for our layer this value is $n = 1.465 \pm 0.005$ [132]. This slightly higher value has been taken into account in our calculations. Another important characteristic of the as-grown PECVD grown SiO_x films is that this film includes N−H bonds, thus introducing extra propagation losses to the waveguide [13]. This fact makes the measurement of the propagation loss for germanosilicate waveguides a very critical step. It is important to estimate precisely these loss values since performance of the final devise based on ring resonators is critically affected by it. For this purpose, a detailed measurement and optimization study for the loss values of germanosilicate waveguides was performed and is to be discussed in the next section. The final structure of the waveguide is depicted in Fig. 6.8 as viewed with an optical microscope.

6.1.3 Propagation Loss Measurement and Optimization of the Germanosilicate Waveguides

Having optimized the propagation losses of germanosilicate slab waveguides (Section 4.4), the propagation loss characteristics of a ridge waveguide device is to be investigated. The structure of this device was determined so as to serve as the building block for potential germanosilicate electro-optic ring resonators as discussed in the previous section.

6.1.3.1 Experimental Setup

After fabrication of the single mode ridge waveguides and the optical cleavage of their ends, their loss characteristics were analyzed by making use of the so called "butt coupling" method. The distinguishing feature of this technique is that the light is coupled into the waveguide by a single mode fiber, an out coupled by a lens which in turn directs the collected light to a Ge photodetector or an IR camera (see Figure 6.9). As a light source operating at 1.55 μm, a distributed feedback laser was used under 27 mA current and 25 ℃ temperature. It was attached to a fiber having polarization control module that allowed to select TE or TM polarized light. In some experiments the fiber used was lensed.

In addition, the sample was placed on an xyz translational stage enabling efficient coupling of the light into the guides. Additional pieozoresistive stages were also used to enable submicron alignment. As for the parameters measured, we could monitor the optical power transmitted using the Ge photodetector or the mode profile by an IR camera working in coordination with a video capture PC card.

6.1.3.2 Measurement Results

The single mode condition for the germanosilicate ridge waveguides with a ridge height of 1.75 μm and a total thickness of the core layer of 2.0 μm was verified

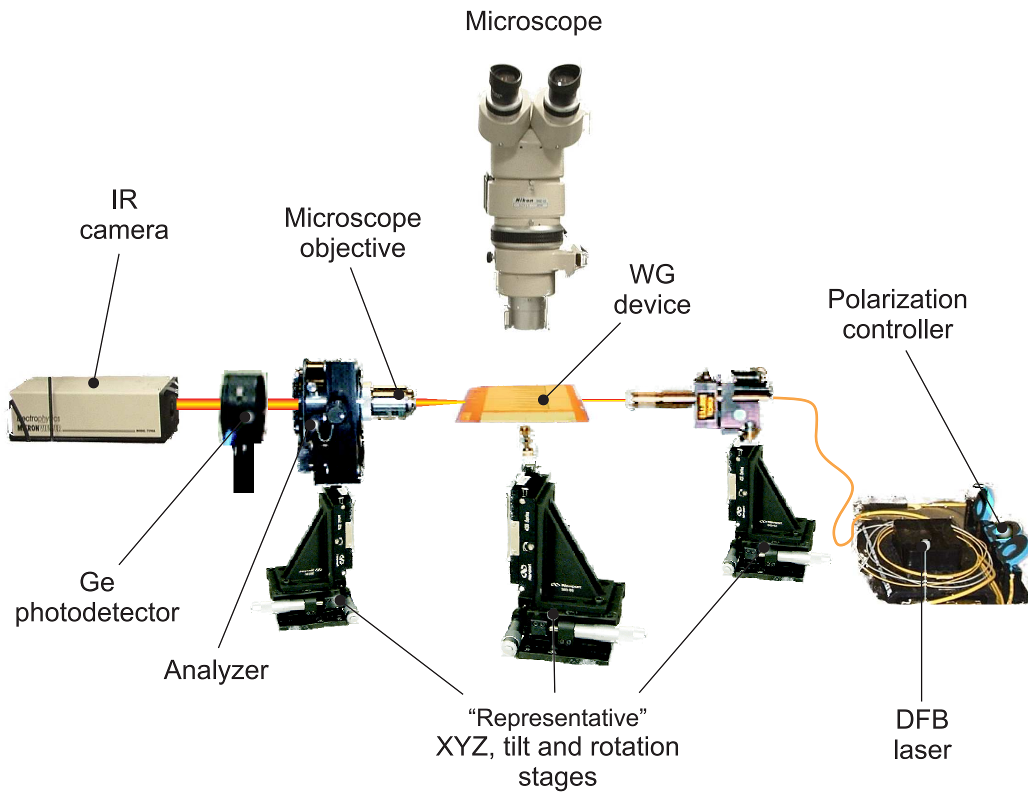

Figure 6.9: Optical waveguide devices measurement setup.

, as had been simulated by BPM (see Fig. 6.1). Experimentally, the well known method of directing the laser light in all possible off-axis positions in order to excite any possible higher order modes was employed. As expected, all the attempts resulted only in single mode operation profile.

Following the single mode verification, an insertion loss measurement on the germanosilicate ridge waveguides was performed. The insertion loss is measured in dB and includes the propagation loss as well as the fiber to guide and guide to objective coupling loss, in our case. Applying the cut-back method, identical waveguides at different lengths were characterized. At each length the measured insertion loss values are that of 15 to 30 different waveguides, allowing one to make a statistical analysis.

The measured values for the waveguides with a structure discussed in the

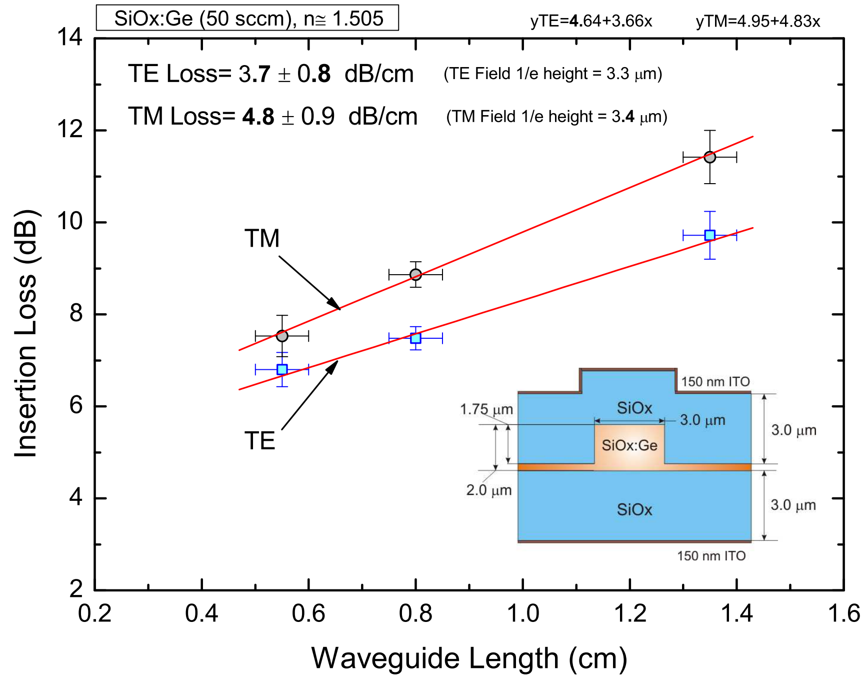

Figure 6.10: Insertion loss results for the TE and TM input polarized light for identical waveguides of different length. The waveguide geometry is depicted in the inset.

previous section are plotted in Fig. 6.10. Applying a linear fit to the loss data in the figure, from the slope we get the value of propagation loss of the ridge waveguides for TE and TM polarizations as:

$$\text{TE: Propagation Loss} = 3.7 \pm 0.8 \text{ dB/cm}$$
$$\text{TM: Propagation Loss} = 4.8 \pm 0.9 \text{ dB/cm.}$$

The y-axis intercept of the line fit to insertion loss data gives the coupling loss values for the waveguide structure. Analysis of the results leads to a conclusion that the fiber coupling loss together with WG to microscope objective loss is about 4.6 dB in total, which points out to a slight mode profile mismatch and reflection losses in the interface of the guide and fiber. The higher loss values for TM polarization indicate that some part of the mode still interacts with the conductive ITO layers. The propagation loss values for ITO itself are reported to be in the order of or larger than 400 dB/cm [135] at $\lambda = 1.55$ μm. This

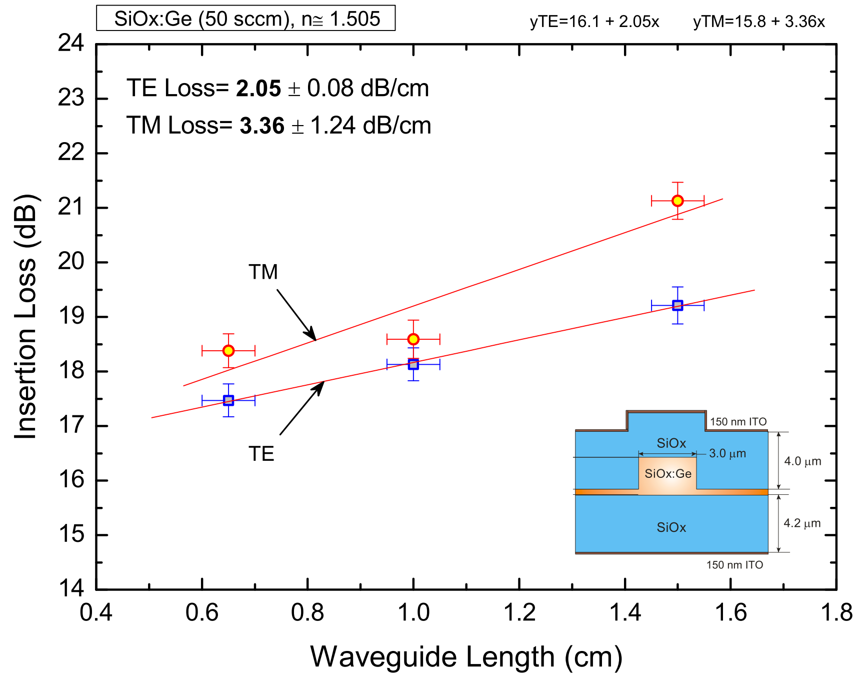

Figure 6.11: Insertion loss results for the TE and TM input polarized light for identical waveguides of different length and lower and upper cladding thicknesses increased to ∼4 μm. The waveguide geometry is depicted in the inset of the figure.

suggests that the propagation loss can possibly be further reduced by increasing the thickness of the SiO_x lower and upper cladding layers. Thereby, the next step was to fabricate and test optical waveguides with SiO_x cladding layer thicknesses of ∼4 μm, i.e. with thicknesses increased by about 1 μm. The insertion loss results of the waveguides with increased cladding layer thicknesses are shown in Fig. 6.11. Performing a similar analysis for propagation loss of the waveguides one obtains the following results:

$$\text{TE: Propagation Loss} = 2.0 \pm 0.1 \text{ dB/cm}$$
$$\text{TM: Propagation Loss} = 3.4 \pm 1.2 \text{ dB/cm.}$$

The propagation loss values are summarized in the Table 6.2. From the results it is apparent that the increase of the thickness of the upper and lower cladding layers has significantly reduced the propagation losses for both polarizations. This

Table 6.2: Summary of the propagation loss values for germanosilicate waveguides with different thicknesses of the cladding layers.

SiO_x	Propagation Loss	
cladding thickness	TE	TM
3.0 μm	3.7 ±0.8	4.8 ±0.9
4.0 μm	2.0 ±0.1	3.4 ±1.2

reduction of loss is in the order of 2 dB/cm and is quite significant, although the uncertainty in the loss value for TM mode in the second measurement is high. On the other hand, there is an apparent increase in the insertion loss values of the waveguide devices. This increase is due to the poor facet quality of the waveguides, which depends on the cleavage process. It should be noted that the none of the devices was polished, which can decrease the insertion losses significantly.

Normally, one would expect that the propagation losses for germanosilicate ridge waveguides are only slightly larger than that of the identical planar waveguides. That is the propagation losses are to be expected to be at most around 0.5 dB/cm. The material losses were minimized and the excess losses are expected to originate from the as-deposited SiO_x layers, rough surface of the waveguide rib, and finally from the upper and lower ITO electrode layers. It is possible to estimate the contribution of each. The maximal material loss contribution of the germanosilicate layer is about 0.3 dB/cm (see Section 4.4). As for the contribution from the cladding layers and the etch irregularities the expected value is about $\sim$0.4 dB/cm. This estimate is based on our previous work [13] on annealed silicon oxynitride (SiON) ridge waveguides that were fabricated identically with similar geometry and had as-deposited SiO_x layers as cladding between the core. Consequently, the remaining loss value of about 1.5-2.5 dB/cm is thought to originate from the interaction of the modal field with the top and bottom ITO electrode layers.

6.2 Germanosilicate Ring Resonator Devices

The integrated ring resonators were first proposed for use as a band-pass filter in 1969 by E. A. Marcatili [136]. The first ring resonators were demonstrated in optical fibers by Stokes *et. al* [137] and realization of the first ring resonators based on planar waveguides had to wait until 1996 [138, 139].

Recently a lot of research has been carried out for use of microring resonators (see Fig. 6.12) in integrated optics as all-optical switches, add-drop filters, electro-optic modulators, etc [21–23]. Current challenges in the field are to produce dielectric microring resonators with low-loss, large free-spectral range and desired characteristics of resonant wavelength adjustment and filter linewidth [24]. Resonator filter circuits based on dielectric layers offer several advantages. These materials are relatively inexpensive and their index contrast is easily adjustable. Moreover, their refractive index is suitable for matching with optical fibers and finally their dimensions are two or three times larger than their semiconductor counterparts, which allows efficient usage of optical without need for e-beam lithography [25]. Germanosilicates, therefore, offer a promising platform for applications of ring resonator devices [26, 27, 97]. The following sections introduce the basic notions of ring resonators and is followed by a report on fabrication and measurements of germanosilicate microring devices.

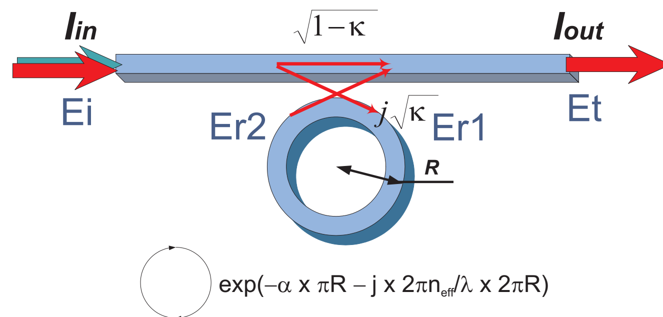

Figure 6.12: A schematic picture of a single bus microring resonator channel dropping filter.

6.2.1 Ring Resonator Devices Basics

The intensity relation for a single bus ring resonator (see Fig. 6.12) can be derived using a simple approach of directional couplers [21, 54, 140, 141]. If we denote the propagation constant as k_n, the radius of the ring as R, its circumference as L, the coupling factor as κ and the attenuation coefficient of the ring as α, the transmitted and inserted electric field relations (depicted in Fig. 6.12) can be written as:

$$E_t = (1-\gamma)^{1/2}\left[E_i\sqrt{1-\kappa} + jE_{r2}\kappa\right] \quad (6.1)$$

$$E_{r1} = (1-\gamma)^{1/2}\left[jE_i\sqrt{\kappa} + E_{r2}\sqrt{1-\kappa}\right] \quad (6.2)$$

$$E_{r2} = E_{r1} \times \exp\left(-\frac{\alpha}{2}L - jk_nL\right), \quad (6.3)$$

where γ is the coupling loss coefficient of the directional coupler and $k_n = \frac{2\pi n_{eff}}{\lambda}$, with n_{eff} being the effective refractive index. Using these equations, the ratio E_t/E_i can be written as:

$$\frac{E_t}{E_i} = (1-\gamma)^{1/2}\left[\frac{\sqrt{1-\kappa} - (1-\gamma)^{1/2} \times \exp\left(-\frac{\alpha}{2}L - jk_nL\right)}{1-(1-\gamma)^{1/2}\sqrt{1-\kappa} \times \exp\left(-\frac{\alpha}{2}L - jk_nL\right)}\right] \quad (6.4)$$

Furthermore, using the following new parameters for simplification:

$$D = (1-\gamma)^{1/2} \quad (6.5)$$

$$x = D\exp\left(-\frac{\alpha}{2}L\right) \quad (6.6)$$

$$y = \sqrt{1-\kappa} \quad (6.7)$$

$$\phi = \frac{2\pi n_{eff}}{\lambda}L \quad (6.8)$$

with

n_{eff} : effective index
γ : intensity insertion loss coefficient (0–1)
$L = 2\pi R$: circumference of the ring
α : attenuation coefficient of the ring
κ : coupling factor.

The intensity relation at the output port of the ring resonator is obtained as:

$$\frac{I_{out}}{I_{in}} = \left|\frac{E_t}{E_i}\right|^2 = D^2 \times \left[1 - \frac{(1-x^2)\times(1-y^2)}{(1-xy)^2 + 4xy\sin^2\left(\frac{\phi}{2}\right)}\right]. \tag{6.9}$$

Microring resonators have several parameters for evaluation of the system at resonance. These are the on-off ratio, free spectral range (FSR), i.e. the wavelength spacing between the adjacent resonances, full width at half maximum (FWHM) power of the resonance peak , and finesse (F) (see Fig. 6.13). The Q factor of the resonator is the ratio of the resonance wavelength to the FWHM, in other words:

$$F = \frac{FSR}{FWHM}, \tag{6.10}$$

$$Q = \frac{\lambda_m}{FWHM}. \tag{6.11}$$

High Q factors are important for optical signal processing applications,

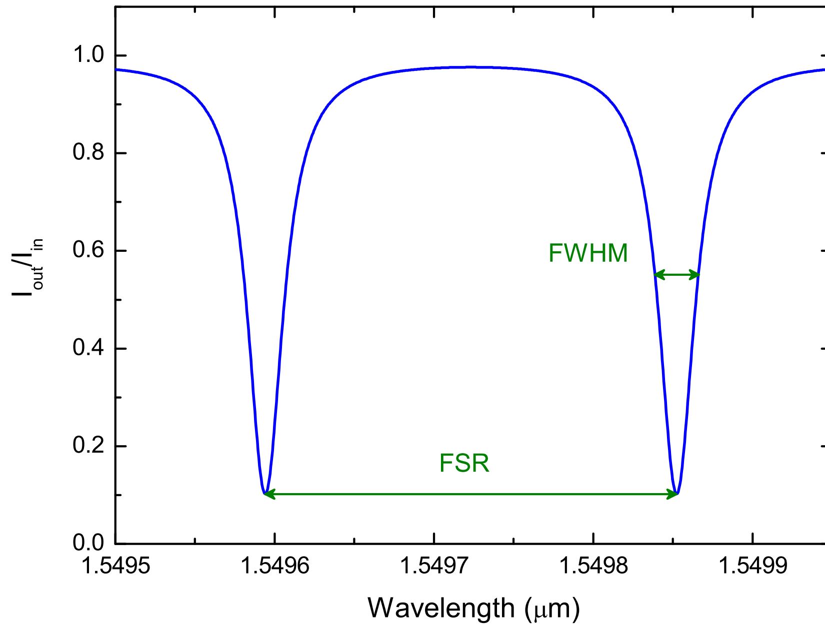

Figure 6.13: Calculated transmission characteristics of a sample single bus microring resonator.

whereas low finesse values (F=2) are used for interleavers [140]. Therefore, the quality and finesse of the resonators are to be chosen according to the desired applications, however it is safe to say that all the resonators require large on-off ratios and small FWHM.

The resonances of minimum transmission occur when

$$\phi = 2m\pi, \tag{6.12}$$

with m being an integer number. The minimum transmission, i.e. the highest on-off ratio, occurs at the so-called critical coupling condition when:

$$\alpha = -\frac{1}{L} \times \ln\left(\frac{1-\kappa}{D^2}\right). \tag{6.13}$$

It is evident that an estimation of the propagation loss value (i.e. α) for the ring resonator devices is critical. It is possible to design a resonator to operate at the critical coupling condition (Eq. (6.13)) by adjusting the coupling factor (κ). This would result in the maximum on-off ratio possible for a given propagation loss in the ring resonator. In our case, however, the primary aim is to optimize the device parameters for possible electro-optical operation of the poled germanosilicate ring resonators. Therefore, the main focus is to obtain as high Q-values (or F) as possible for the resonators that would enable detection of small changes in the effective index of ring resonators upon application of voltage. This can be achieved by designing the ring resonator so as to operate in an under coupled condition for a given propagation loss value. Namely, as Niehusmann *et al.* [142] report, the maximum achievable Q-factor at a given loss is calculated by:

$$Q_{\text{limit}} = \frac{2\pi n_{eff}}{\lambda}\frac{1}{\alpha} \tag{6.14}$$

and at the critical coupling condition the Q-factor of the device is only half of the maximum achievable. Therefore, we are to aim fabrication of microrings in an under coupled condition. By this way it is possible to approach the maximum possible Q-value for the ring resonator devices.

6.2.2 Bending Loss and Coupling Coefficient Calculations

6.2.2.1 Bending Loss Calculations

In order to design the ring resonator devices with desired characteristics one has to be able to successfully estimate the expected losses. In the previous sections a study for estimation of the propagation losses for linear germanosilicate waveguides with the desired structure has already been presented. However, for the ring resonators one has to take into account the bending nature of the waveguides in the ring section as well. The losses of these structures are called as bending losses and are as a result of continuous radiation of the waveguide mode power tangentially out of the curved waveguide, also called as leaky mode.

Estimation of the bending losses is possible with two different techniques. One of them is an analytical method while the other is an estimation using a commercial beam propagation method (BPM) program. We have made use of both techniques and will first concentrate on the analytical method. The analytical approach is based on the method of Marcuse [143]. It makes use of the effective index approximation by which the two dimensional index profile is reduced to a one-dimensional planar waveguide (see Fig. 6.14). In this method after a rigorous analysis of the the wave equation in cylindrical coordinates and using the effective index approach an analytical expression of the exponential power attenuation coefficient for the bending loss of a bent slab waveguide in rectangular coordinates is obtained [144]. The bending loss $Loss_{bend}$ (in dB) for a ring of radius R and angular section of $\Delta\theta$ radians is given by:

$$Loss_{\mathrm{bend}} = -10\log\Big(\exp\left(\alpha_{\mathrm{bend}} \times \Delta\theta \times R\right)\Big), \tag{6.15}$$

where the attenuation coefficient α_{bend} is:

$$\alpha_{\mathrm{bend}} = \frac{\alpha_y^2}{k_0^3 n_{\mathrm{eff}}\left(1+\alpha_y\frac{\omega}{2}\right)}\frac{k_y^2}{\left(n_{e2}^2-n_{e1}^2\right)}\exp(\alpha_y\omega)\times\exp\left(\frac{-2\alpha_y^3}{3n_{\mathrm{eff}}^2k_0^2}R\right). \tag{6.16}$$

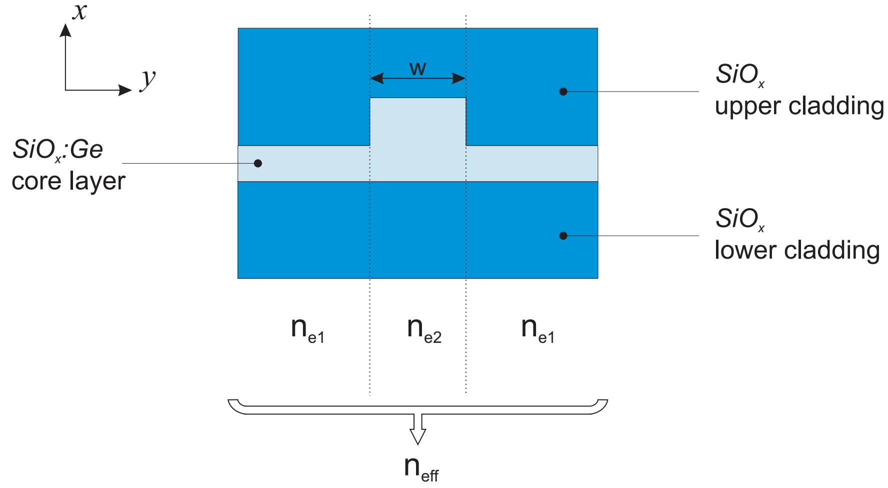

Figure 6.14: Schematic representation of the effective index model used to reduce the 3D structure to 2D.

The variables of which are further defined as:

$$\alpha_y = k_0\sqrt{n_{\text{eff}}^2 - n_{e1}^2} \tag{6.17}$$

$$k_y = k_0\sqrt{n_{e2}^2 - n_{\text{eff}}^2} \tag{6.18}$$

$$k_0 = 2\pi/\lambda_0 \tag{6.19}$$

with ω being the width of the waveguide (see Fig. 6.14), n_{eff} the effective refractive index of the waveguide, n_{e1} and n_{e2} the effective indices of the slab structures and λ_0 being the wavelength of light.

As for the estimation of bending losses numerically, we have made use of a commercial beam propagation method program, BeamPROP™ [145]. A 3D-BPM method with wide angle approximation was employed for a 20° bent section of the waveguide as depicted in Fig. 6.15. A computed mode profile of the straight waveguide was launched into the curved structure as described in [144]. The bending loss values, in dB/degree of arc length, were obtained directly by monitoring the decay of the mode power. The values were then scaled up to the desired arc length.

The waveguide parameters used in both methods were identical and were those of the devices used in the previous sections. Namely, the germanosilicate

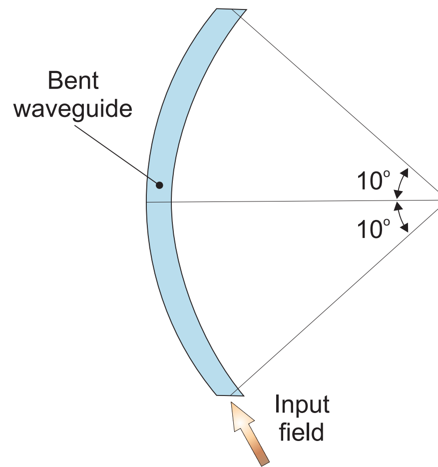

Figure 6.15: Waveguide layout model used for BPM simulation of bending losses in curved structures.

core layer with 2.0 μm thickness (t_{etch} = 1.75 μm) and n=1.505 was used. The lower and upper cladding layers refractive indices were both 1.465 at λ= 1.55 μm. The results obtained for this structure with both analytical and 3D-BPM methods are depicted in Fig. 6.16.

As it is evident from the figure, the bending losses decrease drastically for radii larger than 1000 μm for the both simulation methods. The first note to be made is that the bending losses were identical for TE and TM polarizations in the both methods. The next remark is that there is a small systematic discrepancy for the bending loss values between the analytical and 3D-BPM methods for radii between $\sim$750 and $\sim$1500 μm. According to the analytical model (Eqs. (6.15)–(6.19)) the bending losses are tolerable for radii larger than $\sim$750 μm and cease to negligible values for R $\gtrsim$ 1000 μm. As for the 3D-BPM simulation results, on the other hand, the bending losses become tolerable only at about $\sim$1000 μm and decrease slowly with increasing ring radius (see Fig. 6.16).

The apparent discrepancy between the bending loss results for the two methods can be understood if we take into account the limitations of the effective index approximations itself. It is well known that the results of the effective index method become unreliable when it is implemented in cases of strong optical

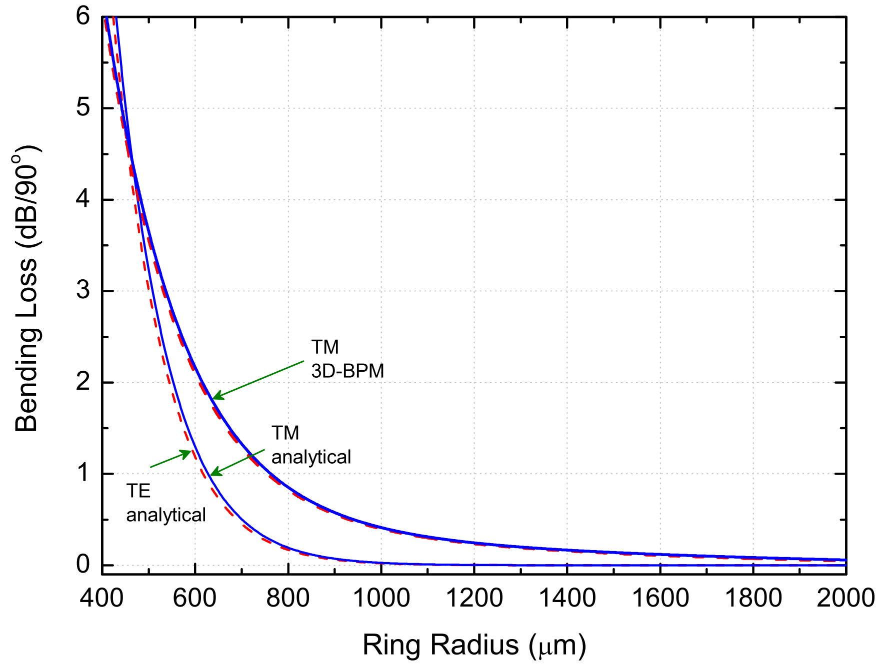

Figure 6.16: Bending loss results as extrapolated to 90° as a function of arc radius as calculated both analytically and by 3D-BPM.

confinement. This situation occurs either when using high index materials or when the waveguide is deeply etched [53]. The latter condition applies to our structure since the 2 μm germanosilicate layer is etched by about 1.75 μm and therefore the results obtained using this technique are to be treated with caution. In conclusion, the results show that the ring radii of the final devices should be larger than about ∼750 μm with optimum R of about ∼1100 μm in order to have tolerable losses.

6.2.2.2 Coupling Coefficient Calculations

Upon making an estimate for the losses of ring resonators that include propagation and bending losses, the next step is to determine the power coupling coefficient (or factor), κ, of the ring resonator. The coupling coefficients were determined by making use of 3D-BPM simulations. The geometrical configuration layout used in simulations is depicted in Fig. 6.17 (a). The power is launched into

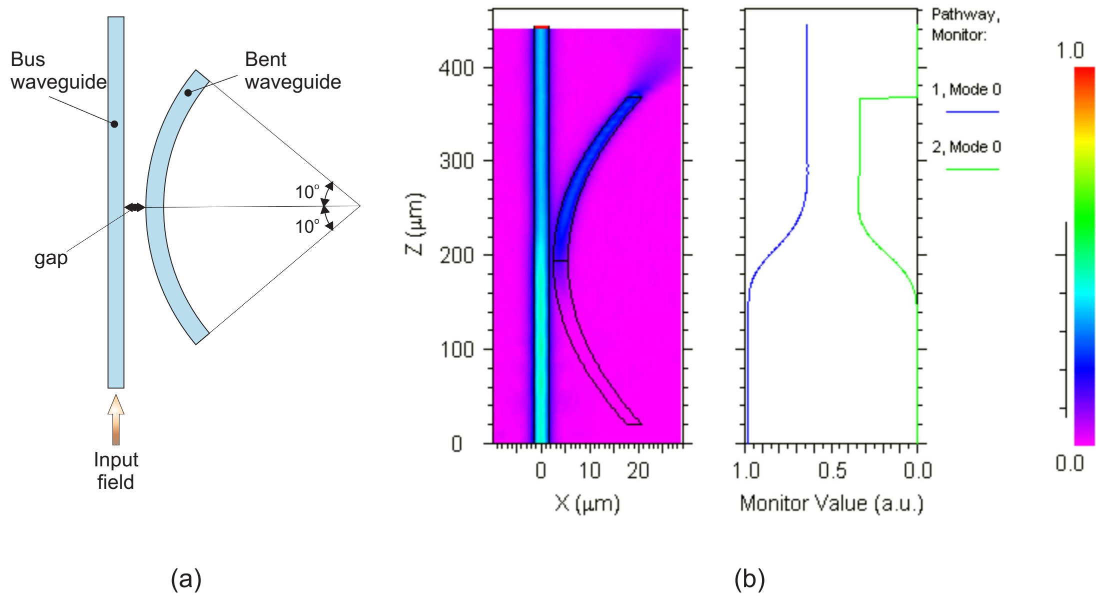

Figure 6.17: (a) Waveguide layout model used for 3D-BPM calculation of coupling coefficients, κ. (b) A sample simulation output for a device with a gap of 1 μm and R=1000 μm.

the straight bus waveguide and a fraction of it is coupled into the bent section, similar to the one used for bending loss simulations (see Fig. 6.17 (b) for a sample simulation). The optical power is monitored at the both ends of the straight and bent sections, being a direct measure for κ. The amount of the optical power coupled to the ring is critically dependent on the radius of the ring and the gap distance between the bus waveguide and ring section.

The simulation results of the power coupling factor for various ring radii as a function of gap length between the bus waveguide and ring section are summarized in Fig. 6.18. The lower limit for the gap length was chosen to be 0.8 μm, dictated by the lower limit of optical lithography tool available. The negligible birefringence of the germanosilicate waveguides with the described geometry reflects itself in the results such that the coupling coefficients are identical for both polarizations. The results show that the coupling coefficients are large enough for our parameters and there is no need to incorporate any straight waveguide sections in the coupling region (i.e. racetrack geometry).

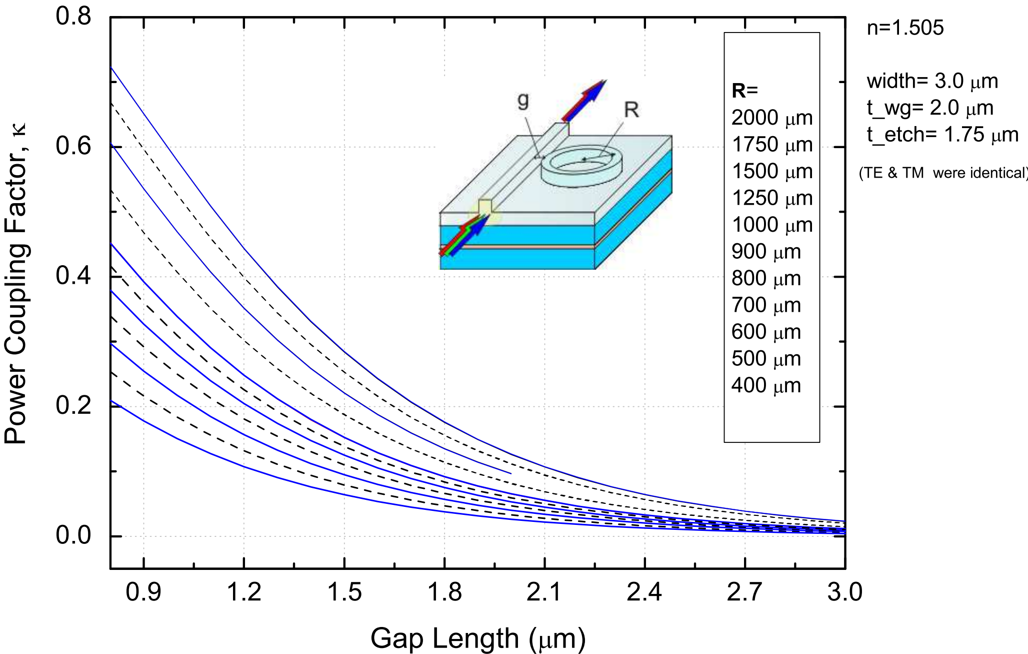

Figure 6.18: Coupling factors as calculated by 3D-BPM simulations as a function of gap length for various radii.

In conclusion, the outcomes of the calculations are to be used for the device design so as to adjust the gap between the ring and the bus waveguide in order to achieve the desired coupling coefficients.

6.2.3 Lithographic Mask Design Issues

Having made estimations for the propagation and bending losses together with the power coupling factors for germanosilicate microring resonators of different gap lengths and radii, the next step is to design a photolithography mask for fabrication of the devices. The choice of the radii of the rings was done according to bending loss calculations and were chosen to range between 750 and 1750 μm. The gap lengths between the bus waveguide and rings, on the other hand, were chosen so as to achieve a coupling coefficient, κ, below the critical coupling condition (Eq. (6.13)), i.e. under coupled. This was done with an aim as to have the highest possible Q-values for the ring resonator devices (see Sec. 6.2.1).

The next restriction was the limited area of the mask which should include the two step mask features. The first class of the patterns would be the ones to be used for definition of the ring and waveguide structures and the second one would include the upper-electrode patterns to be used for E-field application on potential electro-optic devices. Considering all the above limitations the mask design was made so as to include 16 devices in total. The geometrical structures of the devices included in the mask are listed in Table 6.3. The layout of the final mask is depicted in Fig. 6.19. The size of the final chip was intended to be 1" $\times$ 1", dictated by the size of Infrasil glass to be used as substrate for poled devices. The usable area of the mask in the aligner device was of approximately 4 cm $\times$ 4 cm size. For optimum usage of the area, therefore, the mask was divided into four parts with an area of about 2 cm $\times$ 2 cm each. The upper left and upper right corners in Fig. 6.19 depict the mask designs for ring resonator devices of two different chips. Five different radii with several gap lengths for each were included, resulting in a total of 16 different devices. The distribution of the ring resonator devices was done in order to maximize the area usage in

Table 6.3: The geometrical structures of the devices included in the photolithographic mask. Five different radii with several gap lengths for each were included, resulting in a total of 16 devices to be placed on two separate chips.

R (μm)	750	1000	1250	1500	1750
gap (μm)	0.8, 1.0, 1.2	1.0, 1.1, 1.3, 1.5	1.0, 1.1, 1.3, 1.5	1.0, 1.2, 1.4	1.0, 1.3

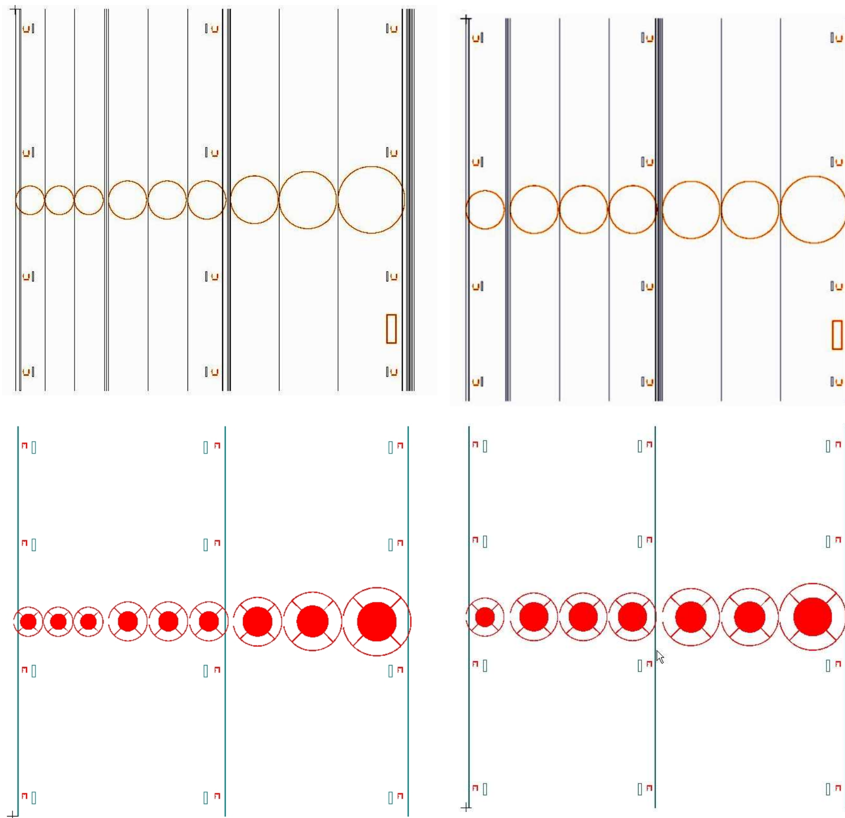

Figure 6.19: A two-step and two-chip photolithographic mask layout as designed with MEMS L-Edit and used for fabrication of germanosilicate ring resonator devices.

the most effective way. The separation between the ring and bus waveguide of the adjacent devices had been varied between 75-100 μm in order to ensure no optical power coupling among them (see Fig. 6.18), even for the slab modes.

The lower left and right corners in Fig. 6.19 show the mask design of the top electrode structures for the two ring resonator device chips. The lower electrode for the devices was aimed to be a full layer of ITO deposited below the lower SiO_x cladding and that of the upper electrodes was designed to have a geometry as in Fig. 6.19. The ITO layer of the top electrode structure was aimed to lie directly onto the waveguide of the ring structure and the pad was placed at the center. In the region of coupling the electrodes were removed so as not to affect the coupling coefficients. Additional alignment marks were included in the design

of each chip in order to facilitate the right placement of the top ITO electrodes.

All the mentioned mask features were realized by a commercial integrated circuit mask layout design program MEMS L-Edit™ [146]. The photolithographic mask had afterwards been fabricated by Photronics UK LTD [147]. The mask was fabricated on 4" × 4" quartz 1× master plate of 0.090" thickness. The address unit during mask production was set to 25 nm and the minimum critical dimension was 0.8 μm with a tolerance of ±0.10 μm. The desired cleanliness of the mask was maximum 1 defect/inch^2 over 1.0 μm. The mask was fabricated so as to bear the mirror image of the final design transferred to a Cr layer on the quartz mask and it had a 5-mm of clear window around the design in order to ease the alignment process.

6.2.4 Fabrication of Germanosilicate Microring Resonator Devices

The process of fabrication of the germanosilicate microring resonator devices is identical to that of linear waveguides (see Fig. 6.4). As a first step, the ITO layer of about 150 nm thickness is grown either on thermally oxidized SiO_2 layer or directly onto Infrasil substrate. The next step is to grow the ∼4 μm thick SiO_x lower cladding layer by PECVD (see Fig. 6.3). This layer is deposited using the standard parameters of SiO_x growth (Table 3.1). The germanosilicate core layer is then grown by standard PECVD parameters and with a GeH_4 flow rate of 50 sccm.

The lithographic process used to transfer the mask pattern to germanosilicate layer was identical to that discussed in detail in Sec. 6.1.2.2. The etch depth of the germanosilicate layer was about 1.75 μm. Fig. 6.20 shows the optical microscope image of a 750 μm radius ring resonator with a gap width of 0.8 μm fabricated as described above. A note should be made here on the fact that the photoresist (PR) treatment process was slightly modified. With the standard spin rates of 5000 rpm for PR the best resolution obtained for the gap length was about ∼1.2 μm. The negative photolithography steps were therefore modified so as to obtain

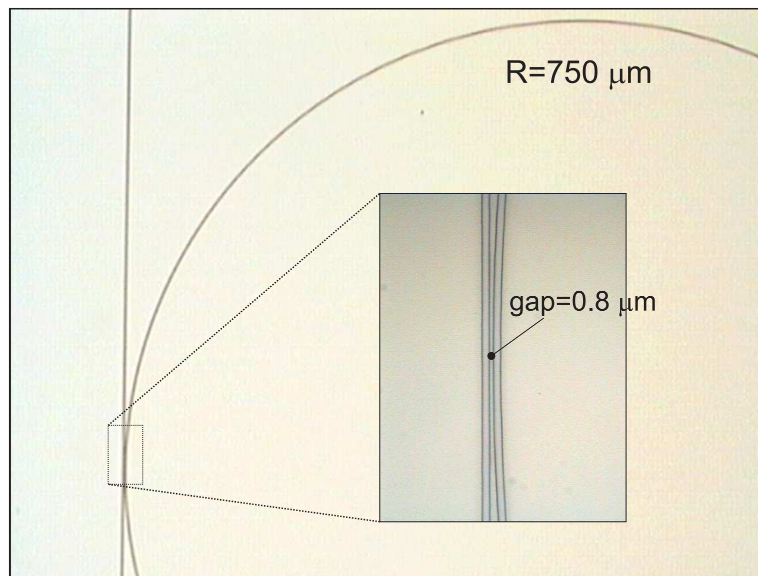

Figure 6.20: An optical microscope image of a 750 μm radius ring resonator. The inset shows in detail the coupling region and the 0.8 μm gap between the bus and ring waveguides, the widths of the waveguides are 3.0 μm.

the best possible resolution. The photoresist spin rates were increased up to 7000 rpm resulting in a thickness of about 1 μm. The edge beads of the chips were removed prior to exposure which proved to be one of the critical steps towards improvement of lithographic resolution.

After the definition of the waveguide and ring structures onto germanosilicate layer, the upper SiO_x cladding of about $\sim$4 μm in thickness was grown by PECVD with standard growth parameters identical to the lower cladding layer. As for the definition of the upper ITO electrode layer image reversal photolithography was used. After patterning the photoresist, the ITO film was sputtered with a thickness of about $\sim$150 nm. The liftoff process was performed in acetone for about 15 min. The resulting top ITO electrodes were of geometry the view of which is given in Fig. 6.21. It represents a schematic picture of the ring resonator device with the top ITO electrode structure. The insets show the optical micrographs of the top ITO electrode layers placed onto the waveguide ridge structures. The width of the waveguides is 3.0 μm, while the width of the ITO layer residing on them is about 15 μm. These electrode are connected to

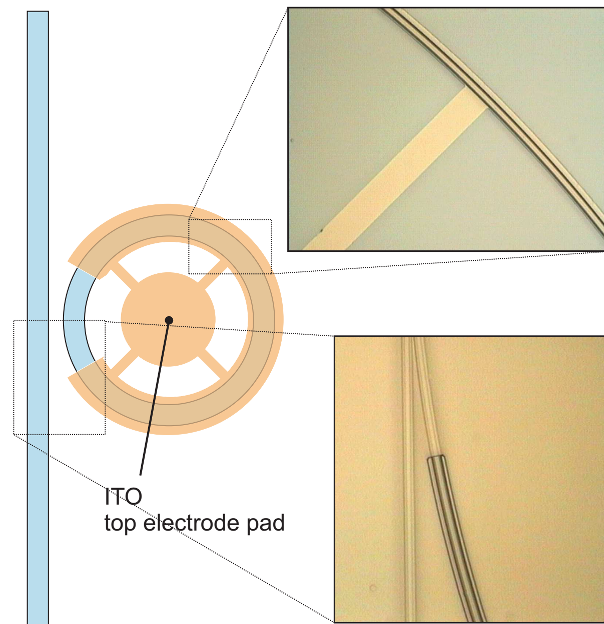

Figure 6.21: A schematic picture of the ring resonator device with the top ITO electrode structure. The insets show the optical micrographs of the top ITO electrode layers placed onto the waveguide ridge structures.

the pad with four smaller pads so as to enable uniform electric field application. The diameter of the pads varies between 800 and 2000 μm. The size of the final chips is about 2.5 cm $\times$ 2.5 cm. The optical cleavage of the facets was done manually for the devices fabricated on oxidized silicon wafer substrates. The devices fabricated onto Infrasil silica substrates were, on the other hand, optically polished in Stanford University.

6.2.5 Measurement Results for Germanosilicate Ring Resonators

The first step to be taken in the route of fabricating electro-optical ring resonator devices based on germanosilicate dielectric was to determine the optimum structure operating in passive configuration. For that purpose, the ring resonator devices were fabricated on oxidized silicon substrates with the geometry described in

the previous section. After the manual cleavage of the chips they were mounted on an integrated optics measurement setup, described in Fig. 6.9. As a light source, unlike the measurements performed for straight waveguides, an external cavity Santec TSL-320 tunable LD light source was used. The wavelength resolution used was 1 pm. The incoming light was coupled to the bus waveguides by a lensed and tapered single mode fiber. The polarization of the light was adjusted using a fiber polarization controller before being coupled to the device. The light was out coupled by a microscope objective and then directed to a Ge photodetector or an IR camera (see Fig. 6.9). In addition, a polarization analyzer with high extinction ratio was placed between the objective and the detector.

The measurement results of optical power as a function of wavelength for some of the ring resonator devices are depicted in Fig. 6.22. The measured

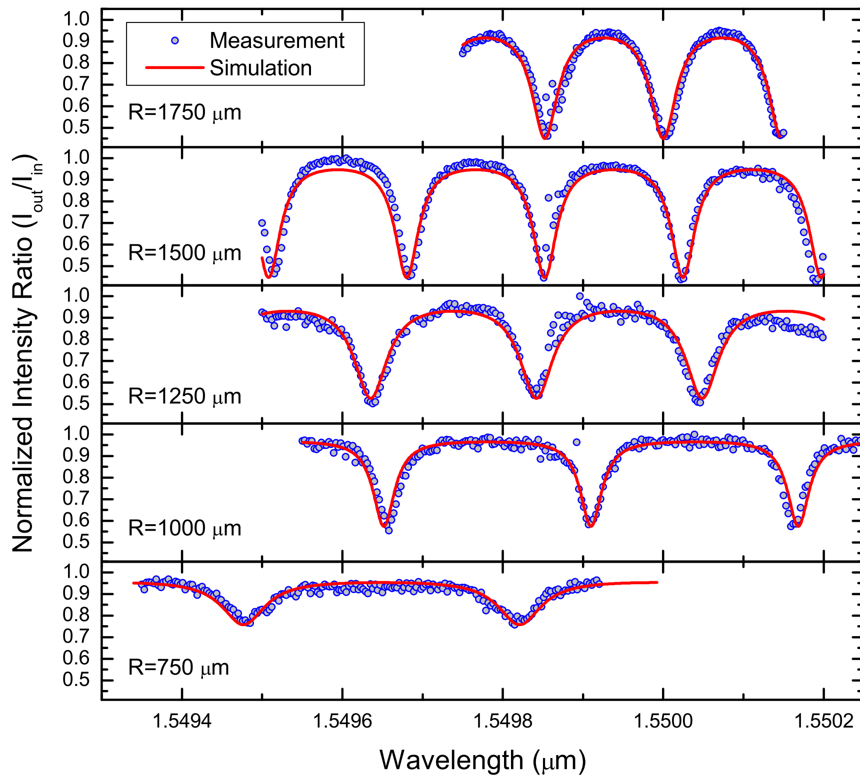

Figure 6.22: Transmission spectra results for some of the ring resonator devices with different radii as a function of wavelength at TE polarization.

Table 6.4: Summary of the measured characteristics of some of the germanosilicate microring resonators.

R (μm)	gap (μm)	Polarization	FSR (pm)	FWHM (pm)	Finesse	Quality Factor	Extinction Ratio (dB)
750	1.2	TE	345	78	4.44	2.0×10^4	1.0
		TM	345	63	5.48	2.5×10^4	0.7
1000	1.3	TE	259	34	7.60	4.6×10^4	2.2
		TM	259	40	6.38	3.8×10^4	1.8
1250	1.0	TE	207	51	4.06	3.1×10^4	2.5
		TM	207	51	4.05	3.0×10^4	1.7
1500	1.0	TE	172	36	4.77	4.3×10^4	3.3
		TM	172	35	4.98	5.0×10^4	2.2
1750	1.0	TE	147	40	3.69	3.9×10^4	3.1
		TM	147	46	3.23	3.4×10^4	2.2

characteristics of some of the ring resonator devices are further summarized in Table 6.4. The dots in the Fig. 6.22 correspond to the measured values, while the lines are the fitted curves of the intensity relation for a single bus ring resonator (see Sec. 6.2.1), i.e.:

$$\frac{I_{out}}{I_{in}} = \left|\frac{E_{out}}{E_{in}}\right|^2 = D^2 \times \left[1 - \frac{(1-x^2)\times(1-y^2)}{(1-xy)^2 + 4xy\sin^2\left(\frac{\phi}{2}\right)}\right], \tag{6.20}$$

where

$$D = (1-\gamma)^{1/2} \tag{6.21}$$

$$x = D\exp\left(-\frac{\alpha}{2}L\right) \tag{6.22}$$

$$y = \sqrt{1-\kappa} \tag{6.23}$$

$$\phi = \frac{2\pi n_{eff}}{\lambda}L \tag{6.24}$$

with

n_{eff} : effective index

γ : intensity insertion loss coefficient (0–1)

$L = 2\pi R$: circumference of the ring

α : attenuation coefficient of the ring

κ : coupling factor.

The fitting procedure was performed with a code realized in Mathcad providing us with the critical parameters of the ring resonator devices.

As evident from the Fig. 6.22 and Table 6.4, the simulation and experimental results are in a very good agreement. A steady decrease of the free spectral range (FSR) from 345 pm to 147 pm was observed as the ring radii increased from 750 to 1750 μm. The best Finesse (F) and quality factors (Q) were obtained for rings with radii of 1000 and 1250 μm. The highest F accompanied with high Q-value was measured for the device with R=1000 μm and gap width (g) of 1.3 μm (see Fig. 6.23). Inspecting the figure, a good correlation between the measured spectrum and analytical function fit of Eq. (6.20) is evidenced. The extinction ratios of the resonators were measured to be low, with the highest one being 3.3 dB. This fact would point to two possibilities. Either the propagation losses of the resonators are much larger than expected or the power coupling factors are lower than calculated. In order to further clarify this point, we tabulate the measured

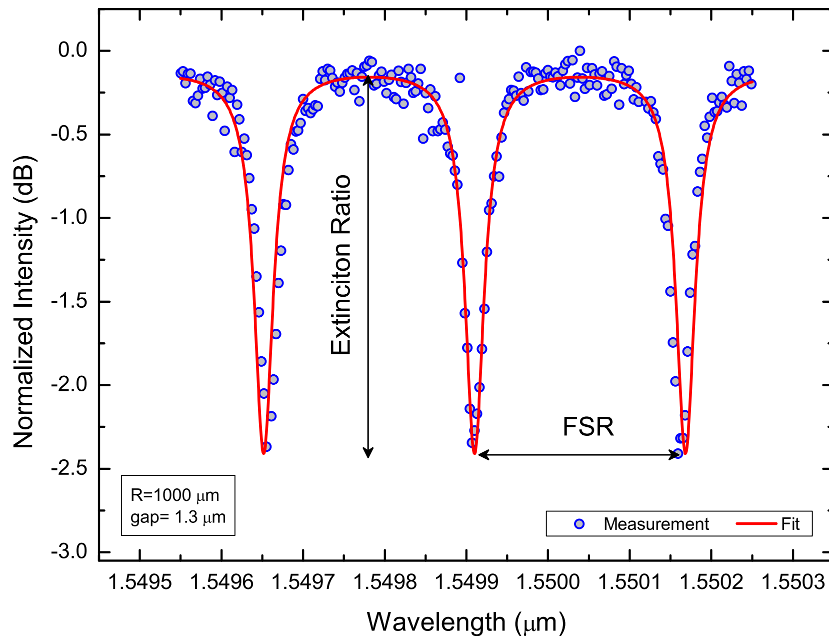

Figure 6.23: Transmission spectra results and analytical function fit to a single bus microring resonator with R=1000 μm and gap=1.3 μm at TE polarization.

Table 6.5: List of some of the critical parameters for germanosilicate ring resonators. The simulated values correspond to the expected parameters based on calculations and the experimental values are extracted from the fit of the analytical function of Eq. (6.20) to the measured transmission spectrum of each device.

Ring Radius (μm)	Parameter	Simulation	Experiment
750 (gap=1.2 μm)	FSR	344 pm	345 pm
(κ_{cr}=0.76)	κ	0.20	0.08
	Loss	13 dB/cm	15 dB/cm
	n_{eff}	1.4800	1.4800
1000 (gap=1.1 μm)	FSR	258 pm	259 pm
(κ_{cr}=0.58)	κ	0.34	0.09
	Loss	6.0 dB/cm	7.1 dB/cm
	n_{eff}	1.4800	1.4801
1250 (gap=1.0 μm)	FSR	207 pm	207 pm
(κ_{cr}=0.56)	κ	0.35	0.18
	Loss	4.5 dB/cm	7.6 dB/cm
	n_{eff}	1.4800	1.4800
1500 (gap=1.0 μm)	FSR	172 pm	172 pm
(κ_{cr}=0.58)	κ	0.47	0.19
	Loss	4.0 dB/cm	5.0 dB/cm
	n_{eff}	1.4800	1.4800
1750 (gap=1.0 μm)	FSR	148 pm	147 pm
(κ_{cr}=0.61)	κ	0.52	0.23
	Loss	3.7 dB/cm	6.5 dB/cm
	n_{eff}	1.4800	1.4800

and simulated characteristics for the resonator devices in Table 6.5. In the table, for each radius of the ring resonators with a given gap length, the parameters of free spectral range (FSR), power coupling coefficient (κ), propagation loss including material and bending losses (Loss), and the effective index (n_{eff}) are tabulated. The values of experimental column were found by performing an analytical fit of the Eq. (6.20) to the measured transmission spectrum of each device. As for the simulated parameters, they were obtained based on calculations described in Sec. 6.2.2 and the simulated loss values include both the calculated bending losses and the propagation losses measured for germanosilicate waveguides (see Fig. 6.11). In addition, for the calculated total propagation losses the values of critical power coupling coefficients (κ_{cr}) are given in brackets, for each device.

An excellent agreement between the foreseen and experimentally observed values of the FSRs for each device is observed. The same excellent correspondence is evidenced for the values of the effective indices of refraction, n_{eff}.

As for the propagation loss values, the bending losses were estimated with two different techniques, one using an analytical effective index approach and later based on 3D-BPM simulations (see Sec. 6.2.2.1). The two techniques resulted in quite different values of bending losses as a function of ring radius (see Fig. 6.16). Looking in the experimental propagation loss values listed in the table, we conclude that the 3D-BPM results estimates were more accurate. In accordance with the BPM estimations, the observed propagation losses decrease at the same rate as calculated and are in reasonable agreement, with the measured losses being a few dB/cm larger.

A considerable difference between the simulated and experimental results was observed in the power coupling coefficient values, κ. More than a two-fold difference was identified, with the experimental values being smaller. The method of simulation used in this study was already proven to result in good estimations and is not, therefore, considered to be the source of this apparent discrepancy [144, 148]. The decrease of the coupling factor dictated a more careful analysis of the coupling region between the bus waveguide and the ring structure in the resonator devices. A detailed optical microscope image of that region is given in Fig. 6.24.

The figure depicts the coupling region between a 3 μm wide waveguides of the bus and ring structures with a gap of 1.3 μm length in between. The left inset of the figure shows the magnified portion of the coupling region. All the fabrication steps for the device analyzed in the figure are completed. That is, the upper silicon oxide and ITO electrode layers are present. During the PECVD growth of the upper silicon oxide cladding layer a discontinuity region formation was identified. This discontinuity region is highlighted in the right inset of Fig. 6.24 and is marked as ①. The discontinuity region is formed because of the poor step coverage of the upper silicon oxide layer during the PECVD growth. The step coverage is expected to be even poorer especially in the coupling region,

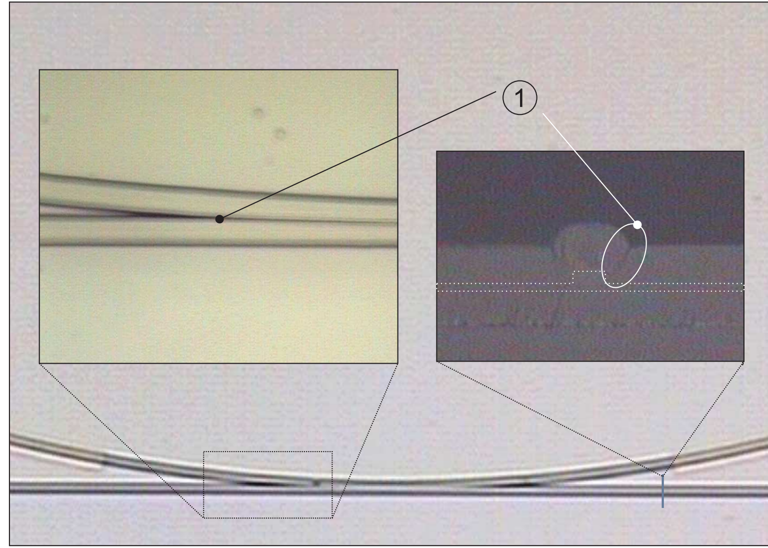

Figure 6.24: Optical microscope image of the coupling region between the bus waveguide and the ring structure in a resonator device with R=1000 μm and gap=1.3 μm. The left inset of the figure shows the magnified portion of the coupling region. The discontinuity region (trench) formed during the PECVD growth of the upper silicon oxide cladding layer is highlighted in the insets and is marked with ①.

where the two waveguides are in close proximity and the discontinuity is probably enhanced. In the process of optical power coupling from the bus waveguide to the ring waveguide and vice versa this discontinuity places a barrier and acts as a scattering center for the electromagnetic radiation. This in turn, may result in significant decrease in the optical power coupling factor and further increase in the propagation loss. The decrease of the power coupling coefficient was slightly effected also by the geometry of the waveguide, as well. Namely, during the fabrication the rib structure of the waveguide was over etched by about 0.1 μm. According to the 3D-BPM simulations an over etching by this amount decreases the coupling factor by less then 0.025, which is negligible compared to the observed discrepancy.

As a result, all the above mentioned observations suggest that the main cause for the discrepancy between the experimentally observed and the numerically

simulated coupling factors, apparently comes about from the formation of a discontinuity region in the coupling part upon growing the upper oxide layer. This discontinuity might further account for the slightly larger than expected propagation losses observed for all ring resonator devices. Although all the above referred artifacts result in decrease of the extinction ratio for ring resonators, their quality factors and finesse are appropriate and adequate in order to observe a possible electro-optical operation.

In order to further investigate the effect of ITO electrode layers on the performance of the microring resonator devices an additional study was performed. Germanosilicate ring resonators were fabricated without the ITO layers and the germanosilicate film was grown directly onto thermal SiO_2 layer. All the other specifications of the devices were identical to the ones grown with ITO electrodes. The main aim was to identify the contribution of ITO and SiO_x layers on the total propagation loss of the devices. The results obtained strongly confirmed the decrease of the propagation losses, as expected. A sample measurement spectrum is depicted in Fig. 6.25. The figure shows the transmission spectra results and

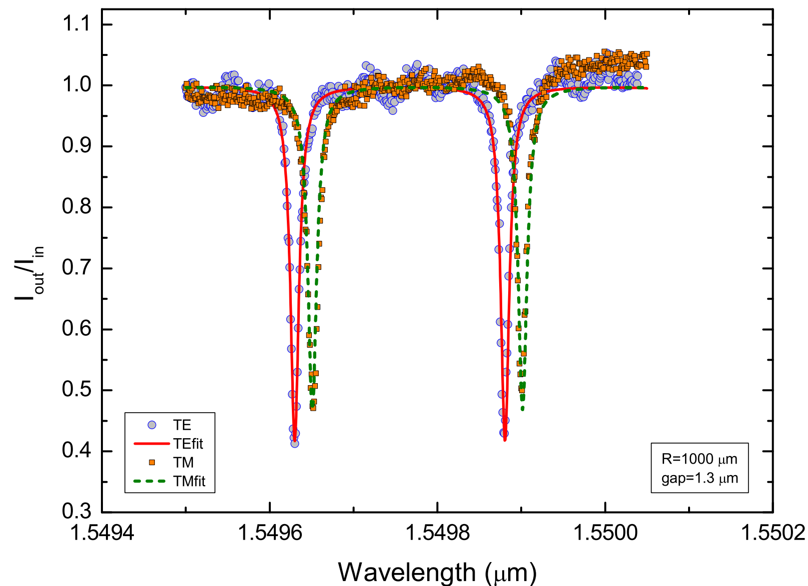

Figure 6.25: Transmission spectra result for a microring resonator with R=1000 μm and gap=1.3 μm at both TE and TM polarizations fabricated without the upper and lower ITO layers.

analytical function fit to a single bus microring resonator with R=1000 μm and gap=1.3 μm at both TE and TM polarizations. As evident from the figure, the slight shift of the drop wavelengths for TE and TM polarization is caused by an effective index mismatch of about 4×10^{-5}, proving the high sensitivity of the device on effective index changes. This device featured decreased total propagation loss and high finesse and Q-factor. Namely, the total propagation loss was determined to be about 2 dB/cm with Q=1.26×10^{5} and Finesse of 20.4. These values suggest a substantial increase of the device performance characteristics. A comparison of the critical ring resonator parameters was done for the devices fabricated with and without ITO layers and the results are plotted in Fig. 6.26. The figure depicts the measured (a) Q-factors, (b) Finesse values, and (c) the cal-

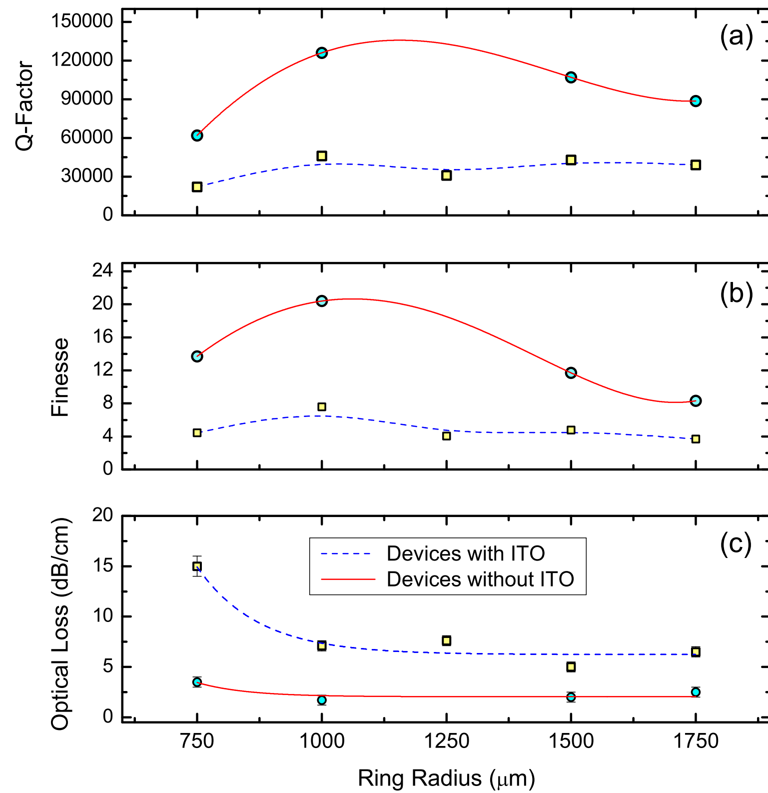

Figure 6.26: The measured (a) Q-factors, (b) Finesse values, and (c) the calculated propagation loss values determined from the function fitting for the ring resonator devices fabricated with and without ITO layers. The lines are drawn to guide the eye.

culated propagation loss values for the ring resonator devices fabricated with and without ITO layers. The loss values were determined by fitting Eq. (6.20) to the measured data. The fitting procedure was performed with a code implemented in Mathcad providing us with the critical parameters of the ring resonator devices. The propagation loss values were also calculated by using the method of Adar *et al.* [149, 150]. In this method the total propagation loss including material and bending losses is given by:

$$\text{Loss} = \frac{4.34}{F \times R \times (1+y)}, \tag{6.25}$$

where R is the ring radius, F is the measured finesse, y is the coupling loss to ring ratio calculated from the transmission minimum at resonance, T_{min} and the loss is given in dB per unit length. Here, y is calculated from

$$y = \frac{1 \pm \sqrt{T_{min}}}{1 \mp \sqrt{T_{min}}} \tag{6.26}$$

and the smaller of the two solutions for y is used, corresponding to the larger calculated loss [149].

The losses determined with the fitting procedure and by using Eq. 6.25 were in a very good agreement. The results are depicted in Fig. 6.26 (c). As evident from the figure, the highest propagation losses are that for the 750 μm ring radii devices and show a steady decrease with increasing radius.

As expected, the devices fabricated without ITO layers exhibit a drastic decrease in the propagation losses. This decrease in loss, on the other hand, expresses itself in abrupt increase of both Q-factors and finesses of the devices, as shown in Fig. 6.26 (a) & (b). Both of these values peak at R=1000 μm with Q = 1.26×10^5 and F = 20.4. The same radius has maximum Q and F values for the devices with ITO, however being less profound. The observed peak can be understood if we analyze, for example, the finesse of the devices. In order to have large F (F=FSR/FWHM), the device has to both be low-loss (resulting in small FWHM) and should have large FSR, i.e. small radius. The smallest radius with relatively low loss, in our case, happens to be met for R=1000 μm, in both the devices with and without ITO layers. Therefore, at this radius both the finesse and quality factors of ring resonators show a peak. With increasing

radius the rate of decrease of the propagation loss is less than the decrease in the FSR of the device, thus resulting in reduction of the finesse and Q-factor of the ring resonator devices.

Chapter 7

Conclusions

In accordance with the main goal of this work, that relies on the utilization of silicon based dielectrics and their optimization for applications in integrated optics, an emphasis was given to the compositional and optical properties of these materials.

In the growth of silicon based dielectric films a standard PECVD technique was employed. Using silane (2% SiH_4/N_2), ammonia (NH_3), nitrous oxide (N_2O), and germane (2% GeH_4/He) as precursor gases it was possible to obtain various films ranging from silicon oxide (SiO_x), silicon oxynitride ($SiON$), silicon nitride (SiN_x), germanosilicate ($SiO_x : Ge$) to germanate (GeO_x), including various combinations of them. Prior to this work the PECVD grown silicon based dielectrics were known to exhibit relatively large propagation losses in the communication wavelength (around 1.55 μm) and required an annealing treatment. Because the annealing step in any potential technology would limit its applicability and would increase the cost, one would be greatly interested in fabricating the devices on low-cost as-deposited layers instead.

The compositional properties of the films in our study were investigated via Fourier transform infrared (FTIR) transmission spectroscopy. Special attention was given to the absorption band of N−H bond stretching vibration, since its first overtone is known to be the main cause of the optical absorption at λ=1.55 μm.

In the first stage of our work we have investigated the compositional properties of silicon oxide, silicon nitride, silicon oxynitride, germania, and germanosilicate glasses and identified the germanosilicate dielectrics as the most promising candidates for use in integrated optics. Next, we focused on detailed quantitative compositional analysis of the germanosilicate films. Compositional analysis using FTIR spectroscopy showed that the amount of N−H and O−H related bonds exhibited a drastic decrease with increasing GeH_4 flow rate. N−H bond concentration of the films decreased from 0.43×10^{22} cm^{-3} down to below 0.06×10^{22} cm^{-3}, by a factor of seven as the GeH_4 flow rate increased from 0 to 70 sccm. A simultaneous decrease of O−H related bonds was also observed by a factor of 10 in the same germane flow range. This, therefore, pointed out to the fact that careful optimization of the germanosilicate layers could result in low-loss as-deposited dielectrics with potential applications in integrated optical devices.

Prism coupling technique has been used for characterization of the polarization dependent refractive indices and propagation losses at both $\lambda = 1.55$ μm and 632.8 nm. Our study was the first reported systematic study of propagation losses for different-index planar waveguides. This study had striking results in which planar waveguides fabricated with germanosilicate core layers showed the lowest propagation loss values reported so far for as deposited films at λ=1.55 μm, eliminating the need for costly and cumbersome annealing process. Specifically, the propagation loss values for TE polarization at λ=1550 nm were found to decrease from 0.32 $\pm$0.03 down to 0.14 $\pm$0.06 dB/cm, as the germane flow rate increased from 5 to 50 sccm, respectively. Furthermore, the decrease in the propagation loss of germanosilicates has been correlated with the decrease of the N−H bond concentration incorporated within the layers.

In the course of our study the prism coupling technique has been used extensively. Prism coupling measurements are often complicated by the softness of the films under investigation when stress is applied to the prism to couple light into the waveguides. Although this technique has been used for more than 30 years, the dependence of the refractive index, film thickness, and birefringence on the applied stress was not examined. The applied pressure was found not to be important if the waveguides investigated have hardness comparable with that of

the prisms (glass) used, e.g. germanosilicates. However, the effect of the applied stress is expected to become pronounced when "softer" layers are to be analyzed by prism coupling method (PCM). We have faced such problems during our study and due to lack of necessary investigation in the literature we have focused on the problem. A new approach was proposed for elasto-optic characterization of thin polymer films, making use of the well known prism coupling technique. This completely new method allows us to determine the optical anisotropy and out-of-plane mechanical properties and to correlate both in order to obtain the elasto-optical properties of thin polymer films, for the first time. Results of 3D FEM analysis together with the refractive index measurements were applied to the Neumann-Maxwell stress equations in order to obtain the elasto-optic coefficients for the PS, PMMA, and BCB thin films. To the best of our knowledge, these values are the first reported results for thin film polymers. In contrast with the measurements of elasto-optic coefficients made under tensile stress conditions for bulk polymers, it was found that the applied stress in the out-of-plane direction of the thin films investigated leads to negative elasto-optic coefficients, as observed for all of the three thin polymer films.

The investigations of optical properties of germanosilicate films continued with a focus on their nonlinear properties. Of interest as potential electro-optic devices, we have concentrated on thermally poled low-loss germanosilicate films deposited on fused-silica substrates by PECVD. In close collaboration with a group at Stanford University we have shown that nonlinearity profiles all exhibit a sharp peak $\sim$0.5 μm beneath the anode surface, followed by a weaker pedestal of roughly constant amplitude and same sign down to a depth of $13-16$ μm. After optimizing the germane flow rate during deposition, the film thickness, and the poling time for maximum peak nonlinearity, we demonstrated a record peak nonlinear coefficient of $\sim$1.6 pm/V, approximately twice as strong as the highest reliable value reported in a thermally poled fused silica glass. These results were important as they open a route for design of electro-optic devices based on thermally poled germanosilicate thin films.

Having optimized the compositional and nonlinear properties of germanosilicate dielectrics, we have demonstrated several applications of this technology in

the field of integrated optics. Since optical waveguides constitute the building blocks of many integrated optical devices, we had first concentrated on design and optimization of waveguides employing germanosilicates as the core layers. The waveguide structure was designed to have bottom and lower ITO electrode layers so as to allow their application in potential electro-optic devices. The effect of ITO layer and lower and upper cladding SiO_x thicknesses on the propagation losses was investigated. The results suggested that the increase of the thickness of the upper and lower cladding layers had significantly reduced the propagation losses for both polarizations due to the decreasing overlap of optical mode with the absorbing ITO layers. This reduction of loss was quite significant (of the order of 2 dB/cm). The germanosilicate waveguide devices containing ITO electrodes and as-grown SiO_x cladding layers were tailored an optimized with propagation losses of about 2 dB/cm, which although not being small, is suitable for demonstration of possible electro-optic application.

The final step of our work was to design and implement microring resonator devices based on germanosilicate layers having high finesse and quality factors. A systematic design study was carried out in order to determine the device geometry best suitable for our purposes. The ring resonator devices were fabricated on oxidized silicon substrates with the geometry identical to optimized linear germanosilicate ridge waveguides. The variation of critical parameters such as Q-factor, finesse and propagation loss with ring radii was analyzed. All the devices were designed to operate in an under coupled condition so as to obtain the maximum possible Q-factor for the ring resonator devices. In this respect, the effect of the bottom and lower ITO electrodes was also investigated by analyzing and comparing with the microring devices fabricated without them. As a result we have obtained maximum Q-factors of about 5×10^4 and finesse of about 7.6 for microring resonators fabricated with ITO electrode layers. As for the devices fabricated without the electrodes, the corresponding values showed an abrupt increase reaching a Q-factor of 1.26×10^5 and a finesse of 20.4. As a result of this study, in both types of the devices, the rings with radii of 1000 μm were identified to be the most suitable ones for a possible electro-optic microring resonator. Finally, an attempt to implement the observed electro-optic activity in a

ring resonator was made. However, difficulties in the final stages of fabrication, in particular facet preparation, did not allow for testing of the active device. As a concluding remark, we have performed a thorough optimization study of germanosilicate microring resonators resulting in determination of the optimum ring structure and geometry suitable for utilization of these devices in electro-optic modulators. As a future direction, implementation of the results of this work should lead to fabrication of the first silica based electro-optic modulators. In this regard, this work can be considered as an important contribution to the integrated optics community. The realization of an electro-optic modulator based on silica dielectrics would have a very high impact on the current state of the information technology.

Finally, my PhD work has resulted in six journal and ten conference publications (see Appendix A), all of which are peer reviewed, with one additional accepted article and one patent application.

Bibliography

[1] W. F. Brinkman, D. V. Lang, *Rev. Mod. Phys.*, **71**, S480 (1999).

[2] G.E. Moore, *Electronics*, **38**, 114 (1965).

[3] Y.P. Li, C.H. Henry, *IEE Proc.-Optoelectron.*, **143**, 263 (1996).

[4] S. Vallete, J.P. Jadot, P. Gidon, S. Renard, A. Fournier, A.M. Grouillet, H. Denis, P. Philippe, E. Desgranges, *Solid State Tech.*, **69**, Febr., (1989).

[5] H. Rong, R. Jones, A. Liu, O. Cohen, D. Hak, A. Fang, M. Paniccia, *Nature*, 3346, (2005).

[6] R.M. de Ridder, K. Wörhoff, A. Driessen, P.V. Lambeck, H. Albers, *IEEE J. Selec. Top. Quant. Elect.*, **4**, 930 (1998).

[7] K. Wörhoff, P.V. Lambeck, A. Driessen, *J. Lightwave Technol.*, **17**, 1401 (1999).

[8] R. German, H.W.M. Salemnik, R. Beyeler, G.L. Bona, F. Horst, B.J. Offrein, *IBM-Zurich Research Report*, RZ 3101 (# 93147), (1999).

[9] T. Baak, *Appl. Opt.*, **21**, 1069 (1982).

[10] M.J. Rand, R.D. Standley, *Appl. Opt.*, **11**, 2482 (1972).

[11] K.E. Mattsson, *J. Appl. Phys.*, **77**, 6616 (1995).

[12] M. Bass, E.W. Van Stryland, *Fiber Optics Handbook*, McGraw-Hill, New York, (2002).

[13] F. Ay and A. Aydinli, *Optical Materials*, **26**, 33 (2004).

[14] D. Moss, J. Canning, M. Bazylenko, *Conference on Lasers and Electro-Optics Technical Digest*, (Optical Society of America, Washington DC, 1998), p. 245.

[15] D.G. Chen, B.G. Potter, J.H. Simmons, *J. Non-Cryst. Solids*, **178**, 135 (1994).

[16] Q.Y. Zhang, K. Pita, C.K.F. Ho, N.Q. Ngo, L.P. Zuo, S. Takahashi, *Chem. Phys. Lett.*, **368**, 183 (2003).

[17] M. del Guidice, F. Bruno, T. Cicinelli, M. Valli, *Appl. Opt.*, **29**, 3489 (1990).

[18] F. Bruno, M. del Guidice, R. Recco, F. Testa, *Appl. Opt.*, **30**, 4560 (1991).

[19] D. Peters, K. Fischer, J. Müller, *Sensors and Actuators A*, **25-27**, 4560 (1991).

[20] D. E. Bossi, J. M. Hammer, J. M. Shaw, ”Optical Properties of Silion Oxynitride Dielectric Waveguides”, Appl. Opt., **26**, 609, (1987).

[21] A. Yariv, *Electron. Lett.*, **36**, 321 (2000).

[22] B.E. Little, S.T. Chu, H.A. Haus, J. Foresi, J.-P. Laine, *J. Lightwave Technol.*, **15**, 998 (1997).

[23] D.J.W. Klunder, F.S. Tan, T. van der Veen, H.F. Bulthuis, G. Sengo, B. Docter, H.J.W.M. Hoekstra, A. Driessen, *J. Lightwave Technol.*, **21**, 1099 (2003).

[24] B.E. Little, S.T. Chu, W. Pan, D. Ripin, T. Kaneko, Y. Kokubun, E. Ippen, *IEEE Photon. Techn. Lett.*, **11**, 215 (1999).

[25] A. Melloni, R. Costa, P. Monguzzi, M. Martinelli, *Opt. Lett.*, **28**, 1567 (2003).

[26] G. Bourdon, G. Alibert, A. Béguin, B. Bellman, E. Guiot, *IEEE Photon. Techn. Lett.*, **15**, 709 (2003).

[27] F. Ay, A. Aydinli, S. Agan, *Appl. Phys. Lett.*, **83**, 4745 (2003).

[28] M. L. Hitchman, K. F. Jensen, *Chemical Vapor Deposition: Principles and Applications*, Academic Press, London, (1993).

[29] B.S. Sahu, O.P. Agnihotri, S.C. Jain, R. Mertens, I. Kato, *Semicond. Sci. Tech.*, **15**, L11 (2000).

[30] M.K. Gunde, M. Maček, *Appl. Phys. A*, **74**, 181 (2002).

[31] W.L. Scopel, M.C.A. Fantini, M.I. Alayo, I. Pereyra, *Thin Solid Films*, **425**, 275 (2003).

[32] A. Sassella, A.Borghesi, F.Corni, A. Monelli, G. Ottaviani, R. Tonini, B. Pivac, M.Bacchetta, L. Zanotti, *J. Vac. Sci. Tech. A*, **15** , 377 (1997).

[33] F. Ay, *Silicon Oxynitride Layers for Applications in Optical Waveguides*, M.Sc. Thesis, Bilkent–Ankara, (2000).

[34] K.S. Potter, B.G. Potter, D.C. Mclntyre, P.D. Gandon, *Appl. Phys. Lett.*, **68**, 2011 (1996).

[35] O. Sugihara, M. Nakanishi, H. Fujimura, C. Egami, N. Okamoto, *J. Opt. Soc. Am. B*, **15**, 421 (1998).

[36] R.A. Jarvis, J.D. Love, A. Durandet, G.D. Conway, R.W. Boswell, *Electron. Lett.*, **32**, 550 (1996).

[37] N.B. Colthup, L.H. Daly, S.E. Wibwrley, *Introduction to Infrared and Raman Spectroscopy*, 3^{rd}Ed., Academic, Boston, (1990).

[38] J.M. Hollas, *Modern Spectroscopy*, 3rd Ed., Wiley, New York, (1996).

[39] W.A. Lanford, M.J. Rand, *J. Appl. Phys.*, **49**, 2473 (1978).

[40] Y.P. Chou, S.C. Lee, *J. Appl. Phys.*, **83**, 4111 (1998).

[41] G. Lucovsky, S.S. Chao, J. Yang, J.E. Tyler, R.C. Ross, W. Czubatyj, *Phys. Rev. B*, **31**, 2190 (1985).

[42] F. Ay, S. Agan, A. Aydinli, *Proc. SPIE Int. Soc. Opt. Eng.*, **5451**, 511 (2004).

[43] V.G. Plotnichenko, V.O. Sokolov, E.M. Dianov, *J. Non–Cryst. Solids*, **278**, 85 (2000).

[44] H.G. Tomkins, R.B. Gregory, P.B. Gregory, P.W. Deal, S.M. Smith, *J. Vac. Sci. Technol. A*, **17**, 391 (1999).

[45] J.C. Rostaing, Y. Cross, S.C. Gujrathi, S. Poulain, *J. Non-Cryst. Solids*, **97-98**, 1051 (1987).

[46] Q. Zeng, J.F. Stebbins, A.D. Heaney, T. Erdogan, *J. Non-Cryst. Solids*, **258**, 78 (1999).

[47] T. Kominato, Y.Ohmori, N. Takato, H. Okazaki, M. Yasu, *J. Lightwave Technol.*, **10**, 1781 (1992).

[48] P.K. Tien, R. Ulrich, *J. Opt. Soc. Am.*, **60**, 1325 (1970).

[49] R. Ulrich, R. Torge, *Appl. Opt.*, **12**, 2901 (1973).

[50] P.K. Tien, *Appl. Opt.*, **10**, 2395 (1971).

[51] P.K. Tien, R. Ulrich, R.J. Martin, *Appl. Phys. Lett.*, **14**, 291 (1969).

[52] T. Liu, R. Samuels, *J. of polymer Sci. part B*, **39**, 2481 (2001).

[53] C.P. Pollock, *Fundamentals of Optoelectronics*, Irwin, Chicago, (1995).

[54] K. Okamoto, *Fundamentals of Optical Waveguides*, Academic, San Diego, (2000).

[55] E.T. Kensky and D.E. Zelmon, *Rev. Sci. Instrum.*, **64**, 1794 (1993).

[56] J.B. Hurtado-Ramos, O.N. Stavroudis, H. Wang, G. Gómez-Rosas, *Opt. Eng.*, **39**, 558 (2000).

[57] R. Ramponi, R. Osellame, M. Marangoni, *Rev. Sci. Instrum.*, **73**, 1117 (2002).

[58] F.L. Pedrotti, L.S. Pedrotti, *Introduction to Optics*, 2nd Ed., Prentice, Englewood Cliffs, (1993).

[59] D.L. Lee, *Electromagnetic Principles of Integrated Optics*, Wiley, New York, (1986).

[60] P. H. Chantome, L. Escoubas, F. Flory, *Appl. Optics*, **41**, 3127 (2002).

[61] F. Michelotti, T. Gabler, H. Horhold, R. Waldhousl, A. Brauer, *Optics Comm.*, **114**, 247 (1995).

[62] K. Sasaki, K. Fujii, T. Tornioka, T. Kinoshita, *J. Opt. Soc. Am. B*, **5**, 457 (1988).

[63] R. Burzyanski, B.P. Singh, P.N. Prasad, R. Zanoni, G.I. Stegeman, *Appl. Phys. Lett.*, **53**, 2011 (1988).

[64] C.B. Rider, J.S. Schilckraut, M. Scozzafava, *J. Appl. Phys.*, **70**, 29 (1991).

[65] G. Arun, V.K. Sharma, A. Kapoor, K.N. Tripathi, *Optics and Laser Tech.*, **34**, 395 (2002).

[66] M. Ree, C.W. Chu, M.J. Goldberg, *J. Appl. Phys.*, **75**(3), 1410 (1994).

[67] H.C. Liou, R. Willacke, P.S. Ho, *Thin Solid Films*, **323**, 203 (1998).

[68] G.D. Shyu, A.I. Isayev, C.T. Li, *J. of Polymer Sci.*, **39**, 2552 (2001).

[69] M. Ree, T.J. Shin, Y.H. Park, S.L. Kim, S.H. Woo, C.K. Cho, C.E. Park, *J. of Polymer Sci. Part B*, **36**, 1261 (1998).

[70] L. Levi, *Applied Optics Vol.2*, Wiley, New York, (1980).

[71] R.D. Andrews, J.F. Rudd, *J. Appl. Phys.*, **28**, 1091 (1957).

[72] S. Monneret, P.H. Chantome, F. Flory, *J. Opt. A: Pure Appl. Opt.*, **2**, 188 (2000).

[73] J. Brandrup, H.H. Immergut, *Polymer Handbook*, 3rd Ed., Wiley, New York, (1989).

[74] S. Agan, F. Ay, A. Kocabas, A. Aydinli, *Appl. Phys. A – Mat. Sc. & Proc.*, **80**, 341 (2005).

[75] J. Massaneda, F. Flory, E. Pelletier, *Appl. Optics*, **38**, 4177 (1999).

[76] L.A. Hornak, *Polymers for Lightwave and Integrated Optics*, Marcel Dekker, New York, (1992).

[77] F. Ay, A. Kocabas, C. Kocabas, A. Aydinli, S. Agan, *J. Appl. Phys.*, **96**, 7147 (2004).

[78] A.M. Nasr, *Polymer Testing*, **21**, 303 (2002).

[79] T.C. Hodge, S.A.B. Allen, P.A. Kohl, *J. Pol. Sc., Part B: Pol. Phys.*, **37**, 311 (1999).

[80] R.S. Kumer, I.K. Schuller, S.S. Kumar, *Mater. Res. Soc. Symp. Proc.*, **308**, 503 (1993).

[81] K.S. Patel, P.A. Kohl, S.A.B. Allen, *IEEE Trans. Comp.,Pack., Manif., Techn.-Part B*, **21**, 199 (1998).

[82] W.C. Oliver, C.J. McHargue, S.J. Zinkle, *Thin Solid Films*, **153**, 185 (1987).

[83] B. Du, O.K.C. Tsui, Q.Zhang, T. He, *Langmuir*, **17**, 3286 (2001).

[84] J. Brandrup, E.H. Immergut, *Polymer Handbook*, 3rd Ed., Wiley, New York, (1989).

[85] G. Leclerc, A. Yelon, *Appl. Opt.*, **23**, 2760 (1984).

[86] R.V. Tanikella, S.A. Bidstrup Allen, P.A. Kohl, *J. Appl. Pol. Sc.*, **83**, 3055 (2002).

[87] V. White, R. Ghodssi, G. Fish, C. Hardey, H. Liu, D.D. Denton, L. Mc-Caughan, *IEEE Phot. Technol. Lett.*, **7**, 772 (1995).

[88] J.F. Rudd, E.F. Gurnee, *J. Appl. Phys.*, **28**, 1096 (1957).

[89] K.S. Patel, P.A. Kohl, S.A.B. Allen, *J. Pol. Sc. Part B: Pol. Phys.*, **38**, 1634 (2000).

[90] H.C. Liou, P.S. Ho, R. Stierman, *Thin Solid Films*, **339**, 68 (1999).

[91] K. Fischer, J. Muller, R. Hoffmann, F. Wasse, D. Salle, *IEEE J. Lightwave Technol.*, **12**, 163 (1994).

[92] A. Kuske, G. Robertson, *Photoelastic Stress Analysis* ,Wiley, New York, p.87 (1974).

[93] F. Flory, D. Endelema, E. Pelletier, I. Hodginkson, *Appl. Opt.* **32**, 5649 (1993).

[94] F. Horowitz, S.B. Mendes, *Appl. Opt.*, **33**, 2659 (1994).

[95] J.W. Dally, W.F. Riley, *Experimental Stress Analysis*, 3rd Ed., McGraw-Hill, New York, p.380 (1991).

[96] R.J. Pressley, *Handbook of Lasers*, CRC, Ohio, p.481 (1971).

[97] A. Ozcan, M.J.F. Digonnet, G.S. Kino, F. Ay, A. Aydinli, *Optics Express*, **12**, 4698 (2004).

[98] A. Saleh, C. Teich, *Fundamentals of Photonics*, Wiley, New York, (1991).

[99] A.C. Liu, *Poled Silica: Material and Device Characterization*, Ph.D. Thesis, Stanford, (1999).

[100] W.B. Leigh, *Devices For Optoelectronics*, Dekker, New York, (1996).

[101] P. Chakraborty, *J. Mater. Sci.*, **33**, 2235 (1998).

[102] P.N. Butcher, D. Cotter, *The Elements of Nonlinear Optics*, Vol. **9** of Cambridge Studies in Modern Optics, Cambridge, (1991).

[103] J. Jerphagnon, S.K. Kurts, *J. Appl. Phys.*, **41**, 1667 (1970).

[104] D. Pureur, A.C. Liu, M.J.F. Digonnet, G.S. Kino, *Opt. Lett.*, **23**, 588 (1998).

[105] F. Pockels, *Lehrbuch der Kristalloptik*, Teubner, Leipzig, (1906).

[106] R.W. Boyd, *Nonlinear Optics*, Academic, London, (1992).

[107] R.A. Myers, N. Mukerjkee, S.R.J. Brueck, *Opt. Lett.*, **16**, 1732 (1991).

[108] A. Ozcan, M.J.F. Digonnet, G.S. Kino, *Electron. Lett.*, **39**, 1834 (2003).

[109] P.G. Kazansky, P.S. Russel, *Opt. Commun.*, **110**, 611 (1994).

[110] Y. Ren, C.J. Marckmann, R.S. Jacobsen, M. Kristensen, *Appl. Phys. B: Lasers and Optics*, **78**, 371 (2004).

[111] L.J. Henry, A.D. DeVilbiss, T.E. Tsai *J. Opt. Soc. Am. B*, **12**, 2037 (1995).

[112] Y. Quiquempois, P. Niay, M.Douay, B. Poumellec, *Current Opinion in Solid State & Materials Science*, **7**, 89 (2003).

[113] A. Ozcan, M.J.F. Digonnet, G.S. Kino, *Appl. Phys. Lett.*, **84**, 681 (2004).

[114] T. Fujiwara, D. Wong, S. Fleming, *IEEE Photon. Tech. Lett.* **10**, 1177 (1995).

[115] X.C. Long, S.R.J. Brueck, *IEEE Photon. Tech. Lett.*, **9**, 767 (1997).

[116] Y. Ren, C.J. Marckmann, J. Arentoft, M. Kristensen, *IEEE Photon. Tech. Lett.*, **14**, 639 (2002).

[117] D. Faccio, A. Busacca, D.W.J. Harwood, G. Bonfrate, V. Pruneri, P.G. Kazansky, *Opt. Comm.*, **196**, 187 (2001).

[118] J. Khaled, T. Fujiwara, M. Ohama, A.J. Ikushima, *J. Appl. Phys.*, **87**, 2137 (2000).

[119] A.S. Huang, Y. Arie, C.C. Neil, J.M. Hammer, *Appl. Opt.*, **24**, 4404 (1985).

[120] A. Ozcan, M.J.F. Digonnet, G.S. Kino, *Opt. Express*, **12**, 3367 (2004).

[121] A. Ozcan, M.J.F. Digonnet, G.S.Kino, *Electron. Lett.*, **39**, 1834 (2003).

[122] P.D. Maker, R.W. Terhune, M. Nisenhoff, C.M. Savage, *Phys. Rev. Lett.*, **8**, 21 (1962).

[123] J. Jerphagnon, S.K. Kurtz, *J. Appl. Phys.*, **41**, 1667 (1970).

[124] J.R. Fienup, *Opt. Lett.*, **3**, 27 (1978).

[125] T.G. Alley, S.R.J. Brueck, R.A. Myers, *J. Non-Cryst. Solids*, **242**, 165 (1998).

[126] A.C. Liu, M.J.F. Digonnet, G.S. Kino, *J. Opt. Soc. Am. B*, **18**, 187 (2001).

[127] N. Boling, A. Glass, A. Owyoung, *IEEE J. Quantum Electron.*, **14**, 601 (1978).

[128] D. Faccio, V. Pruneri, P.G. Kazanksy, *Appl. Phys. Lett.*, **79**, 2687 (2001).

[129] A. Ozcan, M.J.F. Digonnet, G.S. Kino, *Electron. Lett.*, **40**, 551 (2004).

[130] R.T. Crosswell, A. Reisman, D.L. Simpson, D. Temple, C.K. Williams, *J. Electrochem. Soc.*, **147**, 1513 (2000).

[131] Y. Quiquempois, G. Martinelli, P. Dutherage, P. Bernage, P. and M. Douay, *Opt. Comm.*, **176**, 479 (2000).

[132] Jobin Yvon S.A, 91380 Chilly, Mazarin, France, www.jyhoriba.com.

[133] I. Hamberg, C.G. Granqvist, *J. Appl. Phys.*, **60**, R123 (1986).

[134] H. Kima, C.M. Gilmore, A. Piqué , J.S. Horwitz, H. Mattoussi, H. Murata, Z.H. Kafafi, D.B. Chrisey, *J. Appl. Phys.*, **86**, 6451 (1999).

[135] R.L. Nelson, J.G. Grotea, J.B. Huddleston, J.S. Zetts, F.K. Hopkins, *Proc. SPIE Int. Soc. Opt. Eng.*, **4290**, 45 (2001).

[136] E.A. Marcatili, *Bell Syst. Techn. J.*, **48**, 2103 (1969).

[137] L.F. Stokes, M. Chodorow, H.J. Shaw, *Opt. Lett.*, **7**, 288 (1982).

[138] C.K. Madsen and J.H. Zhao, *J. Lightwave Technol.*, **14**, 437 (1996).

[139] C.K. Madsen and J.H. Zhao, *Opt. Lett.*, **23**, 186 (1998).

[140] D.G. Rabus, "*Realization of Optical Filters using Ring Resonators with Integrated Semiconductor Optical Amplifiers in GaInAsP/InP*", PhD thesis, Technischen Universität Berlin, (2002).

[141] D.G. Rabus, M. Hamacher, U. Troppenz, H. Heidrich, *IEEE J. Sel. Top. Quantum Electron.*, **8**, 1405 (2002).

[142] J. Niehusmann, A. Vörckel, P.H. Bolivar, T. Wahlbrink, W. Henschel, H. Kurz, *Opt. Lett.*, **29**, 2861 (2004).

[143] D. Marcuse, "*Light Transmission Optics*", New York: Van Nostrand Reinhold, pp. 398-406, (1972).

[144] V. Subramaniam, G.N. De Brabander, D.H. Naghski, J.T. Boyd, *J. Lightwave Technol.*, **15**, 990 (1997).

[145] BeamPROP™, RSoft Design Group, Inc., 400 Executive Boulevard, Ossining, NY 10562, 1-914-923-2164.

[146] MEMS L-Edit™, MEMSCAP Inc., 4021 Stirrup Creek Drive Suite, 120 Durham, NC 27703, http://www.memscap.com/.

[147] Photronics UK LTD, Trafford Park, Manchester M17 1PE, UK, http://www.photronics.com/.

[148] I. Kiyat, A. Aydinli, N. Dagli, *Optics Express*, **13**, 1900 (2005).

[149] R. Adar, M.R. Serbin, V. Mizrahi, *J. Lightwave Technol.*, **12**, 1369 (1994).

[150] R. Adar, Y. Shani, C.H. Henry, R.C. Kistler, G.E. Blonder, N.A. Olsson, *Appl. Phys. Lett.*, **58**, 444 (1991).

Appendix A

List of Publications

Articles In Refereed Journals:

1. Feridun Ay, Atilla Aydinli, Sedat Agan, "Low-loss as-grown germanosilicate layers for optical waveguides", *Applied Physics Letters*, **83**, 4743, (2003).

2. H.Z. Durusoy, O. Duyar, A. Aydinli, F. Ay, "Influence of substrate temperature and bias voltage on the optical transmittance of TIN Films", *Vacuum*, **70**, 21, (2003).

3. Feridun Ay, Atilla Aydinli, "Comparative investigation of hydrogen bonding in silicon based PECVD grown dielectrics for optical waveguides", *Optical Materials*, **26**, 33, (2004).

4. A. Ozcan, M.J.F. Digonnet, G.S. Kino, F. Ay, A. Aydinli, "Characterization of thermally poled germanosilicate thin films", *Optics Express*, **12**, 4698, (2004).

5. Feridun Ay, Askin Kocabas, Coskun Kocabas, Atilla Aydinli, Sedat Agan, "Prism coupling technique investigation of elasto-optical properties of thin polymer films", *Journal of Applied Physics*, **96**, 7147, (2004).

6. S. Agan, F. Ay, A. Kocabas, A. Aydinli, "Stress effects in prism coupling measurements of thin polymer films", *Applied Physics A - Materials Science*

& Processing, 80, 341, (2005).

7. Askin Kocabas, Feridun Ay, Aykutlu Dâna, Isa Kiyat, Atilla Aydinli, "High refractive index measurement via elastomeric grating coupler", Accepted for publication, *Optics Letters*, (2005).

Refereed Proceedings:

1. F. Ay, A. Aydinli, C. Roeloffzen, A. Driessen, "Structural and Loss Characterization of SiON Layers for Optical Waveguide Applications", *IEEE Lasers and Electro-Optics Society (LEOS)* 2000 Annual Meeting, **2**, 760, (2000).

2. M. Bayindir, Feridun Ay, A. Aydinli, E. Ozbay, "Modification of photoluminescence in one-dimensional hydrogenated amorphous silicon oxynitride photonic band gap structures", *2001 OSA Annual Meeting / ILS-XVII*, ThW33, 114, (2001).

3. Feridun Ay, A. Aydinli, G. Özen, S. Cenk, "Effect of the local environment on the emission properties of Tm3+ in TeO WO and TeO2+CdCl2 glasses", *2001 OSA Annual Meeting / ILS-XVII*, ThW35, 115, (2001).

4. Feridun Ay, Sedat Agan, Askin Kocabas, Atilla Aydinli, "Elasto-Optical Properties of Thin Polymer Films by Prism Coupling Technique", *12th European Workshop on Heterostructure Technology*, San Rafael, Segovia-Spain, Book of Abstracts, WedB4, (2003).

5. Feridun Ay, Sedat Agan, Askin Kocabas, Coskun Kocabas, Atilla Aydinli, "Elasto-optical properties of thin polymer films by prism coupling technique", *2003 OSA Annual Meeting / ILS-XIX*, Tucson-Arizona, USA, ThH4, 112, (2003).

6. Feridun Ay, Sedat Agan, Atilla Aydinli, "As-grown low-loss germanosilicate layers by PECVD", *CLEO/IQEC* and PhAST Technical Digest on

CDROM (The Optical Society of America, Washington, DC, 2004), CThP7, (2004).

7. Feridun Ay, Sedat Agan, Askin Kocabas, Atilla Aydinli, "Prism Coupling Measurements of Elasto-Optical Constants of Thin Polymer Films", *AIP Conference Proceedings*, **709**, 435, (2004).

8. Feridun Ay, Sedat Agan, and Atilla Aydinli, "Plasma-enhanced chemical vapor deposition of low- loss as-grown germanosilicate layers for optical waveguides", *Proc. SPIE Int. Soc. Opt. Eng.* **5451**, 511, (2004).

9. F. Ay, A. Ozcan, M.J.F. Digonnet, G.S. Kino, A. Aydinli, "Thermal Poling of Germanosilicate Layers", *NATO ADVANCED RESEARCH WORKSHOP* (ARW) Frontiers in Planar Lightwave Circuit Technology: Design, Simulation and Fabrication, Ottawa, ON, Canada, (2004).

10. A. Ozcan, M. J. F. Digonnet, G. S. Kino, F. Ay, and A. Aydinli, "Thermally poled germanosilicate films with high second-order nonlinearity", *CLEO/IQEC* and PhAST Technical Digest on CDROM (The Optical Society of America, Washington, DC, 2005), (2005).